SYNTHESIS AND CHARACTERIZATION OF SILVER SILICA NANOCOMPOSITE MATERIALS VIA SOL-GEL TECHNIQUE

TAIFUNISYAM TAIB

INSTITUTE FOR ADVANCED STUDIES
UNIVERSITY OF MALAYA
KUALA LUMPUR

2023

SYNTHESIS AND CHARACTERIZATION OF SILVER SILICA NANOCOMPOSITE MATERIALS VIA SOL-GEL TECHNIQUE

TAIFUNISYAM TAIB

DISSERTATION SUBMITTED IN FULFILLMENT OF THE REQUIREMENT FOR THE DEGREE OF DOCTOR OF PHILOSOPHY

INSTITUTE FOR ADVANCED STUDIES
UNIVERSITY OF MALAYA
KUALA LUMPUR

2023

UNIVERSITI MALAYA

ORIGINAL LITERARY WORK DECLARATION

Name of Candidate: TAIFUNISYAM BIN TAIB

Registration/Matric No: 17044204/2 (New) / HHC 120012 (Old)

Name of Degree : PhD

Title of Project Paper/Research Report/Dissertation/Thesis ("this work"):
SYNTHESIS AND CHARACTERIZATION OF SILVER SILICA NANOCOMPOSITE MATERIALS VIA SOL-GEL TECHNIQUE

Field of Study: ADVANCED MATERIALS/NANOMATERIALS

I do solemnly and sincerely declare that:

(1) I am the sole author/writer of this work;
(2) This Work is original;
(3) Any use of any work in which copyright exists was done by way of fair dealing and for permitted purpose and any excerpt or extract from, or reference to or reproduction of any copyright work has been disclosed expressly and sufficiently and the title of the Work and its authorship have been acknowledge in this Work;
(4) I do not have any actual knowledge nor do I ought reasonably to know that the making of this work constitutes an infringement of any copyright work;
(5) I hereby assign all and every rights in the copyright to this Work to the University of Malaya ("UM"), who henceforth shall be owner of the copyright in this Work and that any reproduction or use in any form or by any means whatsoever is prohibited without the written consent of UM having been first had and obtained;
(6) I am fully aware that if in the course of making this Work I have infringed any copyright whether intentionally or otherwise, I may be subject to legal action or any other action as may be determined by UM.

Candidate's Signature Date:14th April 2023

Subscribed and solemnly declared before,

Witness's Signature Date: _____

Name:
Designation

ABSTRACT

Various filling fractions of silver silica nanocomposites (Ag-SiO_2 NC) were successfully synthesized via sol-gel technique and deposited onto indium tin oxide via electrophoretic deposition (EPD). The size of Silver Nanoparticles (AgNPs) synthesized by reduction method was determined to be within 20-30 nm, homogeneous and spherical in shape observed from Transmission electron microscopy (TEM) images. TEM images also confirmed that the particle distance between AgNPs in the Ag-SiO NC varies according to the filling fractions. The increase in crystalline phase was observed by the increase of peaks intensity of X-ray diffraction (XRD) spectra as the increase of AgNPs amount in the nanocomposites. UV–vis spectroscopy shows that the intensity of the Ag–SiO_2 NCs peak is greatly reduced with a clear and sharp absorption peak. The Fourier-transform Infrared (FTIR) spectra shows similar peaks for all the various filling fractions of Ag-SiO_2 NC. However the peaks shown slightly shifted indicating the existence of the AgNP within the silica nanostructures. Spectroscopy Ellipsometry shows that the effective permittivity and refractive index obtained from the optimum filling fraction are -0.88 and 0.90, respectively. The use of 4-Aminobenzenethiol (4-ABT) as the probe molecule on the substrate greatly enhances the Surface-enhanced Raman Spectroscopy (SERS) signal of the nanocomposites. The results from different pH values confirm that the substrate is stable and gives the strongest SERS enhancements in alkaline environment. The photoelectrochemical behavior of Ag-SiO_2 NC thin films was also investigated. Thin films grown at higher Ag composition showed good photoelectrochemical behavior.

ABSTRAK

Komposit nano gabungan zarah nano perak dan silika pada nisbah pengisian yang berbeza dengan ditetapkan kepekatan zarah nano perak (AgNPs) telah berjaya disintesis dengan kaedah sol-gel dan didepositkan ke atas lapisan Timah Indium Oksida melalui Pendepositan Eletroforetik (EPD). Saiz zarah nano perak yang disintesis melalui kaedah penurunan kimia didapati dalam lingkungan bersaiz diameter 20-30nm, berbentuk sfera dan seragam sepertimana yang diperhatikan daripada imej Mikroskop Elektron Pancaran (TEM). Imej yang dihasilkan oleh TEM juga mengesahkan bahawa jarak antara zarah nano perak yang terkandung di dalam komposit nano Ag-SiO_2 NC berubah mengikut nisbah pengisian. Pelbagai pecahan pengisian komposit nano Ag-SiO_2 NC berjaya didepositkan ke atas lapisan Timah Indium Oksida melalui kaedah Pendepositan Elektroforetik (EPD). Peningkatan fasa berhablur diperhatikan melalui peningkatan puncak dalam spektrum Sistem Pembelauan sinar X (XRD). Keputusan analisis Spektroskopi Ellipsometri menunjukkan bahawa nilai ketelusan berkesan dan indeks biasan yang diperoleh daripada nisbah pengisian optimum ialah -0.88 dan 0.90 masing-masing. Larutan 4-Aminobenzenethiol (4-ABT) yang dijadikan sebagai prob molekul ke atas komposit nano Ag-SiO_2 NC telah berjaya meningkatkan isyarat Spektroskopi Raman dipertingkat permukaannya (SERS) bagi komposit nano tersebut. Keputusan daripada kajian pH mengesahkan bahawa substrat SERS berasaskan nanokomposit perak-silika adalah stabil dan memberikan peningkatan isyarat SERS terkuat dalam persekitaran beralkali. Kajian fotoelektrokimia ke atas filem nipis Ag-SiO_2 NC juga telah disiasat. Filem nipis Ag-SiO_2 NC yang telah dideposit pada lapisan Timah Indium Oksida pada komposisi Ag dengan nilai nisbah pengisian 0.6 (Sampel ID: Ag60) menunjukkan keputusan fotoelektrokimia yang baik.

ACKNOWLEDGEMENTS

It is a great honor for me to express my deepest sense of gratitude to my supervisors ; Prof. Dr. Mohd Rafie Johan and Prof. Dr. Wan Jefry Basirun on their dedication and endless support throughout my research journey. Their guidance, scholarly advice and enlightening ideas have helped me to complete this research.

This research was supported by grants from the Postgraduate Research Fund (PPP), Nanocat RU Grant 2020, University of Malaya (UM) and Research Endowment Fund Type A (EDW A), Research Management Centre, International Islamic University Malaysia (IIUM). I appreciatively acknowledge University of Malaya and International Islamic University Malaysia for the financial support that has enabled me to complete this study.

My highest gratitude goes to all my research colleagues and friends who I started with and gained a lot of experience and kind assistance from them during my research works especially Yusliza Yusof, Nadia, Tan Kim Han from Nanomaterial Engineering Laboratory, Nanotechnology and Catalysis Research Centre (NANOCAT) for their kind support that has help me to accomplish this research work.

Last but certainly not least, my sincere appreciation goes to my mother, Aine binti Md Zain for your endless love and prayers, my beloved wife, Zarina binti Hussin, for your understanding and sacrifices throughout this endeavour.

Finally, to my late father, Taib bin Salleh, your inspiration has always been there all the time until the last word of this research journey.

TABLE OF CONTENTS

LIST OF FIGURES

LIST OF TABLES

LIST OF SYMBOLS AND ABBREVIATIONS

α	: Absorption coefficient
ε_r	: Real part of permittivity
ε_i	: Imaginary part of permittivity
ε_0	: vacuum permittivity
^oC	: Degree Celsius
$h\upsilon$	: Energy of light
AgNPs	: Silver Nanoparticles
SPR	: Surface Plasmon Resonance
SERS	: Surface Enhanced Raman Spectroscopy
MG	: Maxwell Garnett
SiO_2	: Silica
Ag-SiO_2 NC	: Silver Silica Nanocomposite
TEOS	: Tetraethylorthosilicate
4-ABT	: 4-Aminobenzenethiol
$AgNO_3$	: Silver Nitrate
ITO	: Indium Tin Oxide
EPD	: Electrophoresis Deposition
DSC	: Differential Scanning Calorimetry
UV-vis	: Ultraviolet Visible Spectroscopy
EIS	: Electrical impedance spectroscopy
FESEM	: Field Emission Scanning Electron Microscope
FTIR	: Fourier Tranform Infrared
EIS	: Electrochemical Impedance Spectroscopy

PL	: Photoluminescence Spectroscopy
ΔH	: Entalphy of transition
TGA	: Thermogravimetric analysis
UHV	: Ultra High Vacuum
STM	: Scanning Tunneling Microscopy
SPP	: Surface Plasmon Polaritons
LSPR	: Local Surface Plasmon Resonance
TEM	: Transmission Electron Microscope
T_g	: Glass transition temperature
T_m	: Melting temperature
Uv-vis	: Ultraviolet visible
wt. %	: Weight percent
XRD	: X-ray Diffraction
ΔH_m	: Heat of melting
ε_r	: Dielectric constant
χ_c	: Degree of crystallization
χ_m	: Degree of melting

CHAPTER ONE:

INTRODUCTION

1.1 Background

The study of noble metals such as multifunctional metal nanoparticles and its employment as basic engineered building block in micro and nano-scales of various products has increased tremendously in the last several decades. These noble metal satisfies the versatility needs in the functional material in their applications which range from optical and photovoltaic to biological and chemical sensors (Oldenburg, 2014) and enhanced their performance with better quality than ordinary products with better functions but with less financial implications (Goldman & Coussesn, 2005).

The uniqueness of these noble metal nanoparticles such as silver, gold and copper are rendered by their strong surface plasmon resonance (SPR) properties. Due to the SPR phenomenon, the nature of these metal nanoparticles can be tailored to provide a specific optical characteristic. Their properties varies with the change in their size, shape and geometry(Li *et al.*, 2014), surface plasmon resonance spectra (Vernon *et al.*, 2010) and Raman surface-enhancement (Moskovits, 2005) and also has led to novel applications in optical sensing (McFarland & Duyne 2003), catalysis (Cliffel, 2004), luminescent tagging (Gao & Nie 2004) and functioned biological areas (Rothrock *et al.*, 2005).

Surface plasmon resonance (SPR) occurs due to the collective oscillations of free electrons from the interaction of metal conduction electrons of metal with the incident photons. The earliest work on surface resonance plasmon application was found in the famous Lycurgus Cup produced during ancient Roman civilization (Hornyak *et al.*,

2008). However, it was not until 1990 that the remarkable properties of the Cup was uncovered. Scientist found that the impressive dichroism was due to the presence of nanosized particles of silver, gold and copper up to 100 nm in size. (Hornyak *et al.*, 2008).

Silver nanoparticles (AgNPs) is the promising candidate compared to other metal nanoparticles reported in the literature (Bigot, 2000) due to its excellent and remarkable localized SPR, which give them the unique properties such as broad spectrum of surface-enhanced Raman spectroscopy (SERS) (Natsuki *et al.*, 2015) and strong signal in uv-vis absorption (Jasiorski *et al.*, 2014). The integration of AgNPs with other functional electronics or optical assemblies have given rise to novel applications to the ordinary nanocomposite (Goldman & Coussens, 2005). Additional applications include molecular diagnostics, chemical sensors, photovoltaics and catalyst (Oldenburg, 2014).

Since late 1980s, fundamental studies have shown that AgNPs possess interesting interaction response to incident light due to their dielectric constants, which enable the occurrence of light repines in the visible frequency (Hirai *et al.*, 1999). The remarkable properties of silver made it one of the metals that can be tailored to react across the full visible spectrum. The fundamental of metal-light interaction can be applied in various field such as photonics, whereby new materials can be made to transport light through the optical cables with a higher yield (Luo *et al.*, 2005).

All the convincing motivation of material advancement arose from the high sensitivity of AgNPs with strong SPR on the nanostructures of the host medium with special properties not found in nature. This is due to the AgNPs ability to affect the permittivity or permeability of the host medium by having strong electric dipolar and magnetic response (Che Lah *et al.*, 2011). With the increase of silver content randomly dispersed

in the host medium, AgNPs interconnected with each other lead to the formation of electrical conductive metal network at the percolation threshold. The plasma oscillation of these electrons in the interconnected AgNPs leads to a negative permittivity and was analyzed using the Drude model in the nanocomposite structure (Shi *et al.*, 2013).

Since the last two decades, many research have been devoted to investigating the properties of AgNPs synthesized via chemical reductions (Tripathy et all, 2010), gas condensation(Evanoff *et al.*,2005) laser irradiation (Suber *et al.*,2005) sonochemical deposition (Bresme *et al.*, 1998) and nanostructured templates (Wilcoxon *et al.*, 1998). All these efforts have advanced the scientific knowledge of the nature of AgNPs. Ahead among others, chemical reduction techniques offer a novel, simple procedure for the synthesis of AgNPs compared to others which required higher production cost and more process timing because they used complex set-ups for synthesis (Faraudo *et al.*, 2003, Guo *et al.*, 2008, Ditlbacher *et al.*, 2005). Other advantages are well-defined particle size, shape and size distribution which could be controlled by judiciously selecting the reaction temperature, order of reagents addition and protective agent/metal compound ratio which are the factors governed the plasmon resonance excitation of nanoparticles.

1.2 Plasmonic Nanocomposite Materials

Nanocomposite materials have been widely become the focus of highly intense research in the last decades. This is due to their special and unique size-dependent chemical and physical properties (Henglein, 1993). In recent years, nanocomposite embedded with plasmonic nanomaterials with tailored size and shape has shown remarkable properties for many applications in optical, electrical and catalyst (Sakoda, 2001). These materials rely on the controlled interaction between the propagation of electromagnetic field with the free electron at the surface of the metal (typically silver).

Functionalization of metal nanoparticles embedded on the surface of dielectric material such as silica to acquire nanocomposite structures is motivated by interdisciplinary applications in nanotechnology and nanoscience (Kawashita *et al.*, 2003; Niitsoo *et al.*, 2011; Choma *et al.*, 2012). In its hybrid metallic and non-metallic nanostructure, silica has demonstrated a wide range of applications such as in magnetic nanomaterials (Ren *et al.*, 2009), photocatalysis (Wang *et al.*, 2012), photonics (Lu *et al.*, 2002), optoelectronics (Mokkapati *et al.*, 2009), surface enhanced Raman spectroscopy (Liu *et al.*, 2011), biomolecular detection (Kalele *et al.*, 2005) and biocatalysis (Phadtare *et al.*, 2003).

Depending on the preferred interdisciplinary application, prior to the metal inclusions, the AgNPs are synthesized either in the form of pure nanoparticles or an ionic form to various ratio between AgNPs and oxide matrix such as silica (Flores *et al.*, 2008; Quang 2011). Silica nanostructure are very suitable as a substrate for the deposition of metals mainly because of their high active surface area and fine chemical durability (Juarez et al., 2009). Nanoparticles can obtained improved chemical stability and size monodispersity through deposition onto the silica support (Jasiorski *et al.*, 2014).

The undisputed advantage of silica nanoparticles is also due to the possibility for surface functionalization. The modification of the silica particle surface enables the attachment of AgNPs as well as to control their growth. There are numerous papers published for the synthesis of embedded AgNPs onto silica nanoparticles (Flores *et al.*, 2008). The modification of silica nanostructure surface by various embedded amount of AgNPs is proven to effect its properties. The optical, electrical and thermal properties of the nanocomposite of Ag and SiO can be varied by controlling the amount AgNPs

embedded in the silica nanostructure (Jasiorski *et al.*, 2014 ;Kumar *et al.*, 2019; Pei *et al.*, 2010). The incorporation of nanoparticles in various amounts will extend their utility with the increase of AgNPs in the composition. The new nanocomposites exhibit novel optical properties as the plasmonic resonances are strongly affected by the surrounding matrix, because the closely spaced particles in matrices can exhibit cooperative phenomena when interacting with light. The AgNPs dispersion in the silica host matrix possesses efficient light scattering into the absorbing layer, or nano-textured surface of anti-reflection coatings to decrease undesirable back reflections which degrade the photovoltaic applications (Tan *et al.*, 2012).

If novel optical properties are obtained from a sufficient amount of AgNPs randomly embedded into the silica nanostructure, they constitute what is known as a metamaterial (Capolino, 2010). Metamaterial is an artificially structured material that exhibits extraordinary electromagnetic properties not available or not easily obtainable in nature. Since the early 2000, metamaterials have emerged as a rapidly growing interdisciplinary area, involving physics, electrical engineering, materials science, optics and nanoscience. The properties of metamaterials are tailored by manipulating their internal physical structure such as dispersive permittivity and permeability (Etrich *et al.*, 2014).

The permittivity is a measure of the dielectric polarization of the material when subjected to an electric field. The permeability is the degree of magnetization that a material obtains in response to an applied magnetic field. The strong negative permittivity of AgNPs is expected to effect the host medium to obtain special properties with sufficient volume ratio to the host medium (Cheng *et al.*, 2020).

Other optical properties which show novelty, such as the polarization and directional transmissivity of light can be affected as well. This makes them remarkably different from natural materials, whose properties are mainly determined by their chemical constituents and bonds. The primary reason for the intensive interest in metamaterials is their unusual effect on light propagation (Zhang, 2014). The isolated functioning of AgNPs act as a simplest meta-atom (sub-unit of metamaterial) providing the affect of dispersive permittivity or permeability with strong magnetic or electric dipolar response Numerous researchers have confirmed that the desired optical properties could be attained by varying the parameters of inclusion in the dielectric host material (Etrich *et al.*, 2014). The two main parameters are the filling fraction and the intrinsic properties of the constituents. Despite the strong polarization and large dispersion due to high filling fractions, plasmonic nanocomposites with optimum filling fractions should not disqualify the applications of the nanostructure (Etrich *et al.*, 2014).

At present, these new properties is realized by a nanocomposite material consisting of thin wires and split-ring resonators (Shelby *et al.*, 2001). Metal inclusions such as metallic nanowires, with a separation smaller than the incident wavelength are capable to tune the optical properties of the dielectric matix as long as the effective media approximation is valid. Sonication during gelation has been shown to improve the nanowire dispersal. The reflectometry data show the decrease of the real part of the refractive index from 1.17 to 1.1 at 1064 nm wavelength, but at the same time recorded the increase in the imaginary part. Transmisson loss is also recorded in the sol-gel which is mainly due to the inhomogeneous scattering (Kielbasa *et al.*, 2007).

There are several methods used for the fabrication of nanocomposite to maintain the homogeneity. Generally, there are two category which is the top-down and bottoms approach. The bottoms-up approach is much better in generating uniform particles, distinct size and shape. Despite the fact that these factors led to the growth of the nanocomposite, the sol-gel is found to have greater advantages due to its stability and better dispersion of metal within the dielectric surface nanostructure (Hornyak *et al.*, 2008).

The sol-gel synthesis is a bottom-up method which falls under the sedimentation method of liquid-phase category. *Sols* are actually a colloidal suspension of nanoparticles and *gel* is a material that contains liquid within its pore nanostructure. The several sol-gel methods are the hydrolysis and condensation of metal alkoxides sol-gels, non-hydrolytic sol-gel reactions, Pechini sol-gel methods, polymer pyrolysis sol-gels, inorganic-organic hybrids sol gels and colloidal dispersion sol gels (C.J. Brinker *et al.*, 1990).

1.3 Problems Statement

To produce materials in the visible region with new properties such as with negative refractive index and negative phase velocity (in nano-inductors and nano-capacitors) which are not found in nature faces certain challenges((Alu *et al.*,2006), since the magnetic permeability approach the free space permeability due to the molecular currents in the materials (Landau *et al.*, 1984). Another approach is to design sub-wavelength inclusions that exhibit magnetic dipolar resonant response, and thus provide the possibility of having negative effective magnetic dipole moment at optical frequencies. This is based on the collective resonance of an array of plasmonic nano-particles arranged in a specific pattern (Alu *et al.*,2006).

One of the great challenges in developing such properties in the near-IR and visible frequencies is that the electric and magnetic sub-units must be fabricated on the nanoscale for the medium to be considered optically homogeneous (Atsushi, 2011). In addition, the electric conductivity of the metals, behave differently when the frequency is increased into the IR and visible regions. A few possibilities in solving this issue are the utilization of coupled plasmonic parallel nano-wires and nano-plates (Podolskiy *et al*., 2002), closely-packed inclusions with negative permittivity and their electrostatic resonances (G. Shvets *et al.*,2004). Despite their intriguing electrical, thermal and optical properties and promising candidates in flexible electronics (Azulai *et al.*, 2009; Sun 2010; De *et al.*, 2009), the film posses significant roughness and irregular morphologies and shows circular rings and discontinuous film on the substrate (Lu *et al.*, 2010; Robert *et al.*, 2009; Budhiraja *et al.*, 2013).

Beside numerous theoretical research on the tunable properties of metal-dielectric nanocomposite using the Maxwell Garnet (MG) model, less works have been devoted to the effect of various volume ratios of the AgNPs to the silica, on its optical and physical properties at constant concentration of AgNP on the experimental mode. This is due to the MG model doesn't stabilize at higher filling fractions (Chaumet *et al.*, 1998). Hence, the best composition of metal-dielectric host is yet to be achieved. The instability is caused by the van der Waals forces between nanofillers generally lead to strong agglomeration in the matrix, thereby dramatically reducing the electrical conductivity. To address these issues, various approaches for the dispersion of nanofillers in the nanocomposite matrix have been introduced. (Kim *et al*., 2021). Although this has not been thoroughly investigated, one of the the possible method is based on the MG model(Amroziak et al.,2019).

In the case of plasmonic resonance, the Maxwell Garnett formula is correct only at a certain volume fraction of the inclusions, where the spatially domain separation and electrostatic interaction between the inclusions is enumerable (Belyaev *et al.*, 2018). Currently, the effective media approximation is done based on theoretical studies. More studies are devoted on the theoretical aspects of the model compared to the experimental aspects. Therefore, the fine tuning of the optical properties into new dielectric value may offer versatility of the $AgSiO_2$ NC for the fabrication a substrate for further applications.

1.4 Research Objectives

The objectives of this study are listed as follows:

a) To synthesis AgNP via chemical reduction method and Silver Silica Nanocomposite ($AgSiO_2$ NC) via Sol-gel technique.

b) To characterize the $AgSiO_2$ NC at various filling fraction with several analytical techniques; DSC, TGA, TEM, FESEM, UV-Vis spectroscopy, XRD, FTIR, PL spectroscopy, SERS and Electrochemical Impedance Spectroscopy (EIS)).

c) To optimize the Ag-SiO_2 NC for achieving the best filling fraction of Ag/SiO_2 and SERS properties.

d) To evaluate the PEC water splitting performance of Ag-SiO_2 NC under illumination.

1.5 Outline of Thesis

The first chapter, which is Chapter One includes the overview of this research work, objectives of research, problem statement and the outline of the thesis. The literature review of metallic nanoparticles, dialectric nanostructure characteristics and techniques on synthesis of the nanocomposite is presented in Chapter Two. The important aspects of metallic nanoparticles and the dielectric nanostructure will be reviewed, including the optical, structural and morphology of Ag-SiO_2 NC.

Chapter Three focuses on the experimental procedures. Detailed procedures on the synthesis of the nanoscale Ag-SiO_2 NC, morphological studies by using transmission electron microscopy (TEM), Uv-vis spectral measurements, infrared spectra were recorded using FTIR spectrophotometer, X-Ray diffraction (XRD) method to study the crystalline structure, electrophoresis deposition (EPD) to fabricate the thin film of nanocomposite for permittivitiy by using spectroscopic ellipsometry (SE) and the structural fingerprint of the nanostructure were studied using Raman machine for SERS applications. The photoelectrochemical behavior of Ag-SiO_2 NC thin films was also investigated.

Chapter Four presents the results from the characterization techniques on the optical and permittivity studies right upon the experiments carried out in the previous chapter. UV-vis spectroscopy, transmission electron microscopic (TEM) images are provided in addition to the thin film fabrication by Electrophoresis Deposition for permittivity studies using Ellipsometer Spectroscopy.

Chapter Five provides the results for the structural studies using XRD, FTIR and thermal studies using Differential scanning calorimetry (DSC) and Thermogravimetric analysis (TGA) characterization and application on SERS and Electrochemical Impedance Spectroscopy.

The final chapter, which is Chapter Six, is the summary of the whole project with a brief conclusion. Moreover, some of the future work will also be suggested in this chapter.

CHAPTER TWO:

LITERATURE REVIEW

2.1 Introduction

A concise and comprehensive review of the past research on the synthesis and characterizations of the metal and its nanocomposite are reviewed in this chapter. The comprehensive review in this chapter covers the following sections : a) Surface plasmon resonance (SPR), b) Extraordinary properties of silver nanoparticles (AgNPs), c) Properties of $AgSiO_2$ nanostructures, d) Synthesis of $AgSiO_2$ nanostructures.

2.2 Surface Plasmon Resonance

SPR is a collective excitation of free electrons at the surface of a metal stimulated by incident light with a certain characteristic electromagnetic frequency. The resonance condition is created when the photon light frequency corresponds to the natural frequency of the electron surface that is proportional to the positive core recovery force. As shown in Figure 2.1 (a) SPR occurs at metal surface such as gold and silver when an incident light beam strikes the surface at a specific angle depending on the thickness of the molecule layer at the surface of a metal. This resonance occurs due to the negative dieletric properties of silver or gold at optical frequencies.

The speciality of Surface Plasmon Resonance (SPR) as the optical and electrical properties of metallic materials has made the nanotechnology field become more attractive and many discoveries pertaining to its applications have been made. Research

on the nanostructured plasmonic materials has intensified in recent decades. This is due to its unique shape and size-dependent, chemical and physical properties with the possibility to tailoring the particle shape and size. With the excellent control over the shape and uniformity, the result in novel properties among these materials can be exploited for various electrical and optical applications, including photonic crystals, nano-fabrications and nano-electronics.

The applications of SPR usually takes advantage of graded decrease in the intensity of the refracted light. In a local nanometer-sized structure, SPR is called the local surface plasmon resonance (LSPR). Thus, this produces a strong optical extinction of the metal nanoparticles. The excitation of conduction free electron generates local electromagnetic fields near to the metal surface.

Surface Plasmon Polariton (SPPs) are the electromagnetic waves which travel along the metal-dielectric interface and coupled to the oscillations of electrons in the metal. The coupling of light to the SPPs requires a phase matching, where the surface plasmon wave phase velocity is equal to the incident light lateral component (Ritchie, 1957; Barnes, Dereux & Ebbesen, 2003). As being localized at the interface as shown in Figure 2.1 (b) SPP will become extremely sensitive even to a small changes in the refractive index at the interface (Maier, 2007; Kabashin, 2009).

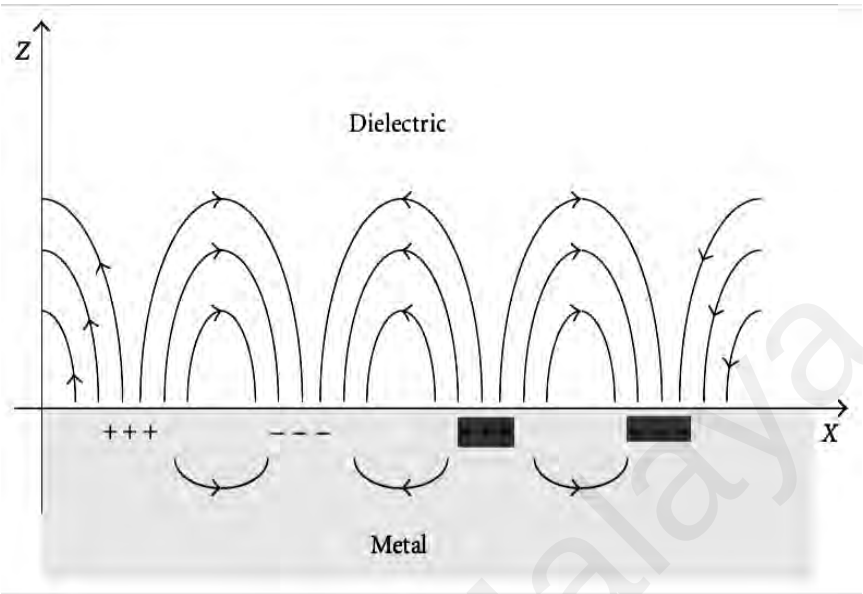

(a)

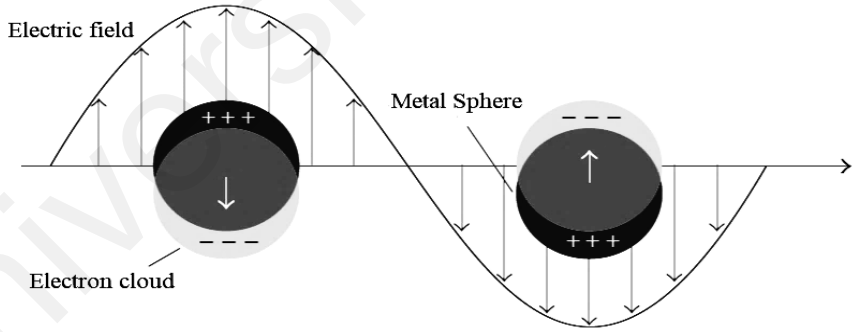

(b)

Figure 2.1: Surface plasmon resonance of metal nanoparticles. (a) Schematic diagram of propagating SPR along the dielectric-metal interface showing electric field generated around the oscillating surface electron. (b) Sign of localized surface plasmons on the side by side electron (Hong, 2012).

2.3 Silver Nanoparticles

Silver Nanoparticles (AgNPs) is a strong plasmonic materials with a remarkable optical properties compared to other noble metals such as gold and copper. The strong properties of AgNPs offer a lot of information and data about the physical state of the nanoparticles which can be acquired by analyzing the spectral properties of the nanoparticles in a solution. The response of AgNPs depends on the shape, size and geometry. As the diameter increases, the absorption peak of the plasmon resonance shifts to longer wavelengths and widens. The effect will be reversed when the diameter decreases. In general, the shape and size of the nanoparticles can be determined according to the pattern of SPR. Generally, any SPR pattern is a spectral fingerprint for any type of nanoparticles or nanostructures (Steven J. O, 2015). The SPR effect is more pronounced in the AgNPs compared to the AuNPs due to the very small AgNP dielectric constant value which causes a large local field enhancement and relatively smaller loss of the SPR propagation (G.Hong-Mei *et al.*, 2009).

Compared to Au nanoparticles, Ag nanoparticles displays brighter fluorescence (Le Gue´vel *et al.,* 2011) and receives greater attention owing to their considerable wide range of applications. Other advantages of AgNPs include strong scattering length and long-term stability. These remarkable properties are essential for a sensitive but stable applications in sensor and catalysis applications (Sengupta *et al.,* 2008).

In the recent years, numerous efforts have been focused on the development of AgNPs synthesis with higher dispersion and more uniform size and shape. The synthesis process fall under four categories, i.e, the physical, photochemical, biological and chemical approaches. (Cuenya *et al.*, 2010; Sau *et al.*, 2010; Zhang *et al.*, 2010).

Under the physical processes, the noble AgNPs are generally synthesized by evaporation and condensation by using a tube furnace at atmospheric pressure. The source material is vaporized into a carrier gas (Gurav *et al.*, 1994; Kruis *et al.*,2000; Magnusson *et al.*, 1999). Although this physical approach produces large quantities of AgNPs product, this technique has several disadvantages as the tube furnace tube occupies a huge space, consumes very high energy (J.Natsuki *et al.*, 2015) and is operated at high temperature (Kang, 2004).

In the photochemical process, AgNPs disintegrate into smaller size by irradiation until the nanoparticles achieve a relatively stable size and diameter distribution (Huang et al, 2008). However, high cost equipments are required in this method (Natsuki *et al.*, 2015).

In the biological approach, biological microorganism such as bacteria and fungus or plant extracts are used as reduction agents. The synthesized AgNPs from this approach are highly stable and provides an alternative source for the synthesis of AgNPs. However, from the advantages over the conventional chemical techniques, this technique is only suitable to produce AgNPs in smaller quantities (Natsuki *et al.*, 2015).

Compared to the abovementioned approaches, the chemical approach is the most preferred as the AgNPs could be highly dispersed and kinetically stabilized (Scaffardi *et al.*, 2005) moreover this method is convenient and using simple equipments. The intrinsic properties of AgNPs are determined mainly by the size and shape, which are controlled during the nucleation and subsequent growth. The most fundamental aspect of the process is the use of reducing agents and stabilizing or capping agents which determines the distribution and size of the AgNPs. On the other hand, the absorption peak is not observed in the absence of a stabilizer (Che Lah *et al.*, 2011).

The preparation of AgNPs in colloidal dispersion can be performed by chemical reduction. The size and shape of the AgNPs in this process is determined by the temperature. At the lowest temperature of 80 ºC the spherical-shaped AgNPs shows a single peak at 392 nm and a peak shift to 409 nm at a higher temperature However, the most prominent SPR absorption is recorded at 436 nm with oblate polygonal-shaped peak (Luo *et al.*, 2005). The SPR bands are further improved by adding a stabilizer such as Daxad 19 (sodium salt of polynaphthalene sulfonate formaldehyde condensate. In this process, the SPR bands of the spherical shape AgNPs at lower temperature 80 ºC is 430 nm, while the polygonal-shaped AgNPs at 120 ºC is 496 nm(Che Lah *et al.*,2011). The maximum absorbance is increased as the density increases higher at arbitrary temperature (Vodnik *et al.*, 2010; Mock *et al.*, 2002).

Real-space topography and imaging of the produced AgNPs is very significant for the correlation analysis of the size, shape, composition, structure and stability (Huayan *et al.*, 2015). These fundamental properties define the functionalities of the AgNPs for its applications in areas mentioned in the previous sections. The high functionality of the AgNPs is due to the numbers of silver atoms which consist as a single nanoparticle. The

diameter of the silver atom is about 0.288 nm. Thus a particle of one nanometer in diameter consists of 31 silver atoms while a 5 nm diameter AgNPs consists of 3900 silver atoms, while a particle with the a diameter size of 20 nm consists of 250,000 silver atoms. The size of the AgNPs in colloidal form is between 5 nm and 200 nm. The measurement of the particle sizes is performed using a Photon Correlation Spectrometer (PCS) that can measure sizes up to 1 nm (Huayan *et al.*, 2015).

The analysis performed by the PCS is in agreement with the images using Ultra High Vacuum Scanning Tunneling Microscopy (UHV STM). Figure 2.2 shows the topography of AgNPs using low-temperature STM at a base pressure 10-11 mbar, (Zhou *et al.*, 2018).

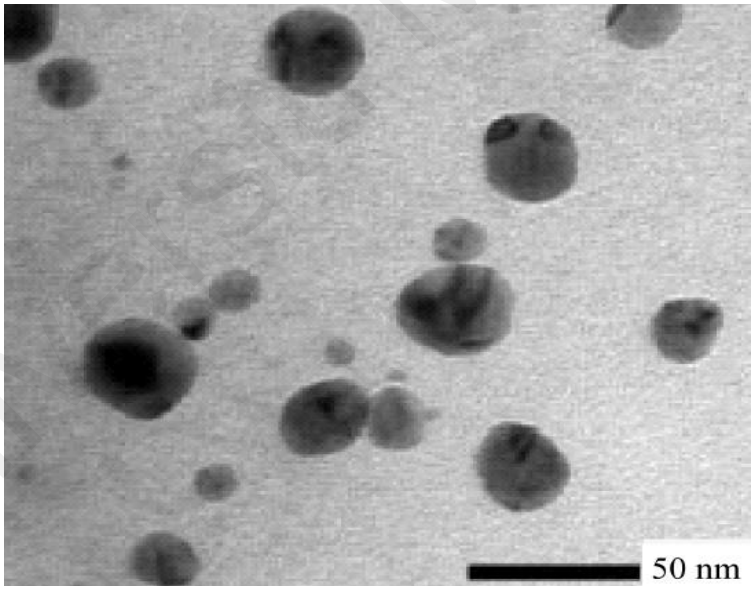

Figure 2.2: TEM image of AgNP dispersed in colloid (Mahmudin1, 2015)

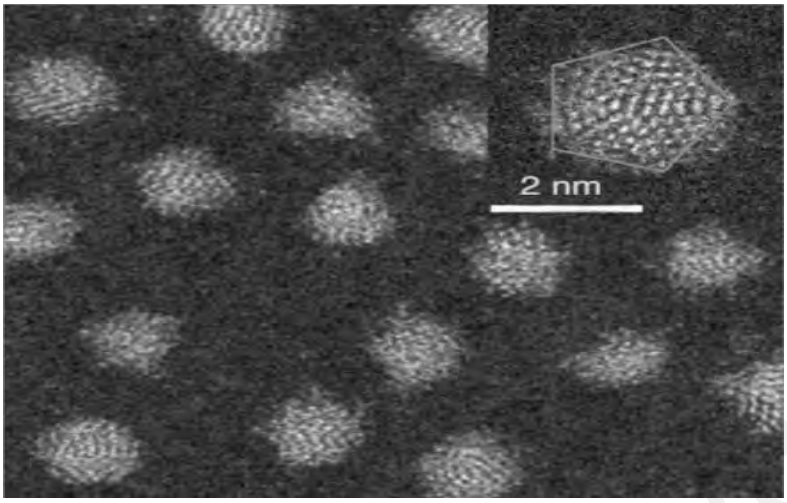

(a)

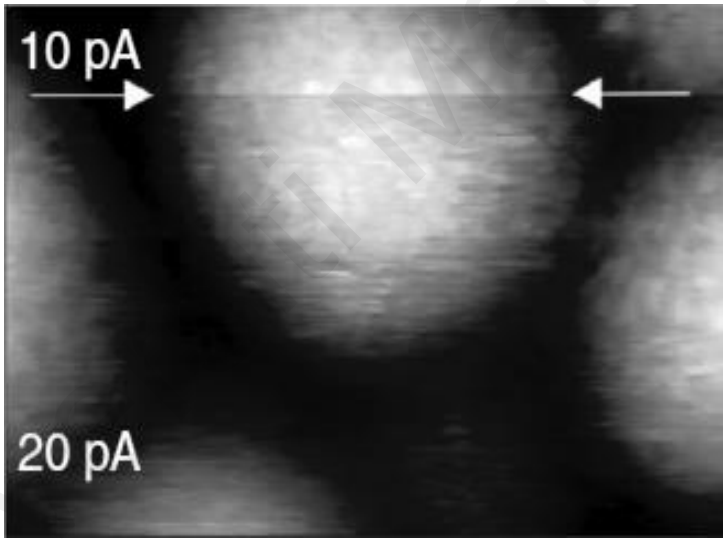

(b)

Figure 2.3: STM images for AgNPs a) at higher resolution and b) focus on one AgNPs.

Spherical AgNPs with average size of 20-30 nm in diameter exhibits the characteristic symmetric absorption peak at 430 nm (Awwad *et al.*, 2012), 420 nm (Trefry *et al.*, 2010; Baset *et al*., 2011) This absorption peak is shifted towards a higher wavelength region by tuning their physical properties such as shape and size of the particles. A single clear peak at 392 nm indicates the presence of a uniform, spherical-shaped nanoparticles at the

lowest temperature (80 ºC) (Luo *et al*., 2005). At higher temperature, the SPR bands are broaden and exhibit two maxima at 409 and 348 nm. This indicates the formation of spherical shaped AgNPs and the presence of truncated edges in the anisotropic structures, respectively. The SPR peaks for the oblate polygonal AgNPs appear at 436 and 322 nm at 120 ºC. The UV–vis results clearly support the TEM images in Figure 2.3. The increase in the maximum absorbance at each temperature is due to the particle density, which is strongly dependent on the amount of silver reduction at the surface of the medium (Mock *et al.,*2002 ; Pesika *et al.,* 2003; Vodnik *et al.,* 2010)

Among the various shape and size of AgNPs, the homogeneous spherical shape has more advantages due to its well-fitting to the Mie's Scattering Model (Amendola *et al.*, 2009). It is significant to note that Mie's model accounts well with the shape and size of the isolated AgNPs in the optical spectra in order to compute the effectiveness of the dielectric function of the simulated system in accordance to the Drude's model for metal nanoparticles (Che Lah *et al.*, 2011).

The dielectric function of the nanoparticles is related to its optical properties, in particular to the reflection, dispersion, polarization and transmission at the fundamental level. At this level, the dielectric function of AgNPs contributes to the understanding of electronic structure of the metal (Taft *et al.*, 1961 ; Honghua *et al.*, 2015).

The AgNPs is optically isotropic due to a face-centred-cubic crystal lattice. As a result, the dielectric function of AgNPs can be expressed as a scalar quantity $\varepsilon(\omega) = \varepsilon_o \, \varepsilon_r(\omega)$, where ε_o is the vacuum permittivity and $\varepsilon_r(\omega)$ is the relative dielectric function which, in the absence of magnetic affects, describes a full electromagnetic response of the

medium (Honghua *et al.*, 2015). The real part of ε_r and its imaginary component, ε_i can be represented by the Drude's model (Crooker *et al.*, 2003) as shown below:

$$\varepsilon_r(\omega) = 1 - \frac{\omega_{p^2}}{\omega^2 + \omega_{c^2}} \tag{2.1}$$

$$\varepsilon_i(\omega) = \frac{\omega_{p^2}\,\omega_c}{\omega(\omega^2 + \omega_{c^2})} \tag{2.2}$$

Whereby

$$\omega_c = \frac{v_f}{L} + \frac{2\,V_f}{d} \tag{2.3}$$

$$\omega = \frac{2\pi c}{\lambda} \tag{2.4}$$

Then, the relative dielectric values of $\varepsilon(\omega) = \varepsilon_r(\omega) + i\varepsilon_i(\omega)$ relates to the refractive index values by

$$\tilde{n}\,(\omega) = n(\omega) + ik(\omega) = \sqrt{\varepsilon\,(\omega)}\,. \tag{2.5}$$

2.4 Silver Silica Nanocomposite

Silver silica nanocomposite (Ag-SiO_2 NC) consists of dispersed AgNPs on the surface of Silica (SiO_2) nanostructure (Pei *et al.*, 2014). SiO_2 particle can be seen containing many small AgNPs with typical sizes of 5 nm in diameter as shown in Figure 2.4 (Jasiorski *et al.*, 2014).

The main advantage of this nanostructure is the dispersion of AgNPs throughout the silica which prevents the agglomeration of the AgNPs. This is possible due the high surface to volume ratio of the surface of SiO_2. The large number of hydroxyl group on the surface provides electrostatic binding energy with the AgNPs as shown in Figure 2.5.

(Das *et al.*, 2013; Maurizio *et al.*,2003). The SiO_2 nanostructure plays an important role in controlling the optical interactions and separation distance between the AgNPs which is effective in tuning the plasmonic properties. This will enable the nanostructure to create a hot spot between the closely packed AgNPs due to the localize electric field between the NPs (Rahman *et al.*, 2016).

The SiO_2 nanostructure acts as a appropriate carrier for the incorporation of AgNPs into polymers, coatings and optical applications. A further benefit is that the restriction of AgNPs mobility within the silica nanostructures facilitates the discharge and disposal of the AgNP themselves. The advantage of this property is the development of a stable substrate for sensor applications (Sanvicens *et al.*, 2008 ; Rameshkumar *et al.*, 2013 ; Radeshkumar *et al.*, 2006).

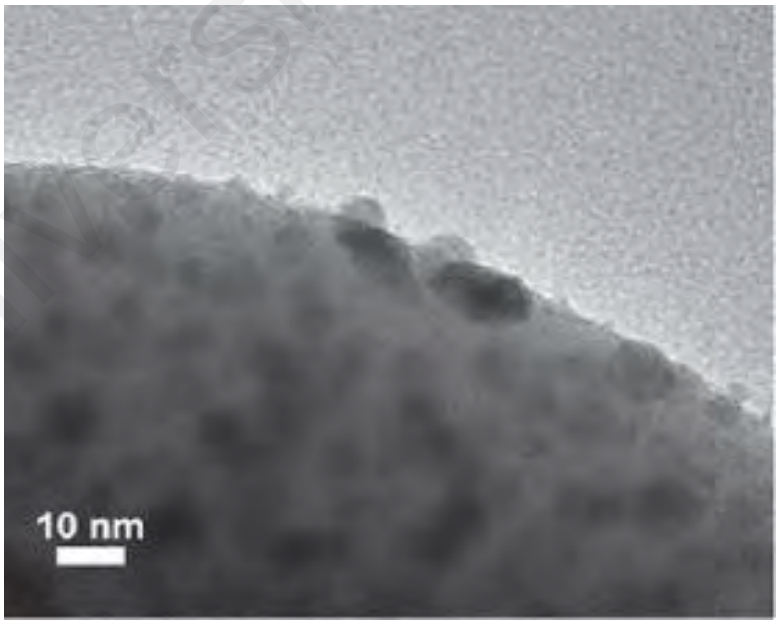

Figure 2.4: TEM images showing SiO_2 spheres with well disperse of AgNPs (Jasiorski *et al.*, 2014).

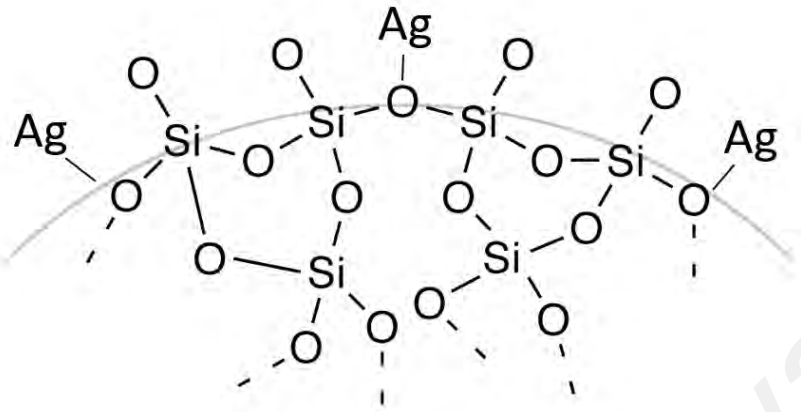

Figure 2.5: Surface structure of Ag nanoparticle decorated SiO_2 gel, dry and hydrated (Mons, 2007).

Under ambient temperatures, AgNPs tend to crystallize into silica nanostructures. This is another advantage for the functionalization of pure silica. Due to the strong ionic bond between the Si-O unit cell and AgNPs distorted from the ideal structure causing a large spontaneous polarization along the bond-axist (Rameshkumar et al., 2013; Merlin *et al*, 2009).

Due to this advantage, the Ag-SiO_2 NC possesses numerous novel properties such as hot spot for the electromagnetic signal for SERS applications and electromagnetic polarization based on the Drude and Lorentz model. However, the amorphous phase with the silica nanostructure is stabilized by the embedded of AgNPs (Rameshkumar *et al*, 2013).

The Ag-SiO_2 NC possess higher stability. The crystalline lattice structure of the Ag-SiO_2 NC possesses two kinds of bonds, named as B1 and B2. As shown in Figure 2.6, the B1 bond is more covalent in nature while the B2 is more ionic. The covalent bonding

increases with the amount of SiO_2, and increases the stability towards chemical weathering. Therefore, the formation energy of B1 is relatively larger compared to the B2 resulting in easy dissociation of the B2 bond at higher growth temperature. The (100) plane is composed of only B2 bond while the planes of (111), (200), (220) and (311) consists of the B1 bonds together (Liu et al, 2014). The Si–O and Si–Si bonds are characterized by a dissociation energy of 8.26 eV and 3.29 eV, respectively (Weast *et al*, 1968).

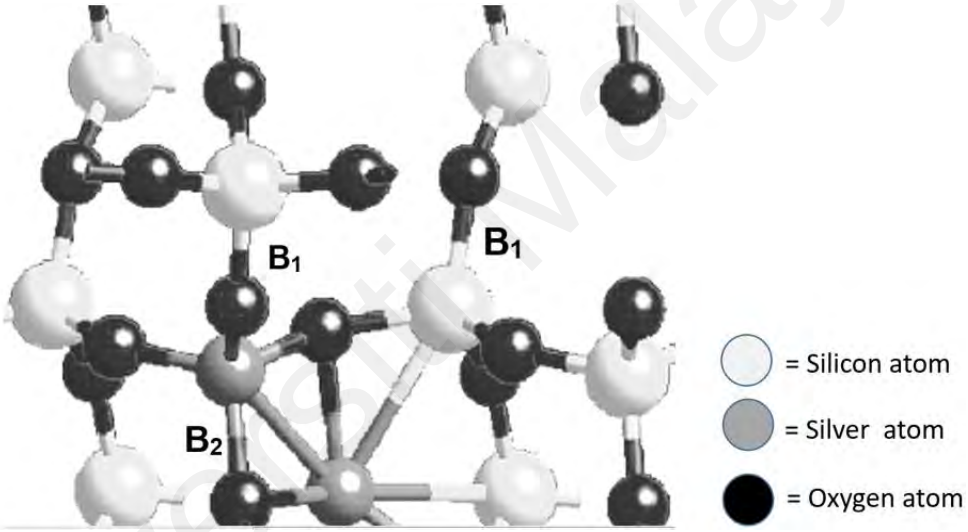

Figure 2.6: Shows a typical Ag-SiO_2 NC (Scheerschmidt, 2007)

2.4.1 Morphology of Ag-SiO_2 NC

The functionalities of Ag-SiO_2 NC can be understood through the morphology of its nanostructures and from the correlation between the size, shape and the optical properties of the nanostructure. These analyses define the specific functionalities of the Ag-SiO_2 NC with the incorporation of AgNPs onto the surface of the silica nanoparticles. The arrangement and dispersion of AgNPs provide an understanding of the optical behavior

of the nanocomposites (Huayan *et al*, 2015). There is a strong correlation between the concentration and AgNPs dispersion on the silica nanoparticles as shown in Figure 2.7 (Jasiorski *et al*, 2014). It is suggested that during the synthesis process, the AgNPs are encapsulated by the SiO_2 as shown in Figure 2.8, and as a result the absorption peak of SPR is reduced compared to the pure silver. The binding of AgNPs on the surface of SiO_2 with the OH^{-1} functional groups occurs due to the present of stabilizers (Eremenko *et al*, 2010).

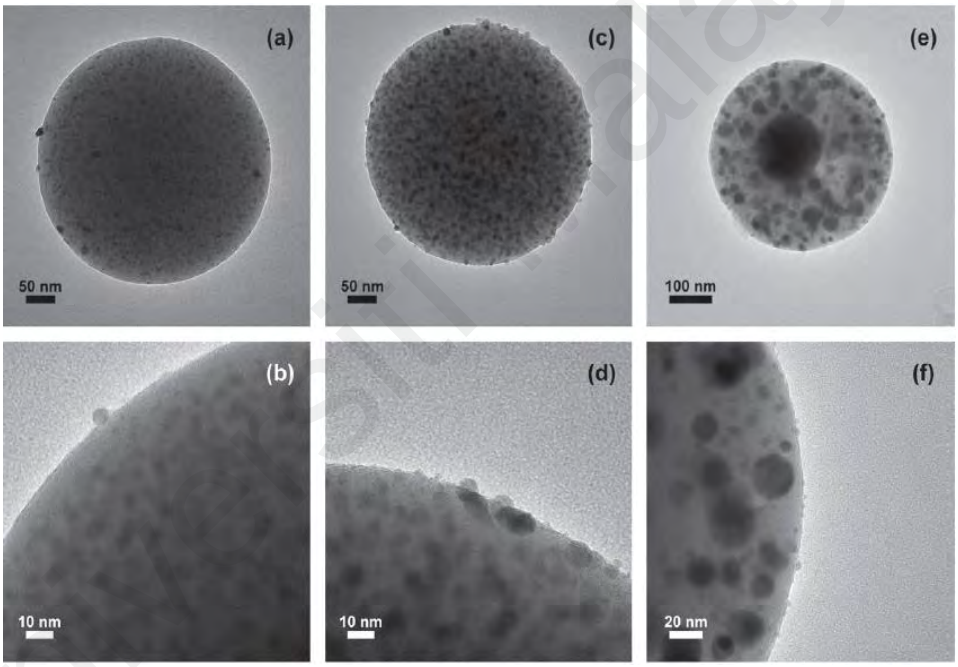

Figure 2.7: TEM images showing SiO_2 spheres with 12% (a and b), 20% (c and d), 50% (e and f) concentration of AgNPs (Jasiorski *et al.*, 2014).

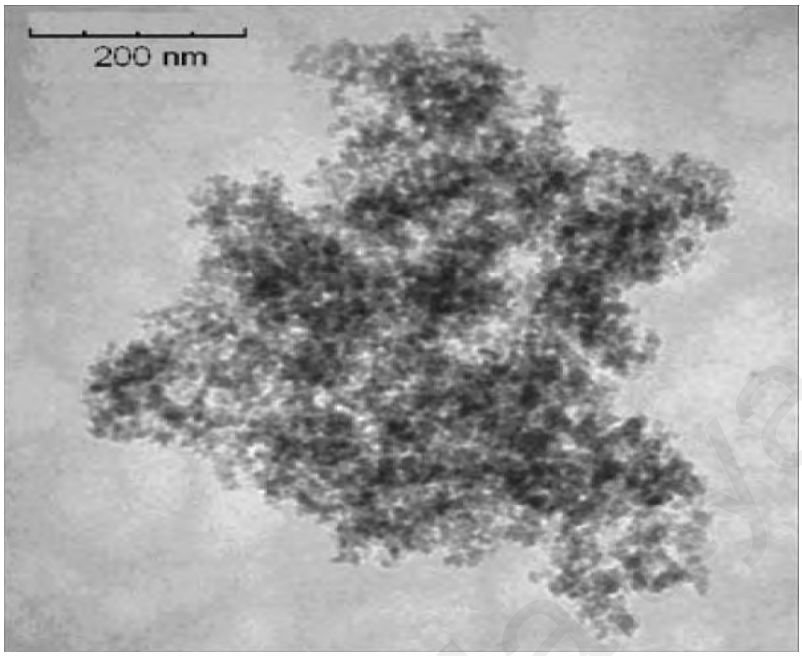

Figure 2.8: TEM of Ag/SiO_2 powder (0.05% Ag) (Eremenko *et al.*, 2010).

2.4.2 Structural Properties of Ag-SiO_2 NC

X-ray diffraction technique (XRD) reveals the information pertaining to the crystallographic structure, physical properties and chemical composition of materials. This technique is based on analyzing the scattered pattern of an X-ray incident radiation hitting a sample as a function of incident and scattering angle, polarization, and wavelength or energy. Figure 2.9 shows the comparison of the XRD pattern between pure SiO_2 and Ag-SiO_2 NC (Nguyen *et al.*,2013). The series of peaks in Figure 2.9 (b) clearly visible at $2\theta = 38°$, 44.2°, 64.2° and 77.2° shows the presence of AgNPs within the nanostructure which is not seen in Figure 2.9 (a).

Jasiorski et al. (2014) established a correlation between the intensity of the peak and the concentration degree of AgNPs. They reported that the characteristic of the diffraction peaks representing pure metallic silver are insignificant at low concentration but are clearly visible at $2\theta = 38°$, 44° and 64° with the increasing of concentration of AgNPs as shown in Figure 2.10.

Another correlation between the intensity of the diffraction peaks and the amount of silver in the material where the composites exhibit similar pattern with four well-resolved diffraction peaks which are found at 2θ angles of 37.9° , 44.1° , 64.3° and 77.2° in the range of 10° to 80° and indexed to the (111), (200), (220), and (311) as reflections indicating the presence of AgNPs as a crystalline structure embedded on the surface of SiO_2. The work also confirms that the average size of the AgNPs are relatively small as shown by the narrow size of the peaks in Figure 2.11 (Wu *et al.*, 2016).

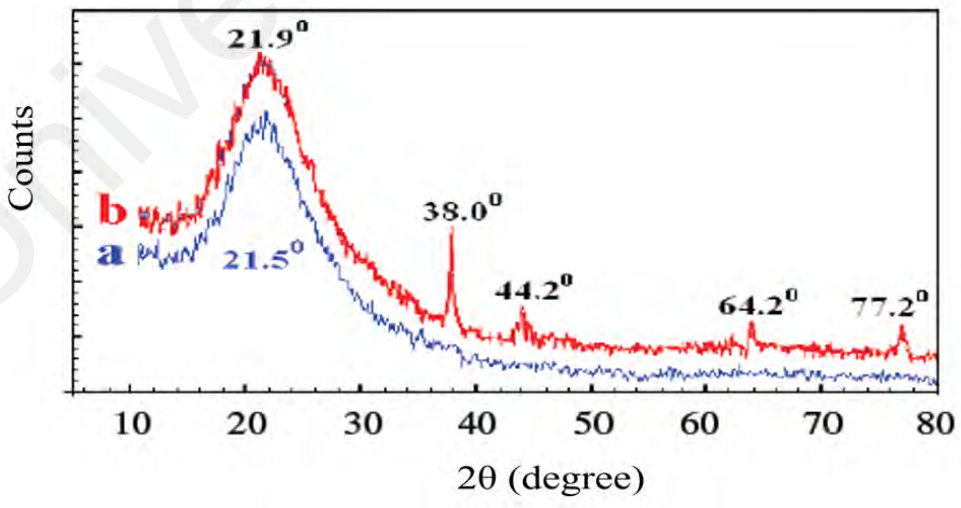

Figure 2.9: XRD patterns of (a) pure SiO_2 and (b) Ag-SiO_2NCs (Nguyen *et al.*,2013).

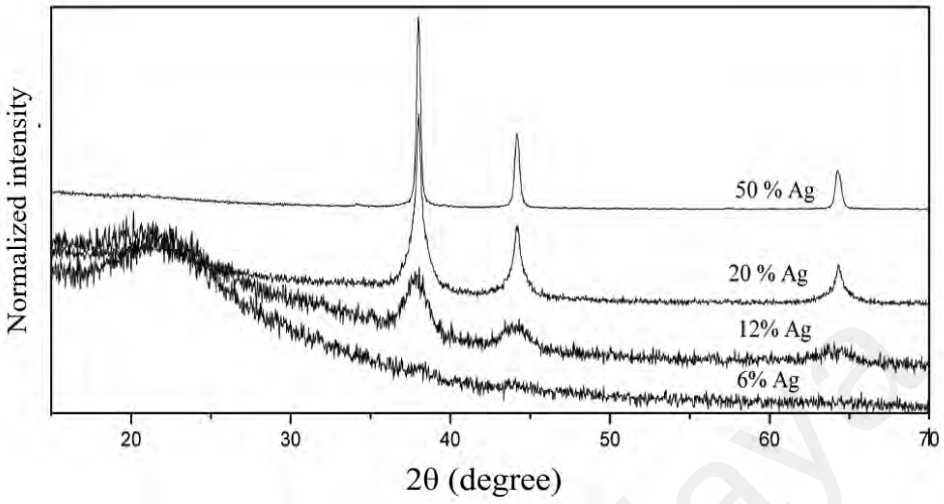

Figure 2.10: XRD diffraction patterns of amino-functionalized SiO_2 spheres with different concentration of AgNPs (Jasiorski *et al.*, 2014).

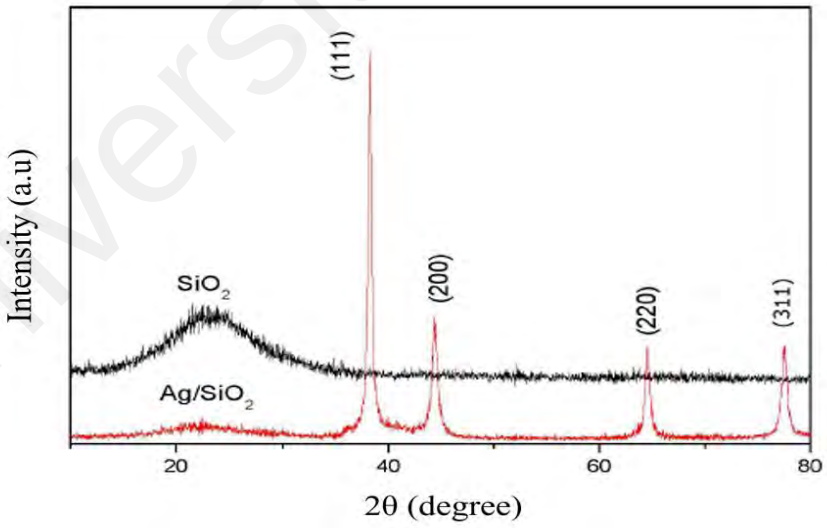

Figure 2.11: XRD spectra showing the effect of average size of AgNPs present in SiO_2 composite (Wu *et al.*, 2016).

2.4.3 Optical Properties of Ag-SiO_2 NC

The optical properties of $AgSiO_2$ depend on the doping variation of the AgNPs. By varying the parameters of AgNPs inclusions into a SiO_2 dielectric host, it is possible to attain the desirable optical properties of the nanocomposite. Various concentrations of AgNPs could control the amount of AgNPs dispersed in the host matrix. This determines the magnitude of the electric or magnetic dipolar response in the far-field. The increase in concentration or molar ratio of AgNPs increases the absorption peak of the host matrix (Rameshkumar *et al.*, 2013; Jasiorski et al., 2014; Shibata *et al.*,1998) as shown in Figures 2.12 – Figure 2.14. The absorption peak is red shifted with the increase of the AgNPs size, while a blue shift is observed when the size is decreased. Figure 2.13 shows the broad absorption peak which shows the decrease in the size of the nanoparticles within the nanostructure. Figure 2.14 shows the effect of molar ratio of AgNP/SiO_2 on the UV-Vis spectra. The absorption peak increased with the amount of AgNPs.

It is reported from previous work that the SPR absorption is not just sensitive to the properties of the particles size and shape, but also to the surrounding medium. A red shift is observed for smaller particles, if the AgNPs is dominated by the configuration of the dielectric (Liz-Marzan *et al.*, 1996). According to the Mie's scattering theory, the dipole absorption due to electric field is oriented along the interparticle axis within the nanostructure specified plane which contributes to a significant red shift of the absorption peak (Xu *et al.*, 2006).

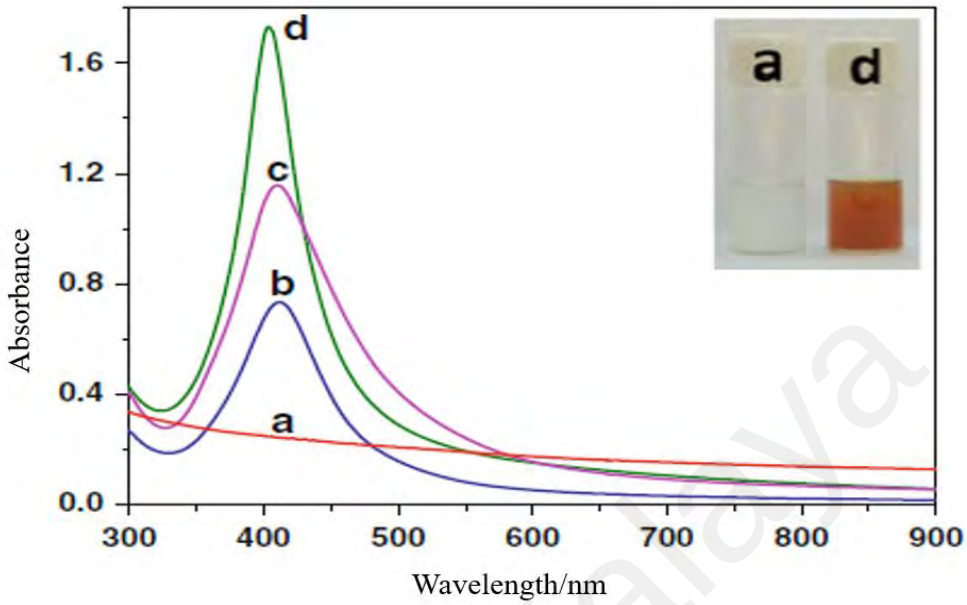

Figure 2.12: A typical surface plasmon absorption spectra obtained from pure SiO_2 (a) and Ag-SiO_2 NC at various concentration; SiO_2/Ag (1mM) NPs (b), SiO_2/Ag (2 mM) NPs (c), and SiO_2/Ag (3 mM) NPs (d). (Rameshkumar *et al.*, 2013).

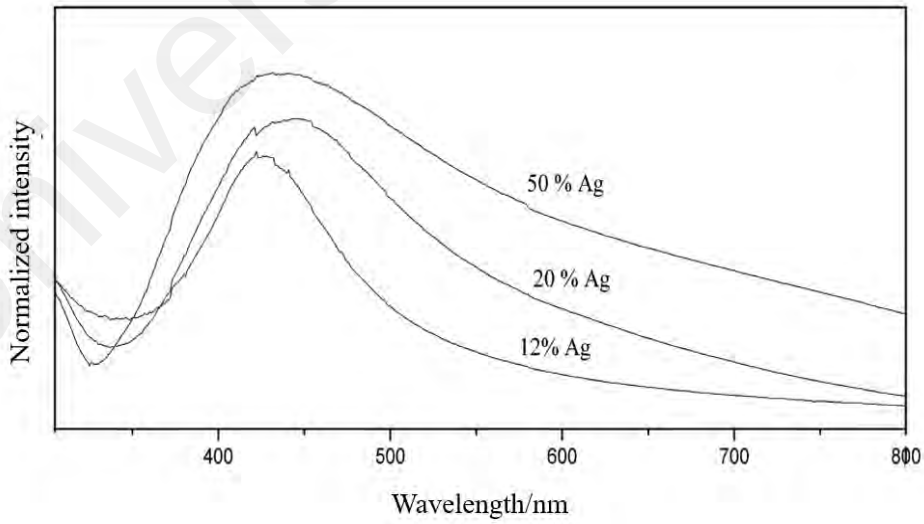

Figure 2.13: Absorption spectra of SiO_2 spheres with the increase of Ag concentration of nanoparticles (Jasiorski *et al.*, 2014).

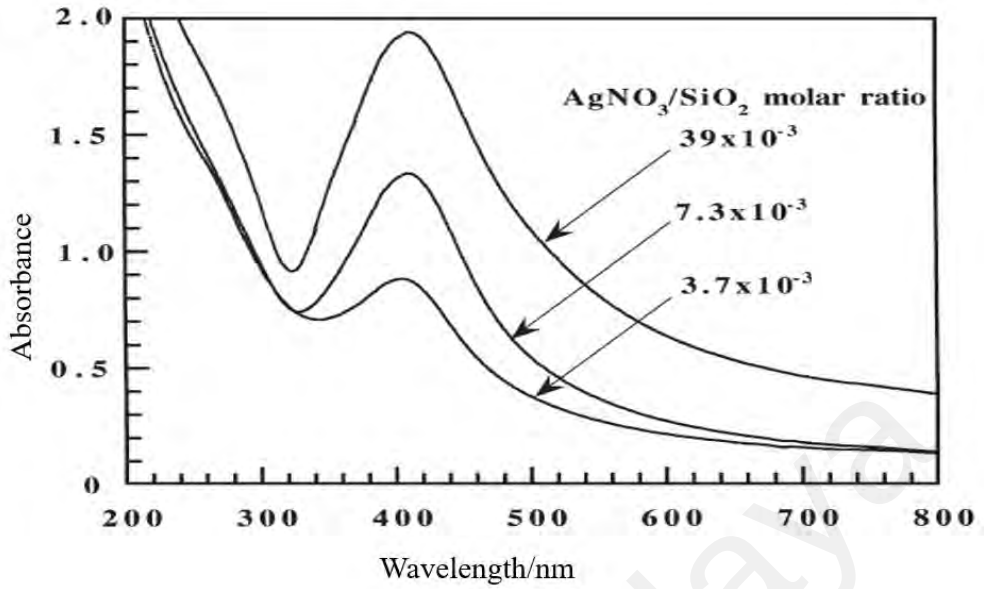

Figure 2.14: Absorption spectra of Ag/SiO_2 with the increased in molar ratio of $AgNP/SiO_2$ (Shibata *et al.*, 1998).

2.4.4 Dielectric Properties of Ag-SiO_2 NC

The electromagnetic properties of Ag-SiO NC is usually characterized by the dielectric permittivity ε and its magnetic permeability μ, while another essential parameter such as the refractive index ($n = \sqrt{\mu\varepsilon}$) can be determined accordingly. The Ag-SiO_2 NC have a relative permittivity based on $\varepsilon_r = \varepsilon/\varepsilon_o$ in which usually larger than unity and the relative permeability, $\mu_r = \mu/\mu_o$ is also approximately unity, where the ε_o and μ_o is the permittivity and permeability of free space or air, respectively. Nanoscience and technology has made it conceivable to tailor these dielectric properties by varying the nanometal dispersion according to future applications.

The ability to affect the dielectric properties of a nanostructure requires constituting entities, so-called meta-atoms, with a strong magnetic or electric dipolar response. These meta-atoms act as an integrated unit to construct a pattern which must be smaller than the light's wavelength if a spatially homogeneous response in the far-field is desired. These geometry properties of the elements within the unit cells determine the primary resonance of both dielectric permittivity and the magnetic permeability (Christoph *et al.*, 2014).

As for the Ag-SiO_2 NC, the Maxwell Garnett model is frequently used to predict the effective permittivity (ε_{eff}) of the nanocomposite, formed by two constituting entities which is the spherical inclusions, (ε_i) and the host matrix, (ε_h) as shown in equation 2.5:

$$\varepsilon_{eff} = \varepsilon_h \frac{\varepsilon_i(1 + 2f) + 2\varepsilon_h(1-f)}{\varepsilon_i(1-f) + \varepsilon_h(2+f)} \quad (2.5)$$

where f is the volume fraction (filling factor) of the spherical inclusion, (ε_i) (ranging from 0 to 1).

The Maxwell Garnett mixing formula does not provide any adjustable parameters to account for any changes in the geometry which keep the filling fractions unchanged. Therefore, the only way to distinguish the "host" from the "inclusion" is that the filling fraction of the former is much larger than the latter. Thus, at higher filling fraction, the model is unstable due to the asymmetric build up of the metal inclusions and the matrix host with the increase in the inclusions concentrations (Chaumet *et al.*, 1998).

In the previous work, the MG theory is used to study the effective permittivity of Ag-SiO_2 NC by varying the amount of metal nanoparticles in the dielectric (Moiseev S.G *et al.,* 2010). The permittivity of the synthesized AgNPs is used as the spherical inclusions, (ε_i) while the permittivity of silica is used as the host matrix, (ε_h).

2.4.5 Photocatalytic Properties of Ag-SiO_2 NC

As reported from previous research, SiO_2 has low absorption in the visible region of solar spectrum due to its large band gap (9 eV) (Shi *et al.*, 2013) but at the same time, it is the most promising material due to the abundance, cost, stability and nontoxicity (Behara *et al.*, 2016) and has a wide range of applications including catalysts, photonics, chemical-mechanical polishing due to their ordered mesostructured and thermal stability. Due to these advantages, SiO_2 nanoparticles have better photocatalyst efficiency compared to TiO_2 (Zhang *et al.*, 2011; Acosta *et al.*, 2011; Kamegawa *et al.*, 2010).

One of the best mechanism to modify the optical and photo-catalytic properties of SiO_2 is by doping the nanostructure with noble metals such as Au, Ag and Pt which can be coupled to the nanostructure and improves the separation of charge carrier and as well as photon absorption (Subramanian *et al.*, 2004; Paramasivam *et al.*,2008; Mokari *et al.*,2005). The SPR effect from these noble metals especially AgNPs, is due to the coherent oscillation of free electrons stimulated by the visible light with certain characteristic electromagnetic frequency.

The excitation of free electron conduction generates local electromagnetic fields near the metal surface which then benefits the facile formation of electron and proton pairs in the vicinity of the semiconductor (Ingram *et al.*, 2011; Awazu *et al.*, 2008; Thimsen *et al.*, 2011; Hua *et al.*,2012). Thus, SiO_2 doped with AgNPs offers a good electronic properties, photochemically stable, responsive to solar-irradiation, having the oxidation and reduction potential for hydrogen generation (Alfaifi et al., 2018).

There are two different mechanisms in the plasmonic photocatalytic activity. The first mechanism is based on the absorption of visible light by the noble metal NPs which leads to the generation of photocarriers at the semiconductor-metal surface. This initiates the redox reactions on the plasmonic photocatalyst surface. This mechanism strongly depends on the movement transfer of the generated electrons and/or holes from the noble metals to the semiconductor (Wang *et al.*, 2012). The second mechanism is based on the SPR-induced electric field which enhances the rate of the formation of electron and proton pairs. This process benefits from the localized electromagnetic energy at the semiconductor surfaces (Yu *et al*., 2019).

2.5 Synthesis of Nanocomposite materials

Numerous methods and processes can be utilized to produce plasmonic nanocomposites. These methods and techniques have their own advantages and disadvantages. In this study, the focus is towards a simple and effective experimental method for producing metal-dielectric nanostructure that possess novel properties that is not found in nature such as negative permittivity at the optimum filling fraction ratio based on the Effective Medium Theory (EMT). There are generally two methods to synthesize nanocomposites; the top down and bottom up approach (Natsuki *et al.*, 2015).

2.5.1 Top-down Method

The objective of the top-down method is to reduce the bulk macroscopic size particles into the nano size particles. This technique is not suitable to produce uniformly shaped particles due to the difficulties in controlling the experimental conditions. The top-down method is a physically intensive and extremely diverse method. Nanomaterials that are formed from the top-down technique can be categorized into mechanical-energy, high-energy, thermal, chemical, lithographic and natural methods.

2.5.2 Bottom-up Method

The bottom-up methods are much better in generating uniform particles, distinct size and shape. This method begins with the atoms that aggregate in the solution or even in the gas phase to produce particles of definite sizes. The problems of this method is related to the stability issues, as the particles are dispersed in aqueous suspension the particles posses high mobility, thus have collide with each other and form a clusters and aggregations. The bottom-up methods can be categorized into the gas-phase, liquid-phase and lithographic methods. The sol-gel method falls in the category of the liquid-phase (bottom-up methods). There are two type of the liquid phase method which is the liquid and sedimentation method. The sol gel technique falls in sedimentation method (Hornyak *et al.*, 2008).

2.6 Sol-Gel Technique

The sol–gel technique is a sedimentation method which falls under the bottom-up category of nanocomposite synthesis. It has been used extensively in oxide film fabrication due to the flexibility of the preparation steps. Besides this, it is also widely used as the synthesis method of metal oxide composite. It is a well known wet-chemical process which is widely used in the area of materials science and ceramic engineering. It is a means of preparing the dispersion of materials through the growth of nanometals within the nanostructure of the composite. Materials fabricated by the sol–gel method usually possess a developed structure of pores with different size, in which the stabilization of nanoparticles in the different chemical nature is feasible.

Sol-gel chemistry is based on the inorganic polymerization reactions. The metal-polymers nanostructures can be produced through the process of hydrolysis and condensation with the present of metal alkoxides ($M(OR)_n$ as the precursors. In this expression, M = Ti, Si, Zr, Al, Sn, while OR is the alkoxy (- O- CH_3) group, and *n* is the valence state of the metal (Blanchard *et al.*, 1998).

The sol-gel reactions promote the growth of colloidal solution (*sol*) that acts as precursors and their subsequent network formation (*gel*) through hydrolysis and condensation reactions of inorganic alkoxide monomers. The use of metal alkoxides are common because they readily react with water. The widely used metal alkoxides are Tetraethylorthosilicate (TEOS) and Tetramethoxysilane (TMOS). The chemical procedure involves the '*sol*' (or solution) which slowly changes to form a gel-like diphasic system which contain both the liquid and solid phases, where the morphologies range from discrete nanoparticles to continuos polymer networks. With regards to the

ratio of the metal-colloid and the host matrix (gel-like), the volume fraction (or filling fraction) of the colloid should be kept low or at optimum ratio for the gel-like properties to be realized. To accomplish this, the process will allow the time for the sedimentation to occur, and then poured off or sucked from the remaining liquid or by the use of centrifugation to accelerate the process of phase separation. Then, the system undergoes a drying process to remove the remaining liquid (solvent) and is usually followed by substantial amount of shrinkage and densification. The speed of which the solvent can be removed is ultimately determined by the distribution of nanoparticles in the gel (C.J. Brinker *et al.*, 1990).

There are 5 different routes of the sol-gel processing; hydrolisis and condensation of metal alkoxides, non-hydrolytic sol-gel reactions, Pechini gel methods, polymer pyrolysis, inorganic-organic hybrids and colloidal dispersion as summarized in Figure 2.15.

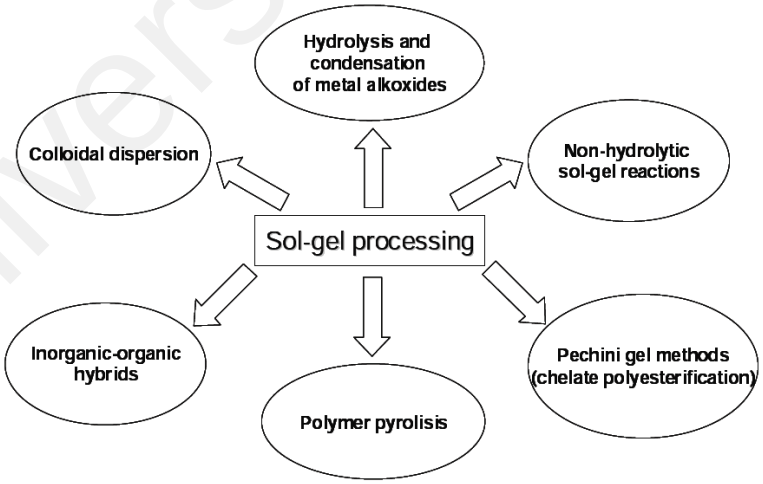

Figure 2.15: Different routes of the sol-gel processing (Dimitrev *et al*., 2008).

2.6.1 Hydrolysis and Condensation of Metal Alkoxides Sol-Gel

In this process, the metal alkoxides, such as Tetramethoxysilane (TMOS) and Tetraethyl orthosilicate (TEOS) will undergo a series of hydrolysis and condensation reactions to produce the sols and gels. Firstly, the alkoxy groups (Si-OR) will undergo a hydrolysis process and then followed by the condensation reaction which generates the silanol groups (Si-OH), which then condense into the Si-O-Si bonds by alcohol. The two stage process of alkoxy polymerizations is the main difference compared to the common organic polymerization reactions. Besides TEOS, other alkoxides which commonly are used in this process are the aluminates, zirconates and titanates but are only used with much smaller scale and is used with other kind of materials such as the TMOS and TEOS (Brinker *et al.*, 1990).

2.6.2 Non-Hydrolytic Sol-Gel Reactions

The non-hydrolytic sol-gel reactions or coined as non-hydrolytic sol-gel chemistry (NHSG) is a process of producing mesoporous materials to obtained highly homogeneous dispersion of metal within the nanocomposite in the absence of water. As no water is used throughout the synthesis, the alkoxide will act as the oxygen donor. Although the volatile organic solvents were easily removed in this simple method (Acosta *et al.*, 1994), the reaction rates are slower compared to the hydrolytic sol-gel (Le Roux *et al.*,1998; Wakabayashi *et al.*,2010; Hagiwara *et al.*,2008 Bassindale *et al.*, 2003). Other oxygen donors used in this process are ethers, carboxylates and carboxylic acids.

2.6.3 Pechini Sol-Gel Methods (chelate polyesterification)

The Pechini Process is referred as the entrapment of cations in a polymer network in order to avoid the building up of multiple phases of binary oxides in the common hydrolysis and condensation rates. This method is used for systems containing multiple cations compared to the common system which involves a single cation (Nishio *et al.*, 2004). In this process, citric acid is used as the chelating agent to surround and entrap the cations. Then, the chelated cations will be immobilized by the formation of polymer network in a gel or resin. Under oxidizing conditions, the product is then combusted to remove any organic content and yields homogeneously dispersed cations in an oxide product (Chen *et al.*, 2018).

2.6.4 Polymer Pyrolysis Sol-Gel

Polymer pyrolysis process is a sol gel technique to produce nanostructured multicomponent composite/ceramics with an exceptional thermal stability at a very high temperature more than 2000 °C. The yield of oxidation resistance is better than chemical vapor deposition grade polycrystalline carbides or nitrides (Iacona et al.,2000 ; Raj. *et al.*, 2001). There are two essential steps in this process. Firstly, the hybrid sol-gel nanostructures of multicomponent composite/ceramic are synthesized from the metal alkoxides modified with organics or inorganic materials. Secondly, under controlled conditions, these nanostructures are pyrolyzed into ceramics. The thermal process is conducted in a high temperature of more 1000 °C until an amorphous covalent ceramic is achieved (Riedel *et al.*, 1996). The change of phase and microstructure of the final product depends on the metal oxide content (Ceccato *et al.*, 2003).

2.6.5 Inorganic-Organic Hybrids Sol-Gel

In this sol-gel category, the metal alkoxide and a polymer in common solvent is used as the co-dissolved precursor. With a small amount of catalyst to catalyze the reactions which consist of hydrolysis, alcoxolation and oxolation (Orgaz *et al.*, 1998), the processes are concurrently governed by the solvent, water and pH, with other manipulated parameters such as the ratio of the alkoxide, type of catalyst, temperature and concentration (Livage *et al.*, 1988). The preparations of the hybrid organic-inorganic membranes are given strong attention due to their utilitarian physical properties. The applications of such polymers with high organic groups are seen in biomaterials, membranes, coatings, optics and electronics. The combination of characteristics of both organic polymers and inorganic compounds enable these novel nanostructures to obtain respectable optical, electrical and mechanical properties (Ebert *et al.*, 2004).

2.6.6 Colloidal Dispersion Sol-Gel

A colloidal dispersion sol-gel is composed of nanosize particles homogeneously distributed by a dispersing medium. The type of dispersing medium could vary from very polar solvents such as water or formamide to highly non-polar solvents such as tolune or alkanes depending the nature and surface chemistry of the nanosize particles. The nanosize particles are also subjected to the Brownian motion. The Brownian motion is directly dependent on the solvent temperature. The rate of diffusion of the nanosize particles then depends on its size and shape and the solvent viscosity. As for the spherical shape, the diffusion rate increases with the decrease in the particle radius. For the smaller

size particles, the sedimentation process under the gravitational forces is slower compared to the larger particles. The smaller particles have greater advantages as the gravity prevents the particles from settling while the thermal motion is a significant factor in keeping the nanosize particles homogeneously distributed. (Matter *et al.*, 2020).

CHAPTER THREE:

RESEARCH METHODOLOGY

3.1 Introduction

In this chapter, all experimental setups for the synthesis of AgNPs and Ag-SiO_2 NC will be described in detail. The main objective is to synthesize a stable AgNPs suspended in colloidal solution and Ag-SiO_2 NC at various volume fraction using sol-gel technique and characterize the samples for their morphology, optical, thermal. structural and electrochemical properties.

In this work, the samples are prepared in two steps process.

- Step 1 : Synthesis of spherical AgNPs dissolved in deionized water at constant concentration with high homogeneity.
- Step 2: Synthesis of five (5) samples of Ag-SiO_2 NC with varied volume ratio of AgNPs/SiO_2 with sol-gel technique for further characterization.

The characterization techniques used on the samples are also presented in this chapter. The prepared samples were directly tested using Ultraviolet Visible (UV-Vis) Spectroscopy, Photoluminescence Spectroscopy (PL), Field Emission Scanning Electron Microscopy (FESEM), Transmission Electron Microscopy (TEM), Ellipsometry Spectroscopy, X-ray diffraction (XRD), Fourier Transform Infrared (FTIR) spectroscopy, Differential Scanning Calorimetry (DSC), Thermogravimetric analysis (TGA), Surface Enhanced Raman Spectroscopy (SERS) and Electrochemical Impedance Spectroscopy (EIS).

3.2 Materials

All chemicals were used without further purification. Daxad 19 (Sodium Naphthalene Sulfonate Formaldehyde Condensate) (MW800) (CAS Number:36290-04-7) (Canamara) as a stabilizer, Silver Nitrate ($AgNO_3$) (CAS Number: 7761-88-8) (Fisher Scientific) as the silver source and Polyethylene glycol (PEG) (CAS Number: 25322-63-4) (Agros Organic) as the reducing agent. Special grade reagents of Tetraethylorthosilicate (TEOS, CAS number: 78-10-4, Aldrich, 98%) and ethanol (CAS Number: 64-17-5, RM Chemicals) (99.5%) were used for sol-gel process.

Ammonia (35% aqueous solution)(CAS Number: 7664-41-7, RM Chemicals) and Ammonium Fluoride (CAS Number: 12125-01-8, RM Chemicals) were used to prepare the catalysts solution for the sol-gel reaction of TEOS. Deionized water was used in all preparation for aqueous solution. The used of PEG is to stabilized the AgNPs to avoid any changes in its physical and optical properties at room temperature(Luo *et al.*, 2005). Figure 3.1 shows the complete overview of the research methodogy. The dispersion of Ag-SiO_2 NC in the EPD process using 2-propanol (CAS Number : 67-63-0, RM Chemicals). Ag-SiO_2 NC were separately deposited onto several ITO glass substrates (Magna Value Supplies, Malaysia, thickness 2500 nm, sheet resistance $\leq 7\ \Omega$/sq).

3.3 The Overview of Research Methodology

The methodology of the research works are semmarized as follows:

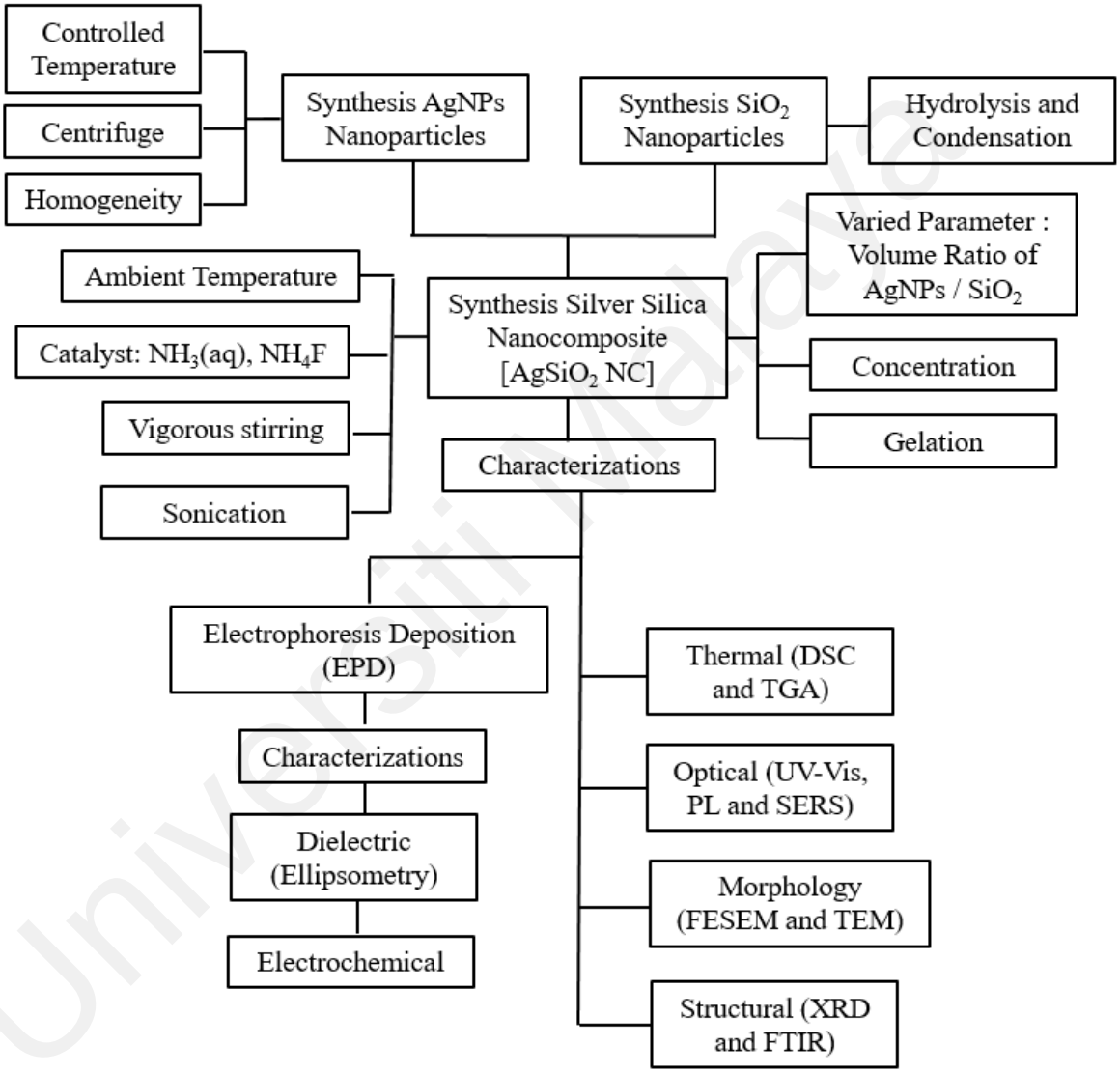

Figure 3.1 : Summary of research methodology

3.4 Synthesis of Silver Nanoparticles (AgNPs)

The preparation of AgNPs consists of three (3) phases. Phase I ; Nucleation and Growth of AgNPs, Phase II; Purification of AgNPs via centrifuge and Phase III ; Preparation of AgNPs colloids solution.

3.4.1 Nucleation and Growth of AgNPs

AgNPs were synthesized by chemical reduction methods using Silver Nitrate [Formula:$AgNO_3$] as the precursor with Polyethylene Glycol (PEG) [formula : $H(OCH_2CH_2)_nOH$] as the reduction agent and Daxad 19 (Sodium Naphthalene Sulfonate Formaldehyde Condensate [Formula : $C_{12}H_{14}Na_2O_6S_2$]) as the stabilizer. In this work, 4.5 g Polyethylene Glycol (PEG) and 5 g of Daxad 19 (were dissolved through deoinized water under magnetic stirring. As shown in Figure 3.2, the solution turn to light brown color then heated and maintained to 80^o C. The temperature is very important in order to produce a spherical and homogeneous silver nanoparticles. Then, 4 g of $AgNO_3$ was dissolved into the solution. The mixed solution turn to grey-black color indicated the formation of AgNPs. The solution is then stirred for 1h with the temperature maintained at 80^o C to obtain spherical shape (Che Lah *et al.*, 2011). The process is described in the following equation:

$$2HOCH_2–CH_2\,OH \rightarrow 2CH_3CHO + 2H_2O \qquad (3.1)$$

$$2CH_3CHO + 2AgNO_3 \xrightarrow[\text{reduction process}]{C_{21}H_{14}Na_2O_6S_2} CH_3CO–COCH_3 + 2Ag + 2HNO_3 \qquad (3.2)$$

Figure 3.2: Chemical reduction of $AgNO_3$ to AgNPs

Figure 3.3: Centrifuge machine

3.4.2 Purification of AgNPs

The solution was cooled to room temperature and prepared for centrifugation. The centrifuge is used in this work for the purification process which is to separate the samples from PEG and Daxad 19 residue. The 150 mL cylinder container was used to fill with silver solution. Using the Hettich Zentrifugen EBA 12 as shown in Figure 3.3, several 150 mL cylinders were placed in the centrifuged machine. The internal feature of the machine is shown in Figure 3.4. The centrifuge machine was set at 6000 rpm for 20 minutes. Once the cylinder is removed, the percipitated AgNPs was found at the bottom of the cylinder as shown in Figure 3.5. The inhaled solution was suctioned out of the cylinder and left to find the AgNPs. Once it has been completely dried, the precipitated metal is washed again by using distilled water. The washing process was repeated for 3 times. In the last step of the centrifuge, after the solution is removed, the metal percipitate is washed with acetone solution. by filling the cylinder containing the precipitated metal with acetone and centrifuged again. Then, the acetone solution is removed and dried. At this final step, the purification of AgNPs was obtained, represented by glossy metal percipitate as shown in Figure 3.6. The precipitated AgNPs is dried at room temperature with a grey-white shinning color as shown in Figure 3.7. The AgNPs powder that has been produced is stored in a mini glass bottle as shown in Figure 3.8.

Figure 3.4: Centrifuge machine with internal setting

Figure 3.5: First step of centrifuge process. Visible precipitation at the bottom of clear 150 mL tube cylinder container.

Figure 3.6: Final step of centrifuge process. Shining silver precipitation at the bottom of the 150 mL cylinder.

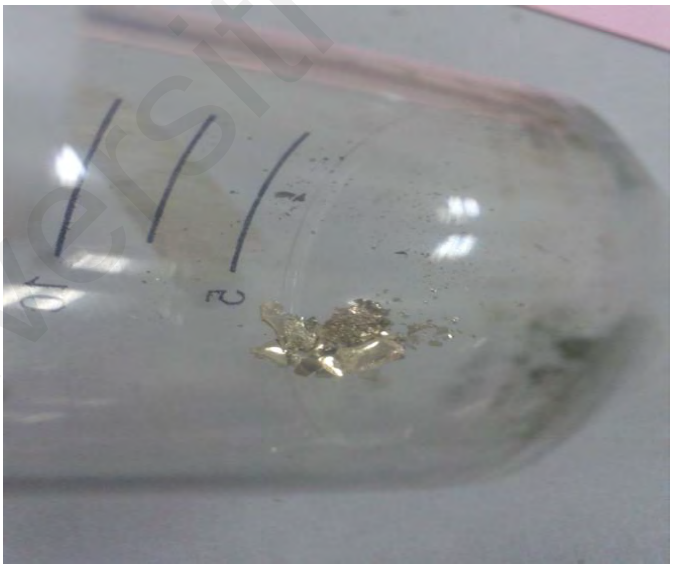

Figure 3.7: AgNPs at the end of centrifuge process.

Figure 3.8: AgNPs for storage in mini glass bottle

3.4.3 Preparation of AgNPs in Colloids

The freshly prepared AgNPs is then dissolved and dispersed in deionized water to form a homogenous colloidal solution at 50 mM. The colour of AgNPs colloids solution is reddish brown as shown in Figure 3.9.

The concentration of AgNPs colloids is given as;

A) Numbers of mole of AgNPs

i) Sample mass = 0.27 g

ii) Molar mass of Ag =107.87g

Numbers of mole :

Numbers of mole

$$\frac{\text{Sample of AgNPs}}{\text{Molar Mass AgNPs}} = \frac{0.27}{107.87} = 0.0025 \text{ mole} \quad (3.3)$$

B) AgNPs colloid concentration

$$\frac{MV}{1000} = \text{numbers of mole} \quad (3.4)$$

$$\frac{M(50 \text{ mL})}{1000} = 0.0025 \text{ mole}$$

$$M = 0.05 \text{ M } (50 \text{ mM})$$

Figure 3.9: AgNPs suspended in colloid solution

3.5 Preparation of Catalyst Solution for Ag-SiO_2 NC Synthesis

The following reagents were used to synthesis the catalyst solution:

i) Dionized water (18 mL)

ii) 0.07 mL of 30% aqueous ammonia (NH_3) (RM Chemicals) with M=17.03g/mol is used as the main component of catalyst.

iii) 0.3 mL of 0.5 M Amonium Fluoride (RM Chemicals, M=37.04g/mol) is used as a buffer for the catalyst. The preparation of Amonium Fluoride solution as follows:

$$\frac{M(V)}{1000} = \frac{\text{mass sample of } NH_4F}{\text{Molar mass of } NH_4F} \quad (3.5)$$

The chemical used in this section are shown in Figure 3.10.

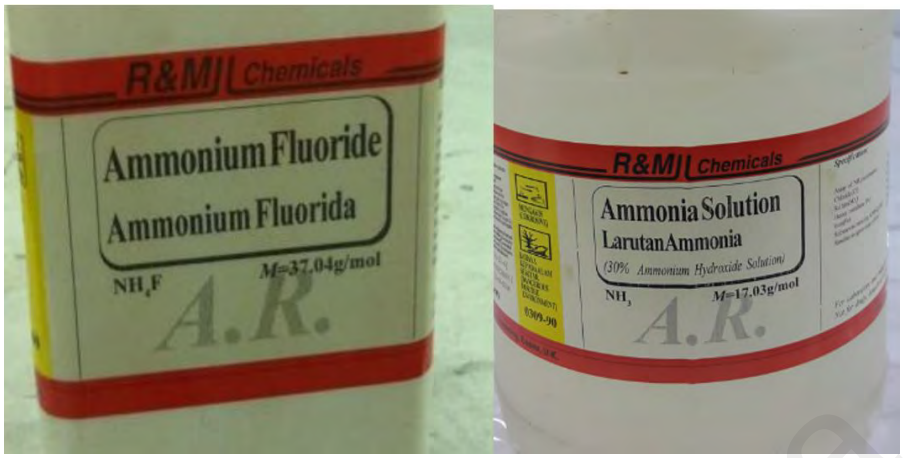

Figure 3.10: Ammonium Fluoride and Ammonium Solution used in this research.

3.6 Synthesis of Silica Nanoparticles

In this process, special grade reagents of alkoxide; Tetraethylorthosilicate or TEOS with the chemical formula $Si(OC_2H_5)_4$) and ethanol (99.5%) were used. 12.5 mL TEOS and 10 mL of ethanol is mixed under vigorous magnetic stirring for 40 minutes to allow the hydrolysis and condensation of TEOS at pH of 9.4. The process is known as hydrolysis because of the combination of hydroxyl ion to silicon atom shown as follows:

Hydrolisis;

$$Si(OC_2H_5)_4 + H_2O \xrightarrow{C_2H_5OH + H_2O} HO\text{-}Si(OC_2H_5)_3 + (OC_2H_5)\text{-}OH \quad (3.6)$$

$$Si(OC_2H_5)_4 + 4\ H_2O \rightarrow Si(OH)_4 + 4\ (OC_2H_5)\text{-}OH \quad (3.7)$$

$Si(OH)_4$ is termed as silicic acid which traditionally is known as synonym for Silica (SiO_2). Depending on the amount of catalyst, the process may reach to completion where all the OR group replaced by OH^{-1} groups.

3.7 Synthesis of Ag-SiO_2 NC

The synthesis of Ag-SiO_2 NC was conducted as follows : AgNPs at constant concentration (50 mM) taken from safe storage, sonicated for 1 hour to avoid aggregation. The sonicated AgNPs were then dispersed in the freshly prepared sol-gel under vigorous magnetic stirring. The solution is then sonicated for 1 hour using a ChromTech sonicator (Taiwan) with 40 kHz frequency and 1200W power as shown in Figure 3.11. After sonication, the prepared catalyst solution was slowly added into the main solution by injection at the rate of about 1.0 mL/min using 5 mL syringe. Immediately after that, the mixture is poured into a plastic lab dish and sonicated again for 1 hour in a sonicator as shown Figure 3.11. The plastic lab dish is arrange in such a way as shown in Figure 3.12 to let the samples to be exposed to room temperature. This will kept the AgNPs dispersed during gelation which preventing aggregation. The samples are then dried at room temperature for 4 days to remove the residues (Kielbasa *et al.*, 2007) as shown in Figure 3.13. The reaction in this process is divided into two main reaction which occurs simultaneously (Kim *et al.*, 2002); condensation reaction of the hydroxyl group with other ethoxy group from other TEOS as expressed in Equation (3.8). and the immobilization of silver onto silica nanostructure expressed as in Equation (3.9).

$$Si(OC_2H_5)_4 + 4\ H_2O \rightarrow Si(OH)_4 + 4\ (OC_2H_5)\text{-}OH \qquad (3.8)$$

$$Si(OH)_4 + Ag^o \rightarrow SiO_2Ag^0 + 2H_2O \qquad (3.9)$$

In order to study the effect of various filling fraction of Ag/SiO_2 on its properties, the whole process is repeated for different volume of AgNPs colloids. Figure 3.13 shows the samples at various filling fraction. The summary of this process are shown in Figure 3.14. A sample of sol-gel without AgNPs is prepared in the same way for comparison. Table 3.1 shows the detailed parameters of the sol-gel preparation.

Table 3.1: Details of sol-gel preparation. Different filling fraction with constant concentration (50 mM) were used.

Sample ID	TEOS (mL)	AgNP (50 mM) (mL)	Fraction AgNPs/TEOS
Ag20	12.5	2.5	0.2
Ag40	12.5	5.0	0.4
Ag60	12.5	7.5	0.6
Ag80	12.5	10.0	0.8
Ag100	12.5	12.5	1.0

Figure 3.11: Picture of Sonication machine

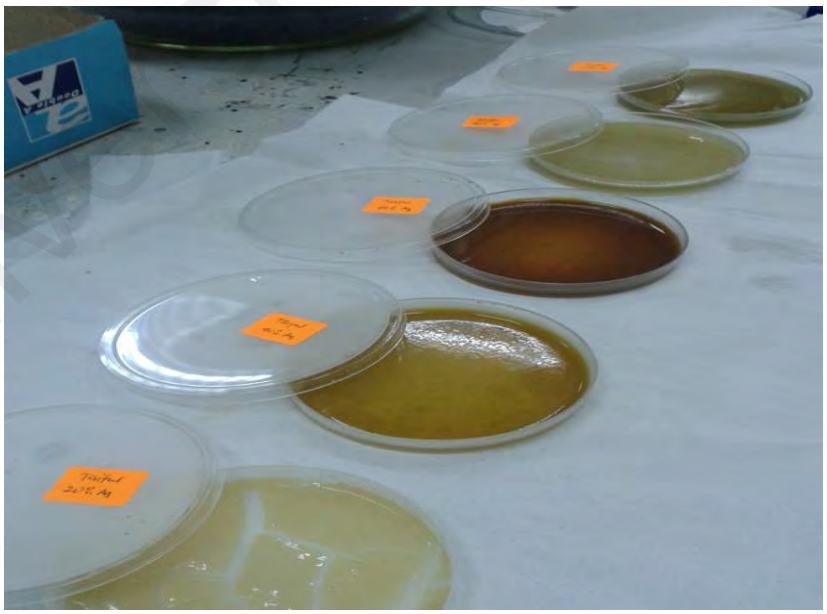

Figure 3.12: Ag-SiO_2 NC samples are prepared for drying process

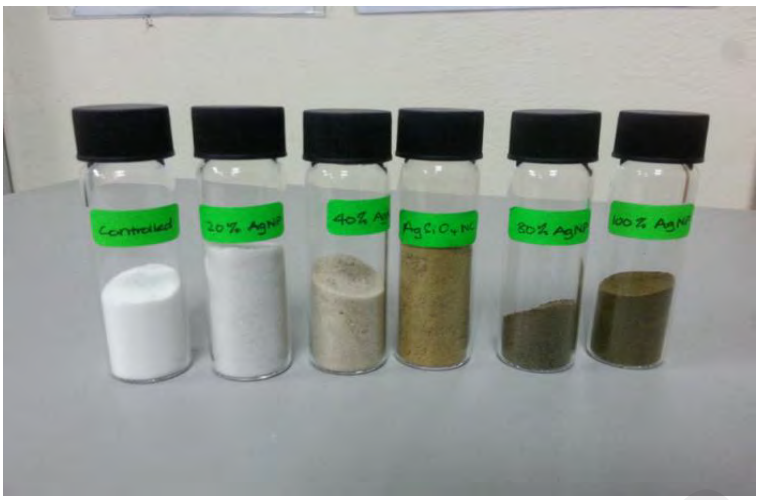

Figure 3.13: Ag-SiO_2 NC Samples powder at different volume ratio

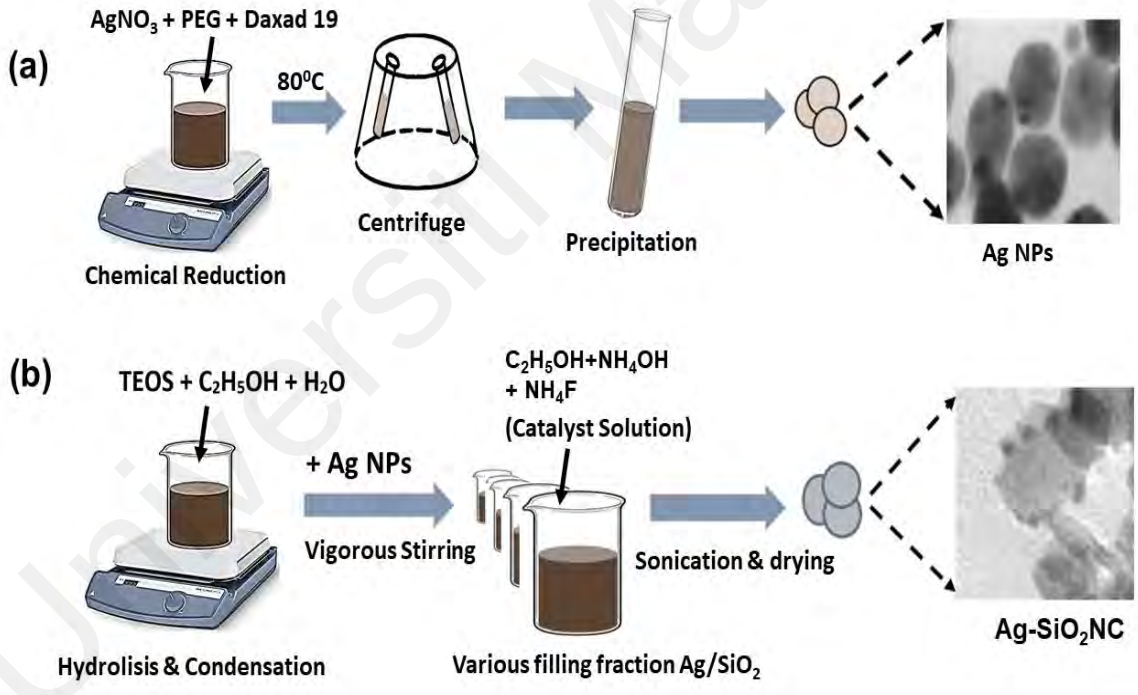

Figure 3.14: Summary of the process ;(a) AgNPs synthesis by chemical reduction technique (b) Nanocomposite synthesis via the sol-gel technique

3.8 Thin film fabrication using electrophoresis technique

3.8.1 Glass slide preparation

Glass slide coated with Indium Tin Oxide (ITO) is used as a substrate for the composite deposition by electrophoresis process. In this preparation, the ITO substrate with thickness of 2.2 mm is cut into small rectangular size slides with the average the size of the slides is 25 x 12.7 mm as in Figure 3.15. The slides were ultrasonically cleaned sequentially using distilled water, acetone and then soaked in ethyl alcohol for 10 minutes. Finally they were sonicated again for 30 minutes. The conductive surface is determine using digital multimeter which shows of an average of 11.0 V and then labelled with non electrosatic tapes

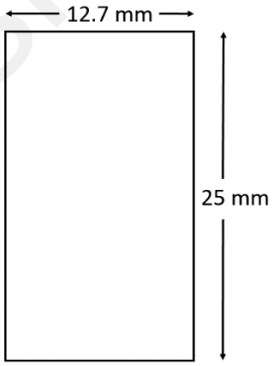

Figure 3.15: ITO Substrate unit for electrophoresis deposition

3.8.2 Electrophoresis Setup

The freshly prepared ITO-coated glass slides is then used as electrode(anode) for Ag-SiO_2 NC deposition and the same glass substrate is used as counter electrode (cathode). The electrodes were assemble in parallel arrangement with a separation of 1 cm to the custom made electrode holder as shown in Figure 3.16. The complete setup of this process is shown in Figure 3.17.

Figure 3.16: Customised electrode holder for electrophoresis process.

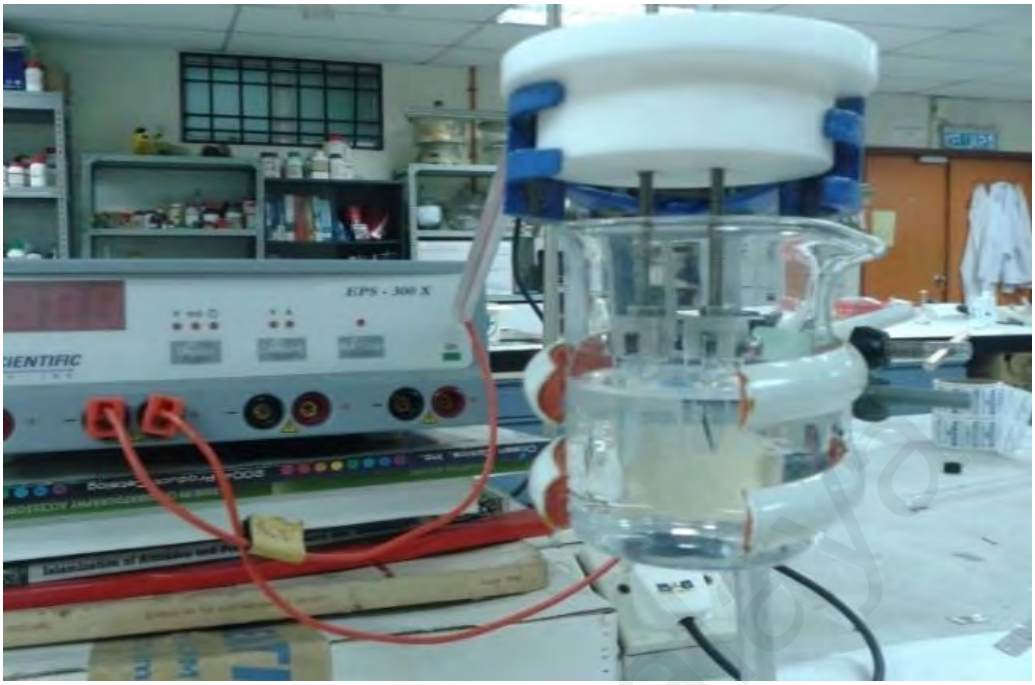

Figure 3.17: Experimental setup for Electrophoresis Deposition(EPD) process showing the control system.

3.8.3 Deposition of Ag-SiO_2 NC onto ITO

The Ag-SiO_2 NC were crushed into powders and dissolved in deionized water. The solution was diluted by 2-propanol to form a solvent-based EPD bath with 10 vol. % Ag-SiO_2 NC (pH =2.5 to 3.0) as show in Figure 3.18. The solvent-based bath is commonly used in the EPD method because it prevents gas generation which hinders the deposition process (Kelly et al., 2016). Prior to deposition process, the solution was then sonicated for an hour to reduce particle agglomeration. The solution is then connected to external circuit by the electrode with a potential difference of 80 V and the deposition process was performed for 5 minutes to obtain a minimum thickness. The ITO substrate with coated Ag-SiO_2 NC thin film [Figure 3.19] was then dried at 50 ºC in a vacuum oven for an hour to eliminate the remnant solvents from the EPD process.

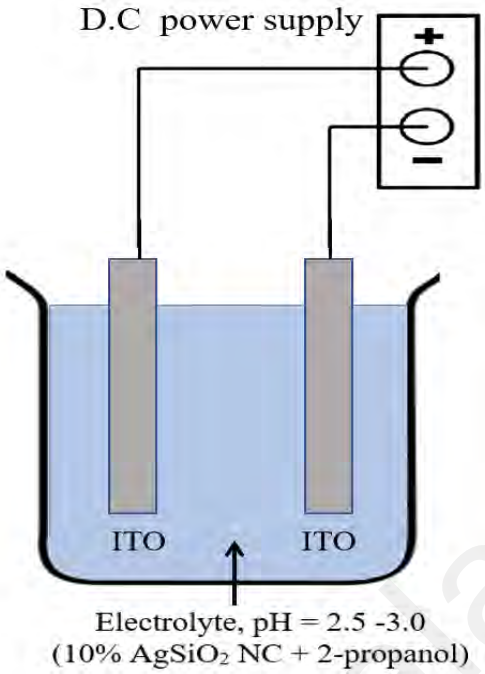

Figure 3.18: Schematic diagram of electrodeposition process for synthesizing Ag-SiO_2 NC thin film on ITO glass substrate

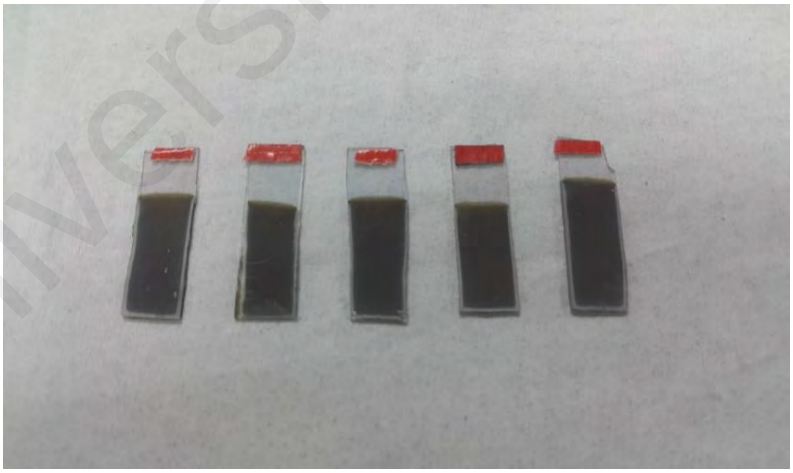

Figure 3.19: ITO glass substrate with Ag-SiO_2 NC deposition

3.9 Characterization Techniques

Various techniques were used for the samples characterizations. Transmission Electron Microscope (TEM) were used to study the morphology of the metal nanoparticles and nanocomposite. The optical study of the nanocomposite has been investigated using UV-Vis and Photoluminescence (PL) , The crystalline structure of the Ag-SiO_2 NC thin films has been investigated using XRD. FTIR and Raman Spectroscopy was used to study the structural properties of the deposited thin film. The dielectric properties of the thin film was measured using Ellipsometer Spectroscopy (ES). The photocatalytic properties were studied using Electrochemical Impedance Spectroscopy (EIS).

3.9.1 Field Emission Scanning Electron Microscopy (FESEM)

The Field Emission Scanning Electron Microscope (FESEM) is used to observe very fine features of the surfaces and capturing high quality of images at a lower voltage. In this research, FESEM (JSM 5410LV, JEOL, Japan) as shown in Figure 3.20 is used to observe the size, shape and distribution of AgNPs. Generally, as shown in Figure 3.21, FESEM consist of two main component which is Field Emmision and Scanning electron Microsope. The first component is where the excited electron (known as primary electron) is produced from a metal surface with the presence of a very high electric field. The primary electron beam is then accelerated by the field gradient and passes through electromagnetic lenses and focusing onto the target specimen. From this bombardment, high energy electrons (known secondary electron) were then emitted from the sample through elastic and inelastic scattering together with the electromagnetic radiation each of which will be detected by the detectors. The produced image of the sample is created by the combination of various intensity of secondary electron.

Figure 3.20: Picture of FESEM machine

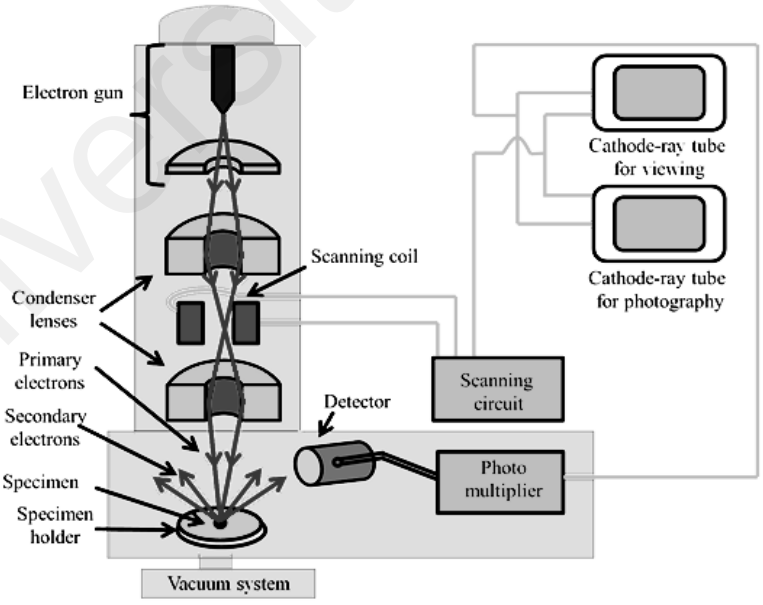

Figure 3.21: Schematic diagram of FESEM (http://www.clipartpanda.com/clipart_images/scanning-electron-microscope-41803737 (25/4/2018).

3.9.2 Transmission Electron Microscopy (TEM)

Further morphology studies on AgNPs and Ag-SiO_2 NC at various filling fraction were performed using Transmission Electron Microscopy (TEM)(LEO LIBRA, Germany) (Figure 3.22), operating at 120kV. There are four main components in a TEM: an electron optical column which consist of electron gun, a vacuum system, a series of lens for focusing and deflecting the beam together with the high voltage generator for the electron source, and control software as in Figure 3.23. Compared to other microscope, the TEM system will project the electron beam pass through the specimen. Hence, the quality of the desired image is determined by the thickness of the sample. Ultra-thin sample should be prepared before the TEM analysis. In this work, AgNPs and Ag-SiO_2 NC samples were dispersed in deionized water and sonicated for 60 minutes to prevent particle agglomeration. From each samples, a small drop of suspension was placed on a copper grid. A few second after the sample particles suspended at the copper grid. Nucleopore polycarbonate filters were used to tape the grid. This is to remove any excessive material from the grids. The grids were then left to dry at room temperature for 3-4 days before sent for TEM analysis. In the TEM, the images is then magnified by the projection lenses system and was then captured in the image recording system for morphological studies.

Figure 3.22: Picture of Transmission electron microscope

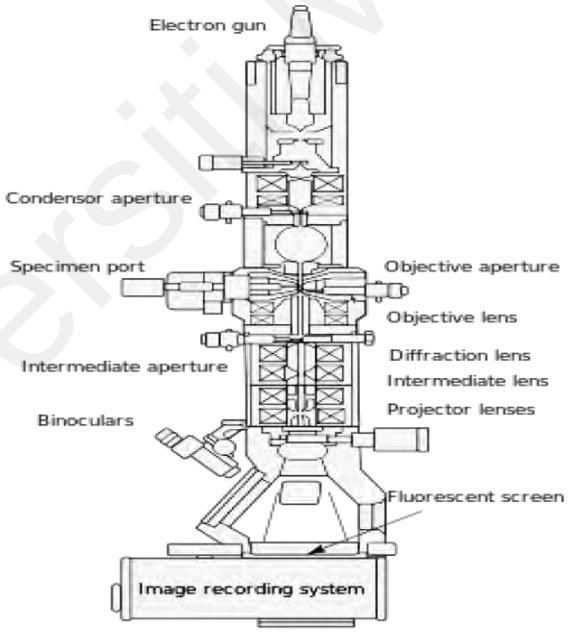

Figure 3.23: Schematic diagram of TEM

(Source: http://en.wikipedia.org/wiki/Transmission_electron_microscopy*)*

3.9.3 Ultraviolet Visible (UV-Vis) Spectroscopy

The optical properties of AgNPs and Ag-SiO_2 NC were studied using Ultraviolet Visible spectrophotometer single beam (Biocary 50 Varian, US), as shown in Figure 3.24. Essentially, the Ultraviolet Visible spectrophotometer analysis is based on the comparison between the light intensity passing through the sample (I) to the light intensity passing it without the sample (I_0)(T.Owen *et al.*, 1996). The result of analysis usually expressed as a percentage of (%T) and the absorbance is refer as A which is written as:

$$A = - \log (\%T/100\%) \quad (3.10)$$

All the samples used in this analysis are diluted in deionized water. The samples are typically placed in a transparent rectangular-shape cell known as cuvette with the width size of 1 cm. The cell was placed into the chamber and exposed to UV, visible and near infrared radiation as in Figure 3.25. The absorption spectra were analyze within the wavelength range between 190 – 800 nm.

Figure 3.24: Picture of UV-Visible spectrophotometer (Biocary 50 Varian)

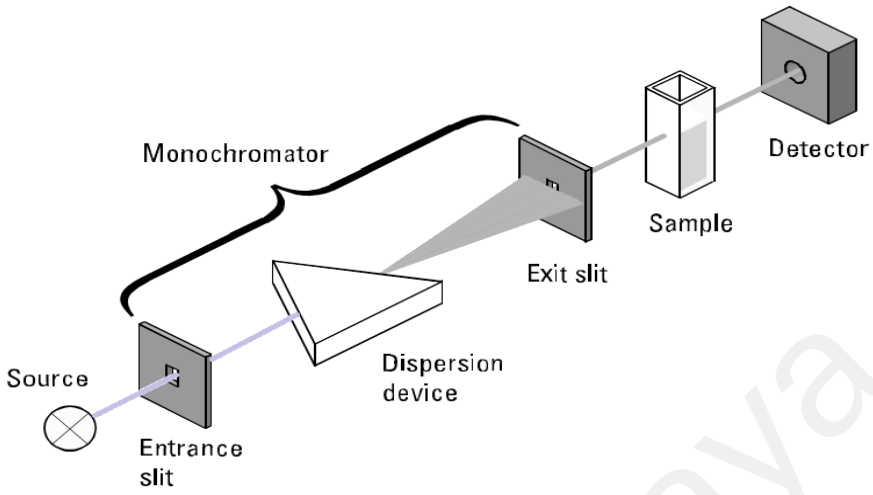

Figure 3.25: The schematic diagram of Ultraviolet Visible (UV-Vis) spectrophotometer (www. Fadhl.alakwa.weebly.com 5/11/2019)

3.9.4 Photoluminescence Spectroscopy (PL)

The spectrometer LS55 series (Perkin Elmer, US) is used to obtain the photoluminescence spectra of Ag-SiO_2 NC samples as shown in Figure 3.26. The machine is used because it covers a large range of excitation and emission energies. A Xenon lamp discharge is used as a light source because it produces a continuum of light from the ultraviolet to the near-infrared for sample excitation. The emission were recorded within the wavelength range of between 200 to 800 nm. Within the excitation part, a pivoted grating combined with two concave mirrors serves as a monochromator. The desired excitation wavelength is selected from the incoming polychromatic radiation produced by the Xenon lamp. Finally, the emission is then captured by the detector as shown in Figure 3.27.

Figure 3.26: Picture of Photoluminescence machine

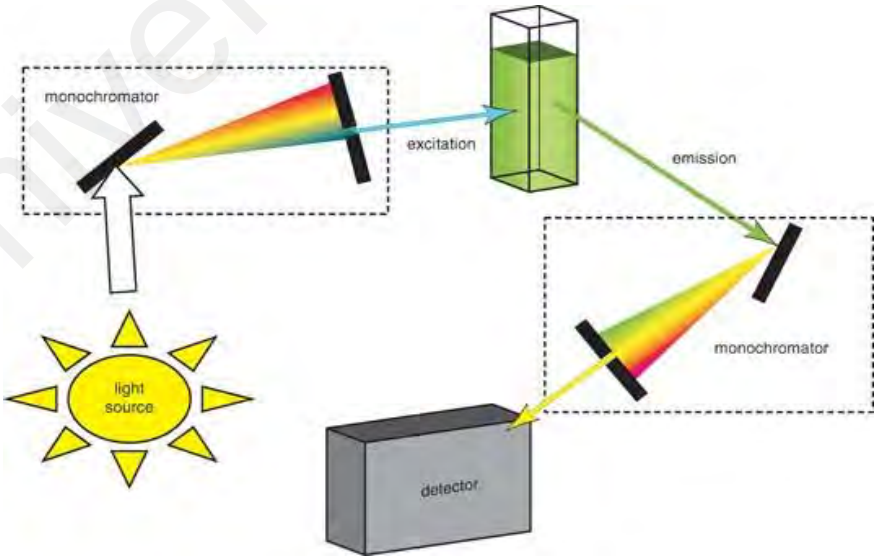

Figure 3.27 : Schematic diagram Photoluminescence.

3.9.5 Fourier Transform Infrared Spectroscopy (FTIR)

Fourier Transform Infrared Spectroscopy (FTIR) is a characterization technique used to study the chemical bonds and interaction between the atoms within the studied nanomaterial. FTIR spectra is used to identify the molecular structure of the nanomaterial. In this research, FTIR (Perkin Elmer, US) was used to ascertain the presence of AgNPs in the Ag-SiO_2 NC nanostructure as shown in Figure 3.28. In this measurement, the sample are made into powder form and placed in the sample holder of the spectrophotometer and IR radiation is let to passed through the samples within wave region between 500 cm^{-1} to 4000 cm^{-1}. As shown in the schematic diagram in Figure 3.29, part of the radiation is absorbed and part of it will passed through (transmitted) the samples. The resultant spectra will shows series of peaks representing the molecular absorption and transmission, which creates the signature pattern or fingerprint of the sample. This pattern provide the detailed information of the sample's molecular structure.

Figure 3.28: Picture of FTIR Spectrometer

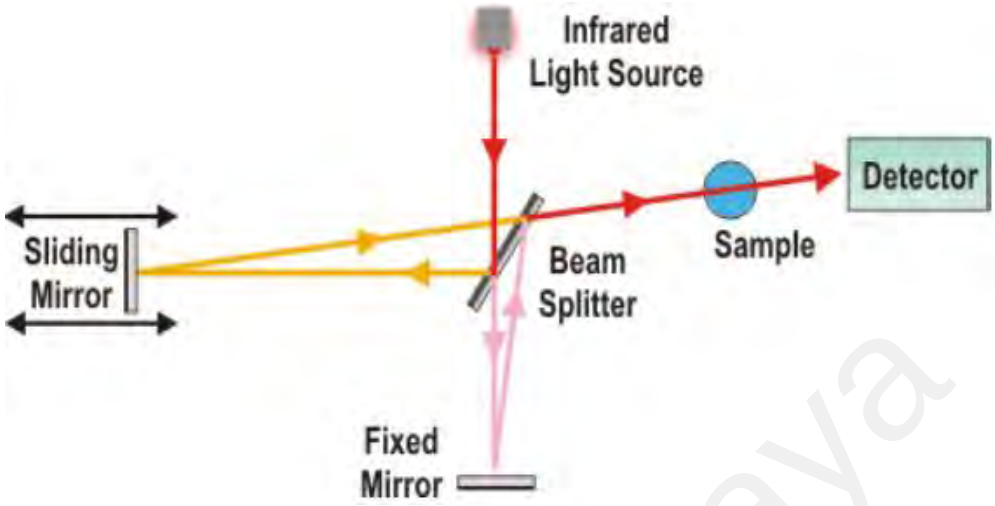

Figure 3.29: Schematic diagram of FTIR

3.9.6 Zeta Potential Analysis (ZP)

Zeta potential (ZP) analysis is a characterization technique used to estimate the surface charge of nanoparticle suspensions in order to understand the physical stability of the particles. In this technique, the charged particles dispersed in dionized water are placed into a zeta cell and upon application of an external electric field, the particles will travel toward the respective electrode which opposite to the particle charge. Their zeta potential and electrophoretic mobility, is calculated by Zetasizer Nanoseries (Malvem Technique, UK). In this measurement, Zeta potential measurements were then carried out on the suspension solutions containing AgNPs and Ag-SiO_2 NC in separate zeta cell using Zetasizer from Malvern Instrutment Ltd as shown in Figure 3.30.

Figure 3.30: Picture of Zeta Potential Machine (Malvern Instrument)

3.9.7 Thermogravimetric Analysis (TGA)

Thermogravimetric Analysis (TGA) is one of the widely used technique for thermal analysis. The TGA system as in Figure 3.31 provide thermogravimetric information in a shape of curve. The samples in this work are tested for their thermal stability. The stability test of all sample were conducted using TGA instrument (SDTA 851 Mettler Toledo, Switzerland). In this technique, the system analyses the changes in the amount and weight for the samples as a function of time or temperature in isothermal state in an enclosed system. The system consist of thermobalance, electronic microbalance with a furnace, temperature programmer and computer unit for control and display data as shown in Figure 3.32.

All samples is made into powder, put in the sample holder, and heated. The powder form is to ensure the maximum surface area to be heated. In this test, N_2 is used as the purge gas and injected into the atmosphere where the heating process is carried out using sample weights of 5-10 mg over a temperature range of 20-1000 ºC with the scan rate of 10 °C/min. The changes in the amount and weight of the sample are simultaneously measured during the heating and cooling process in a controlled manner where the mass, time and temperature data are captured and presented in a shape of curve for further analysis.

Figure 3.31: Picture of Transgravimetric Analysis machine

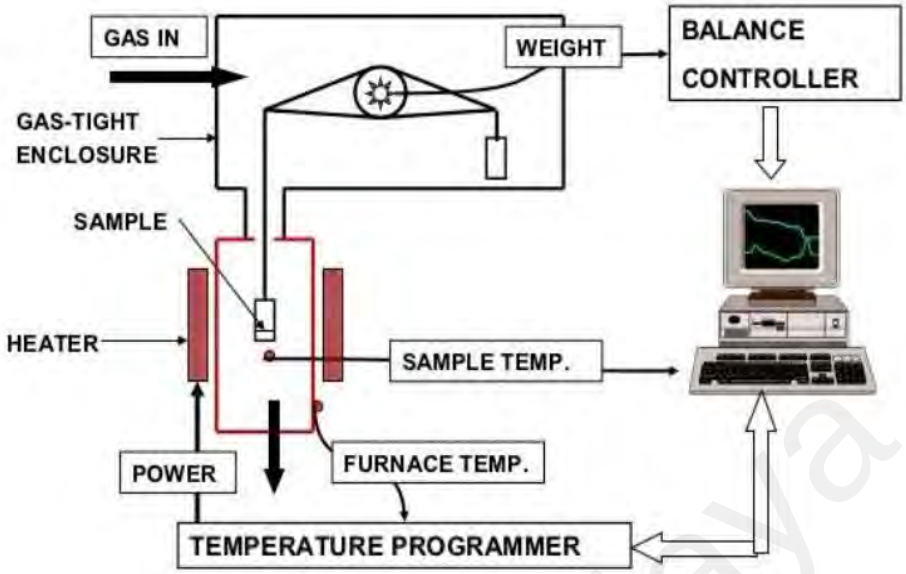

Figure 3.32: Schematic diagram of TGA machine

3.9.8 Differential Scanning Calorimetry(DSC)

Differential Scanning Calorimetry is another thermal analysis technique used to measure heat change, either exothermic or endothermic reaction of the materials as a function of temperature. The DSC instrument (Mettler Toledo DSC 820, Switzerland) shown in Figure 3.33 is used in this research to analyze the fusion and crystallization of the samples. Figure 3.34 shows the schematic diagram of the DSC technique. There are two heating pan (heaters) in the main heating chamber, one is for reference pan and the other one is sample pan. Empty aluminium crucible is put on the reference pan. The sample (about 10 mg) were sealed in the aluminium pans. The analysis were carried out under the Nitrogen flow at the heating rate of 20 ºC/min within the temperature range of –100 to 100 ºC. The heat energy is measured during the heating and cooling process. The curves obtained were then used to analyzed the fusion and crystallization heat of the samples.

Figure 3.33: Picture of Differential scanning calorimetry (DSC)

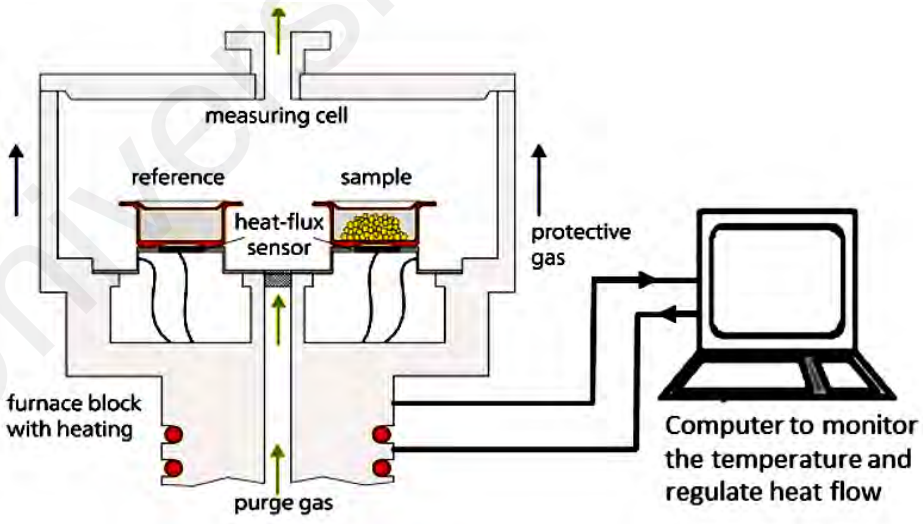

Figure 3.34: Schematic diagram DSC machine

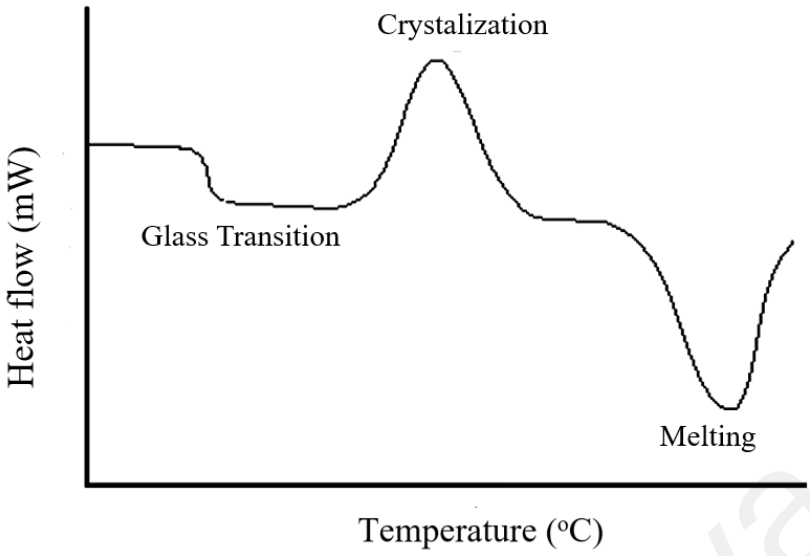

Figure 3.35: Typical graph of DSC

Figure 3.35 shows the typical DSC graph at where glass transition temperature, crystallization temperature and melting temperature can be determined. Endothermic or exothermic reaction can also be analysed using this DSC graph.

3.9.9 X-Ray Diffraction (XRD)

X-Ray Diffraction or XRD is a non-destructive technique which used to analyze the crystallographic structure of materials. This technique utilizes the small wave length to penetrate through the planes in the crystal solids and therefore enable in providing detailed information of the crystal structure such as the orientation, thickness, interplanar spacing of the structure and orientation of the crystals in the solid (Rosenthal *et al.*, 2007). In this research, X-Ray Diffraction unit (Model SIEMEN D500, Germany) operated at 40 kV and 40 mA) as in Figure 3.36 is used to determine the diffraction angle. The results from the X ray diffraction was represented by the value of θ in Scherrer's formula in the equation below:

$$S = \frac{k\lambda}{\beta \cos\theta} \tag{3.11}$$

In the equation, k is the Scherrer's constant of the order of unity for normal crystals, usually having a value of 0.9. The X-ray wavelength is represented by λ. In this research, the value λ was taken as 1.5406 Å. The complete schematic diagram of X-Ray diffraction technique is shown in Figure 3.37.

Figure 3.36: Picture of X-ray diffraction machine

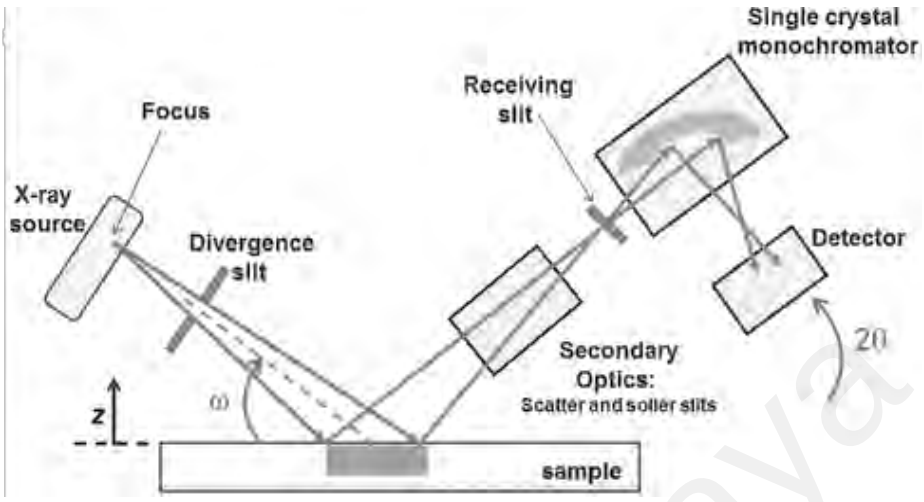

Figure 3.37: Schematic diagram of X-Ray diffraction machine (Sardela Jr, 2014)

3.9.10 Surface enhanced Raman Spectroscopy (SERS)

Surface enhanced Raman Spectroscopy (SERS) is spectroscopic technique used to study the structural fingerprint of materials based on the signature pattern produced by the enhancement of the inelastic scattering of the reemitted photons. In this research, the technique is used to analyze the fingerprint pattern of Ag-SiO_2 NC samples. The analysis of the nanostructure is based on the light interaction with the samples which then changes the photon frequency due to inelastic scattering of monochromatic light from a laser source produced by Micro-Raman spectrometer (HORIBA Model: XploRA Plus, France) as in Figure 3.38. In this work, the sample is illuminated with a laser beam as the source of photon in the visible, near-infrared, or near ultra-violet range. The photon of the laser beam is then absorbed by the sample and then reemitted. The photon from the beam interacts with the electrons of the bonds of the molecules on the thin film surface. The frequencies of the reemitted and scattered photons varies and shifted either to a lower (red

shift) or higher (blue shift) values compared to the original frequency, which then is known as Raman effect. The effect of this normal Raman scattering is usually weak and SERS has to be employed to enhanced the signal for analysis. The enhanced spectra or pattern shift in the frequencies from the effect provides detailed information about the rotational, vibrational and other frequencies transitions of molecules or atoms in the samples. The computer is connected to the CCD (as shown in Figure 3.39) to convert the transitions mode into spectrum using specific software.

Figure 3.38: Picture of Raman machine.

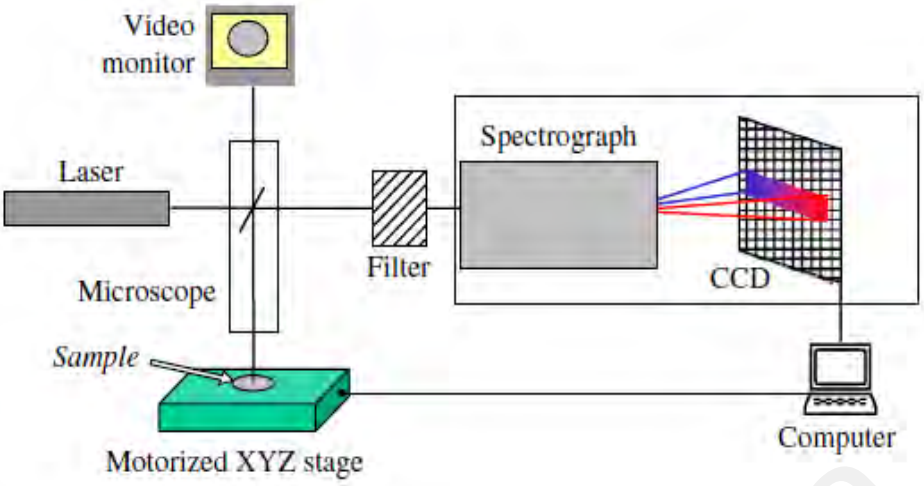

Figure 3.39: Schematic Raman Spectroscopy technique (Gouadec, Ph. Colomban / Progress in Crystal Growth and Characterization of Materials 53 (2007) 1-56)

3.9.11 Ellipsometer Spectroscopy (ES)

Spectroscopic Ellipsometry (SE) is another non-destructive optical technique which measures the change in the polarization state upon a polarized light reflected obliquely from a thin film surface. The analysis of the optical properties of a thin film is based on the measurement of two independent ellipsometry parameters, amplitude ratio (Ψ) and phase change (Δ). Ellipsometry is a model based analysis which also used to determine the thin film interface, thickness, as well as optical properties. In this research, Spectroscopic ellipsometry (SE) (HORIBA, Model : MM16 System, France) as in Figure 3.40 was used to determine the thickness of the sample thin film, the optical constants such as the refractive index, extinction coefficient and permittivity values. The SE light source is a combination of a tungsten-halogen lamp and a blue LED provides stable illumination across the visible range of 430-850 nm. The input and output heads are identical and comprises of a Glan-Taylor polarizer, two ferroelectric liquid crystal cells

and a fixed retardation plate. The light is analyzed by a spectrograph with a CCD detector and is able to deliver the complete 16-element Mueller matrix in 2 seconds with high accuracy and precision. Figure 3.41 shows the set up of the SE technique.

Figure 3:40: Picture of Ellipsometer machine.

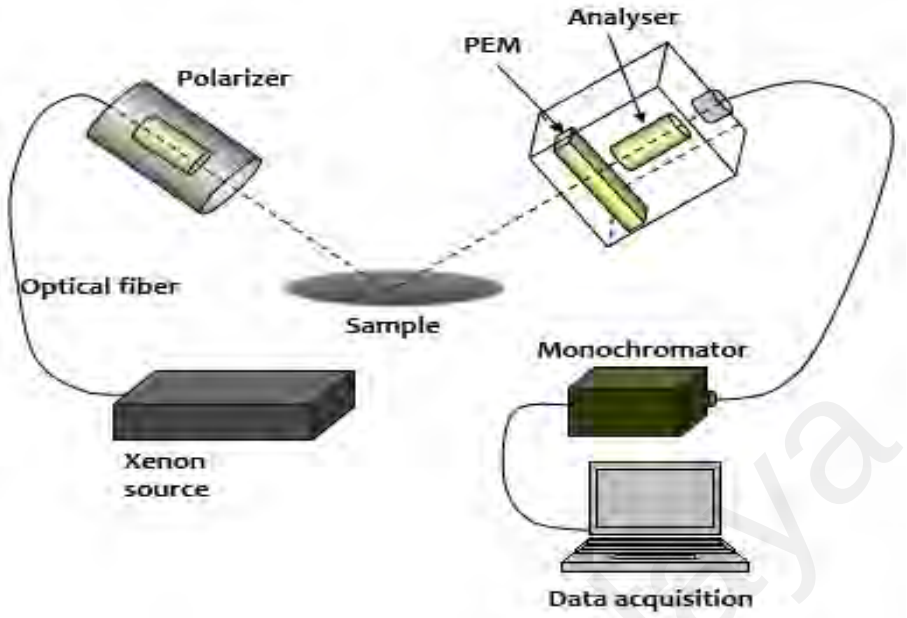

Figure 3.41: Schematic diagram of an ellipsomentry technique

3.9.12 Electrochemical Impedance Spectroscopy (EIS)

Electrochemical Impedance Spectroscopy (EIS) is a technique implemented to study the electrical properties of dielectric and semi-conductive materials. EIS results presents the information about the conducting materials by measuring current as function of applied potential (E). In this research, the photo-electrochemical studies of the samples were carried out with potentiostat/galvanostat instrument (Metrohm, Model; Autolab PGSTAT302N, US) as in Figure 3.44. In Figure 3.42, an experiment setup with a conventional three-electrode with Ag SiO_2 /ITO modified electrodes were used as the working electrode (WE) and a platinum wire were used as counter electrode while Ag/AgCl (KCl) as reference electrode. For the photochemical studies, the fabricated thin film electrode was inserted into a cell containing 0.5M Sodium Hydroxide (NaOH) aqueous solution exposed to the dark and the illumination condition generated using

xenon arc lamp 150W (Newport, Model 69907) with AM 1.5G filter as shown in Figure 3.43. The light intensity was calibrated to 100 mW/cm^2 and the scan rate was 25 mV/s and the scan range ranging from -0.5 to 0.5V vs SCE.

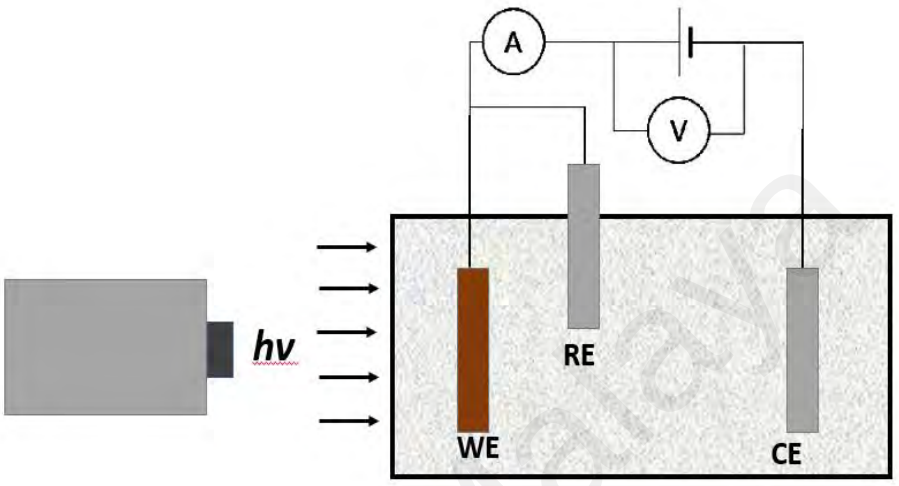

Figure 3.42: Schematic diagram of three-electrode PEC water splitting cell, where WE ; working electrode, CE ; Counter electrode and RE is the reference electrode.

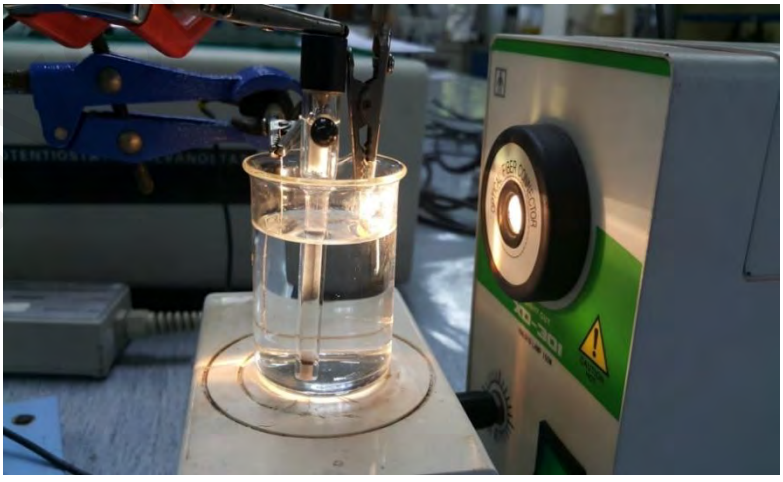

Figure 3.43: The illumination condition generated using xenon arc lamp 150W

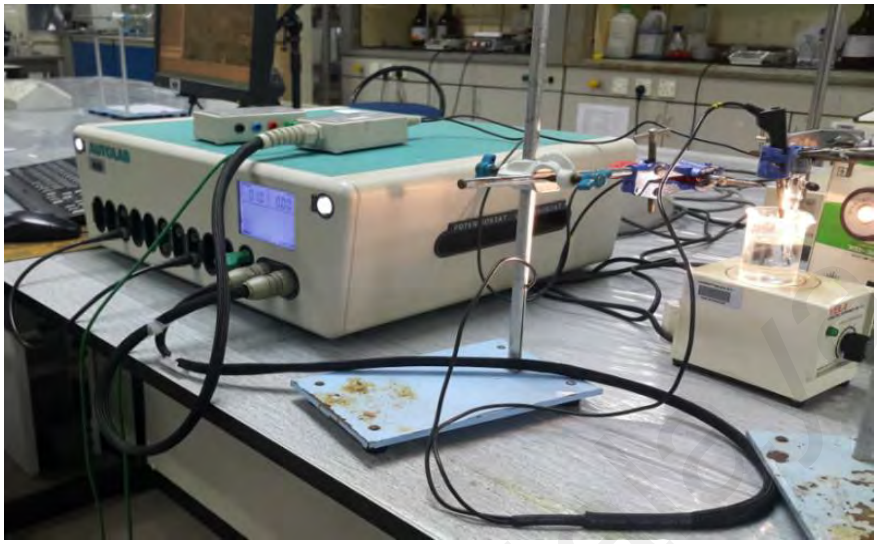

Figure 3.44: Picture of Potentiostat/Galvanostat (Model: Autolab PGSTAT302N)

CHAPTER FOUR:

OPTICAL, MORPHOLOGICAL AND PERMITTIVITY STUDIES

4.1 Introduction

This chapter presents the analysis and results of the morphology, optical and permittivity studies of Silver Silica Nanocomposite (Ag-SiO_2 NC) at various filling fractions with constant concentration. The samples ID with different volume ratios of AgNPs to SiO_2 i.e Ag:SiO_2 are ; [20%, sample ID Ag20], [40%, sample ID Ag40], [60%, sample ID Ag60], [80%, sample ID Ag80] and [100%, sample ID Ag100] were used to investigated the effect of AgNPs inclusions on the nanocomposite. The UV-Vis spectra were obtained where the indirect band gap of amorphous structure of silica could be studied. The images from TEM are shown for the morphology analysis. The values of dielectric contant (ε_r), dielectric loss (ε_i), refractive index (n) and extinction coefficient (k) were obtained from Spectroscopy Ellipsometry (SE).

4.2 Optical Studies

4.2.1 Ultraviolet Visible Spectroscopy Studies

The optical spectra of AgNPs and Ag-SiO_2 NC were investigated using UV-Vis spectrophotometer. The optical absorbance spectra of AgNPs and Ag-SiO_2 NC at various volume ratios were measured at room temperature.

4.2.1.1 Absorption Spectroscopy of AgNPs

The absorption band for AgNPs in Figure 4.1 shows a clear and sharp peak at 423 nm due to the narrow size distribution of the nanoparticles which indicate that the AgNPs are present in the crystalline state. The AgNPs are spherical, discrete and homogeneously dispersed with a mean diameter size of 33 nm. This shows that the aggregation process occurs at a slow rate with the releasing of the free energy during the nucleation process via particle surfaces and as a result reduces the activation energy barrier during nucleation (Pal *et al.*, 2006 ; Liz-Marzan *et al.*, 1996).

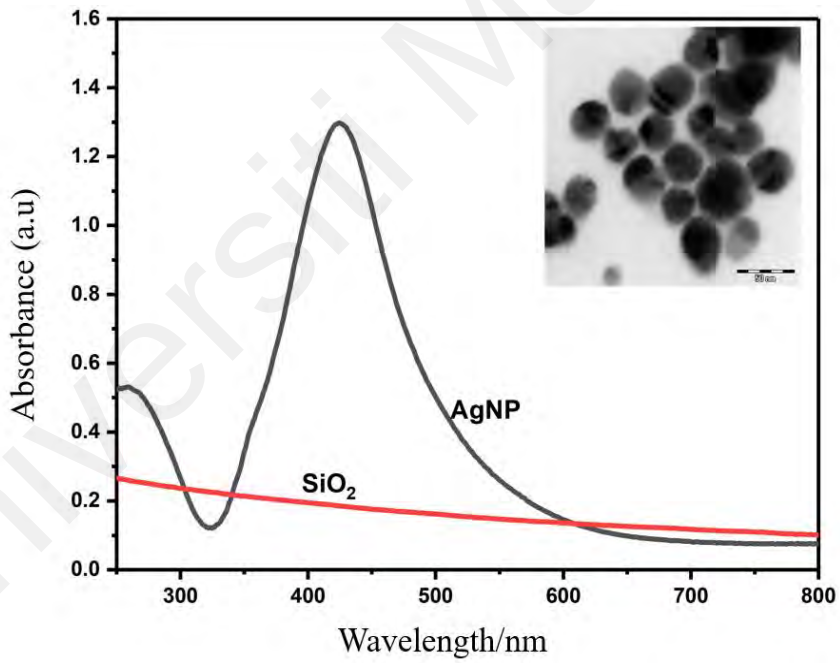

Figure 4.1: The SPR spectra of AgNPs with a symmetrical peak at 423 nm which indicates a narrow particle size distribution in the inset picture.

4.2.1.2 Absorption Spectroscopy of Ag-SiO_2 NC at Various Filling Fraction

The UV-Vis absorption spectra of all samples in Figure 4.2 show the effect of various degree of filling fractions of AgNPs incorporated into the nanostructure. The sample with ID Ag20 shows a red shift at 456 nm wavelength followed by other filling fractions ; Ag40, Ag60, Ag80 and Ag100 at 455 nm, 453 nm, 447 nm and 435 nm, respectively. The size of full width at half maximum (FWHM) for all samples Ag20, Ag40, Ag60, Ag80 and Ag100 are measured as 122 nm, 136 nm, 112 nm 97 nm and 114 nm, respectively. It is obvious that the absorption peak belong to all filling fraction show an increase in the FWHM and are red shifted compared to AgNPs particles.

The absorption spectra of UV corresponds to the excitations of outer orbital of the electron. As the UV radiation passes through the samples, the affected atoms or molecules in the samples absorb energy while it rotates and vibrate with respect to each other. This energy is then used to initiate an electron from the ground level to an excited level. The discrete energy levels packed at each electronic level contributes to the absorbance spectra. It is reported from previous work that the SPR absorption is not just sensitive to the properties of particles size and shape, but also to the surrounding medium. The blue shift of small particles will be observed if the AgNPs dominated the configuration of the dielectric.

As in this work, the surrounding nanostructures were dominant and a red shift is observed with the increase in the size of FWHM. The shift is also due to the local increase of refractive index and scattering from the larger SiO_2 nanoparticles (Liz-Marzan *et al.*, 1996). According to Mie's scattering theory, the dipole absorption due to electric field

oriented along the interparticle axis within the nanostructure specified plane contributes to a significant red shift of the absorption peak (Xu *et al.*, 2006). For this reason, in the UV-Vis measurement, the mean 23 nm red shift as seen after the encapsulation of AgNPs into Silica is in good agreement with the TEM images.

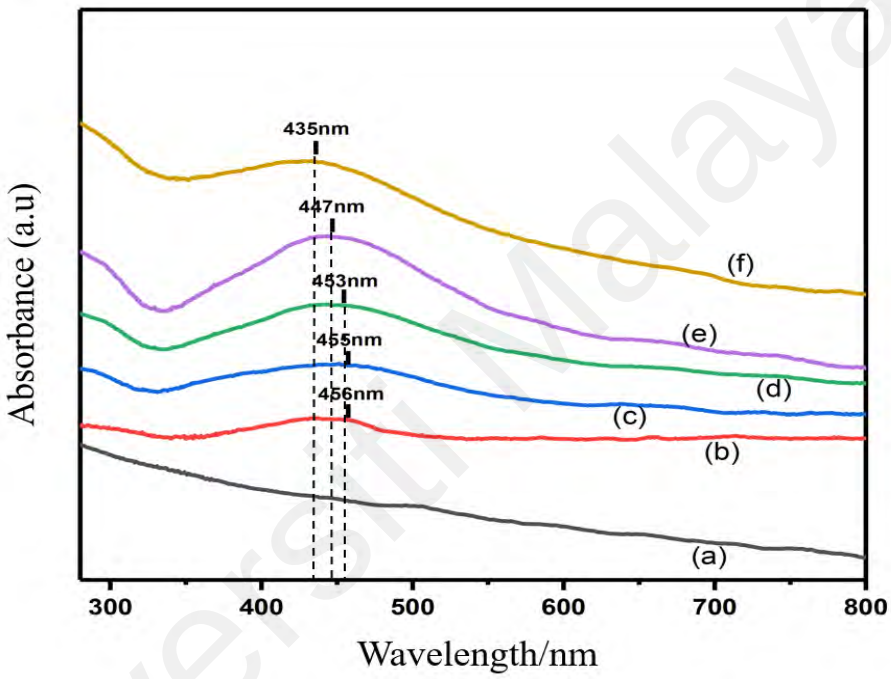

Figure 4.2: UV-Vis absorption spectra of Ag-SiO_2 NC at the various filling fraction (a) pure SiO_2 (b) Ag20 (c) Ag40 (d) Ag60 (e) Ag80 and (f) Ag100.

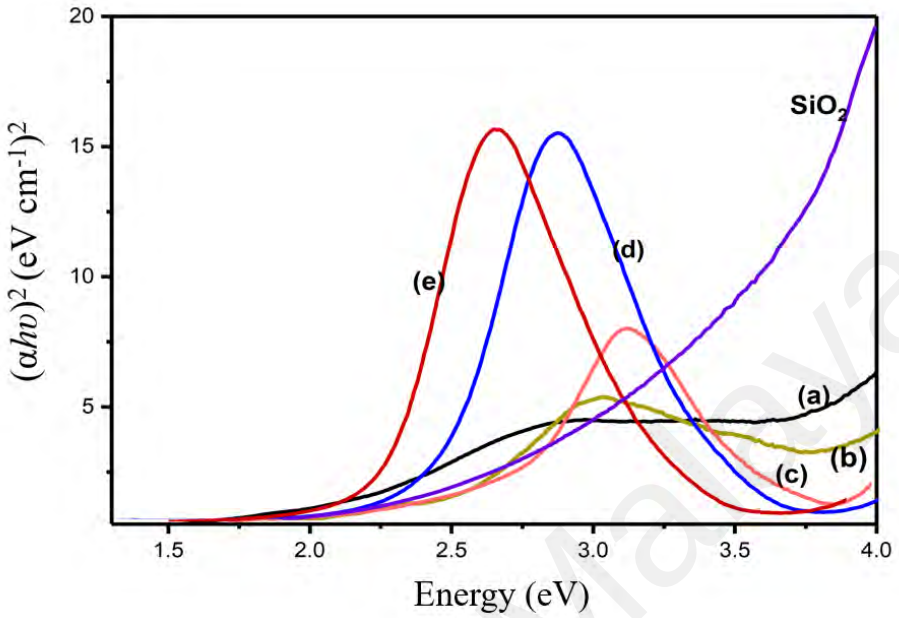

Figure 4.3: $(\alpha h\upsilon)^2$ vs. $h\upsilon$ (direct bandgap) plots of pure SiO_2 and Ag-SiO_2 NC at various filling fractions of Ag/SiO_2 (a) Ag20 (b) Ag40 (c) Ag60 (d) Ag80 (e) Ag100

The general equation of Tauc plot method is given as

$$(\alpha h\upsilon)^n = K\,(h\upsilon - E_g) \qquad (4.1)$$

Where $h\upsilon$ is the incident photon energy, E_g is the direct band gap energy, α represents the absorption coefficient, K is the energy independent constant, and n is the nature of transition. To determine the nature and width of the band gaps, $(\alpha h\upsilon)^2$ was plotted versus incident photon energy ($h\upsilon$) as shown in Figure 4.3.

The linear part as shown in the plot $(\alpha h\upsilon)^2$ versus $(h\upsilon)$ shows that the samples has a direct energy band gap. This direct band gap values and the allowed direct transition energies were determined by the intercept on the x-axis which represents the energy by extrapolating the linear portion of the curves to zero absorption value which gives the value as shown in Figure 4.4. These values are summarized in Table 4.1.

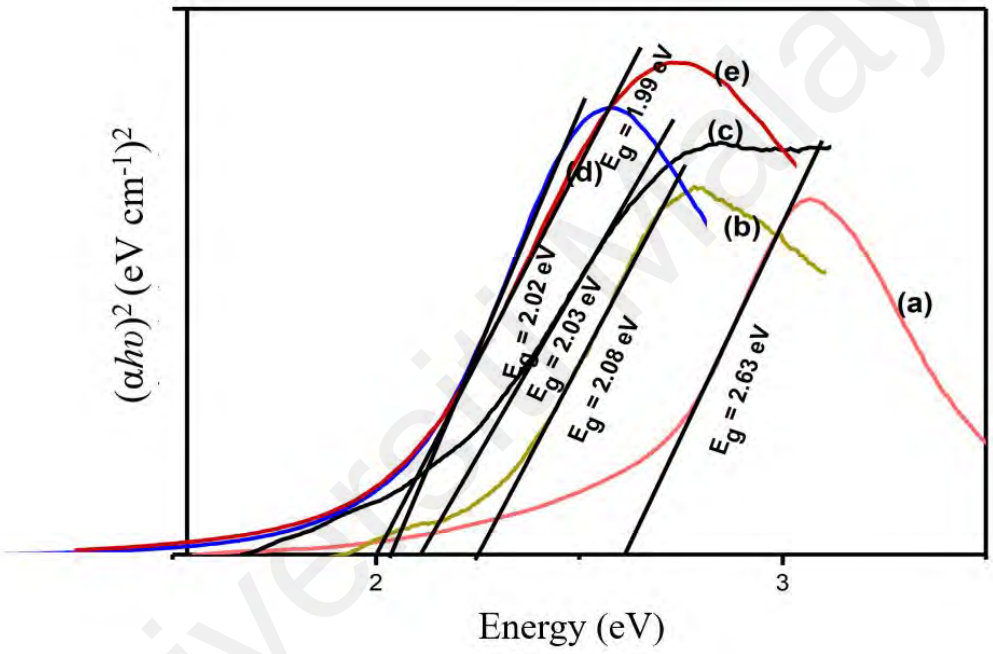

Figure 4.4: $(\alpha h\upsilon)^2$ vs. $h\upsilon$ (direct bandgap) plots of (a) Ag20 (b) Ag40 (c) Ag60 (d) Ag80 (e) Ag100.

Table 4.1: Samples with the direct band gap values

Samples	Wavelength (nm)	Band Gap (eV)
Ag20	456	2.63
Ag40	455	2.08
Ag60	453	2.03
Ag80	447	2.02
Ag100	435	1.99

Figure 4.5 is the UV-Vis absorption spectra of the substrate tested in different pH. The substrate in a basic medium (pH 9.4, 10.8 and 12.8) exhibit stronger absorbance peaks while the substrate in acidic medium (pH 3.4 and 4.8) shows lower absorbance, with no absorbance at pH 1.4. The strongest absorption peak is seen at pH 9.4 due the present of more AgNPs since the nucleation and rapid growth of AgNPs is at pH 9.0 (Sekhar et al., 2018). The substrate is more stable in the basic medium compared to the acidic medium. The substrate spectra at all pH are slightly blue-shifted due to the pH effect on the different scattering in the Ag-SiO_2 NC nanostructures. One of the reasons for the stronger signals at higher pH medium is the presence of the strong dipole-dipole interactions of the OH^{-1} and the decrease in the nanoparticle size which are blue-shifted for all samples. This in turn, tunes the nano-gap between the nanoparticles which creates vast SERS hot spots for the electromagnetic enhancement (Chen *et al.*, 2017).

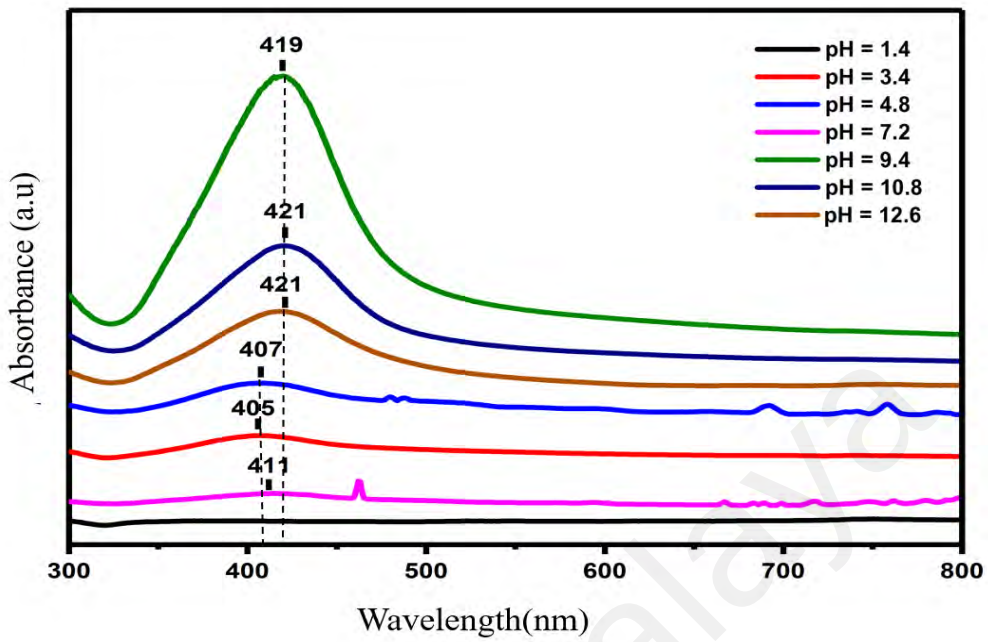

Figure 4.5: Uv-Vis spectra of pH studies of the optimum filling fraction (Ag60).

4.2.2 Photoluminescence Studies

Figure 4.6 shows the PL emission spectra of Ag-SiO_2 NC synthesized via sol gel method. The spectra of all samples exhibit similar PL features, consisting of main emission band between 545-555 nm for pure SiO_2 and 548-562 nm for Ag-SiO_2 NC at various wavelengths, namely 555, 545, 567, 677 and 445 nm for Ag20, Ag40, Ag60 Ag80 and Ag100, respectively. The PL emission spectra are shifted to larger wavelength with an increase in the amount of AgNPs in the samples as shown in Figure 4.6. This red shift is attributed to the increase in the amount of AgNPs.

The PL spectra in Figure 4.6 show various intensities for each sample. The sample of Ag100 displays the highest PL intensity. This is followed by other samples. The increase in the amount AgNPs increases the PL intensity of the respective samples. This shows that the quantum efficiency of Ag-SiO_2 NC is greatly dependant on the amount of added AgNPs.

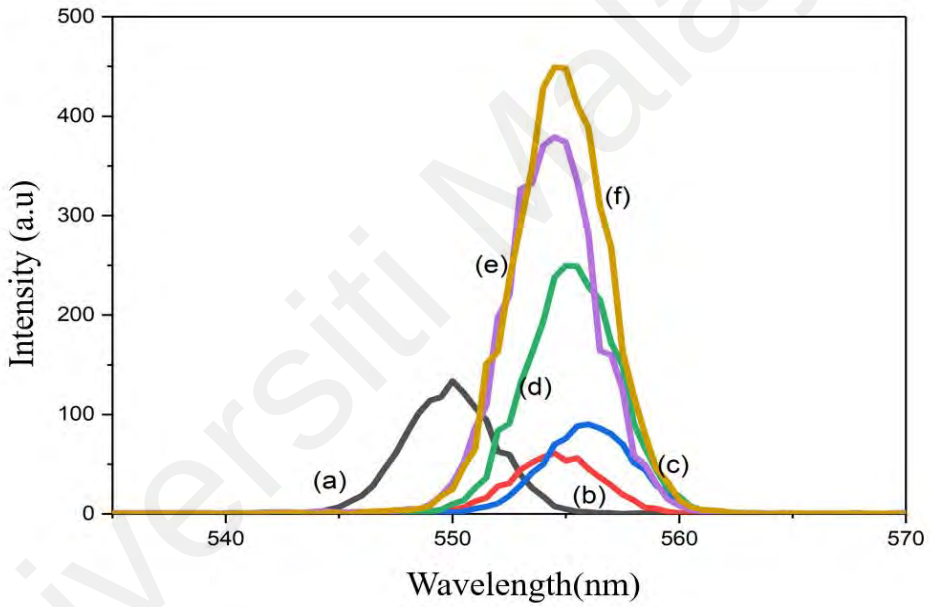

Figure 4.6: Photoluminescence spectra of real permittivity of (a) pure SiO_2 and Ag-SiO_2 NC samples at different filling fraction (b) Ag20 (c) Ag40 (d) Ag60 (e) Ag80 and (f) Ag100.

4.3 Morphology Studies

4.3.1 Morphology of AgNPs

The morphological studies for AgNPs was performed and detailed by Field Emmision Electron Scanning Microscope (FESEM) and Transmisson Electron Microscope (TEM). The image obtained from FESEM and TEM micrograph clearly indicates that the AgNPs are almost spherical in shape and monodisperse with most particles are well distributed having a size range between 25–50 nm. Figure 4.7 and Figure 4.8 represent the images from FESEM while Figure 4.9 and Figure 4.10 are shown at higher resolution of 0.05 nm which is obtained from TEM. It is clear that the shapes of the particles are spherical and well dispersed. The size distributions of the particles are measured and shown in Table 4.2.

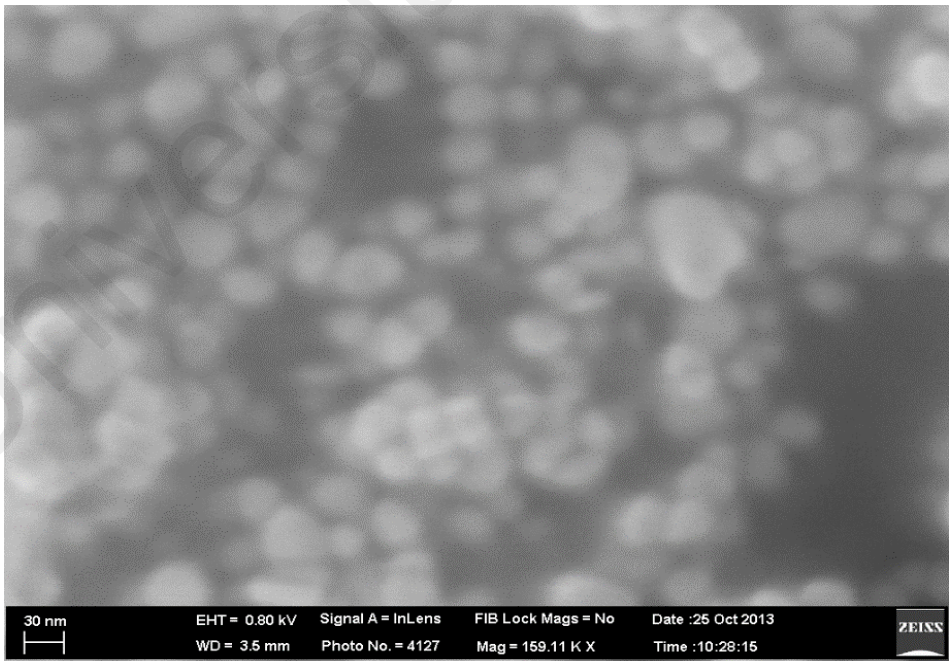

Figure 4.7: High resolution of FESEM images of AgNPs with 159 K times magnification

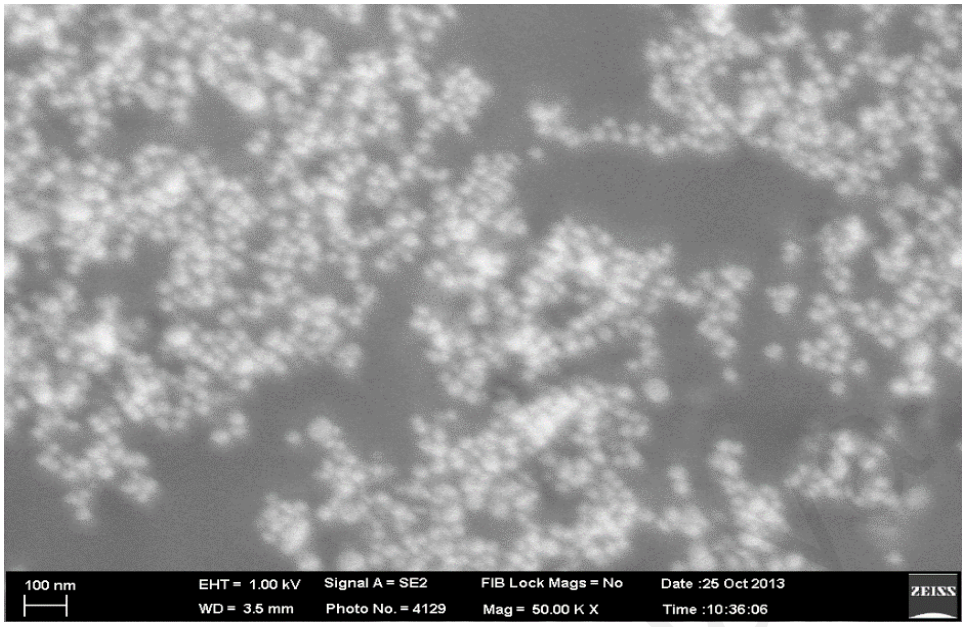

Figure 4.8. High resolution of FESEM images of AgNPs with 50 K times magnification

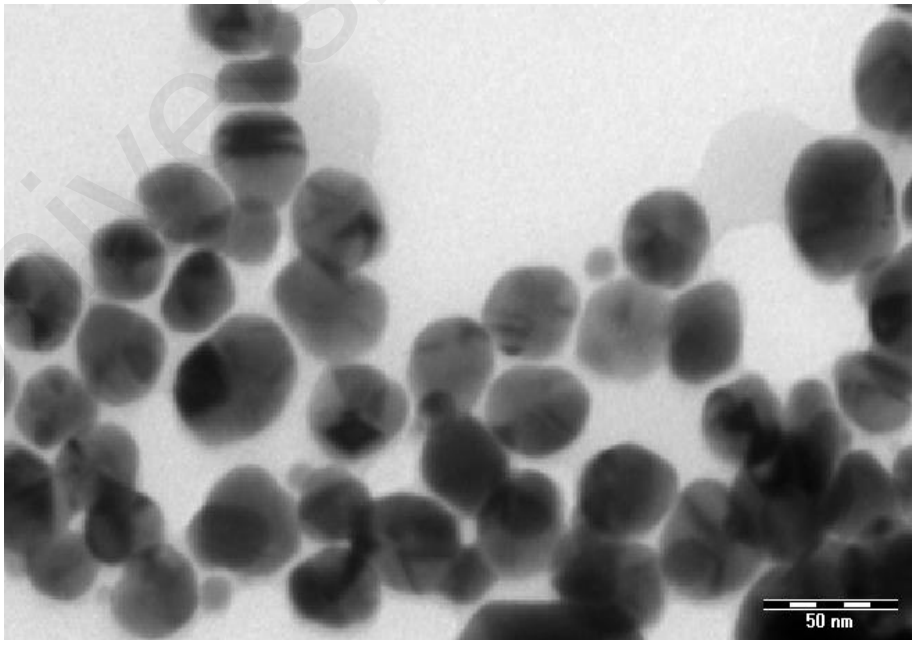

Figure 4.9: High resolution of TEM images of AgNPs with 50 nm range

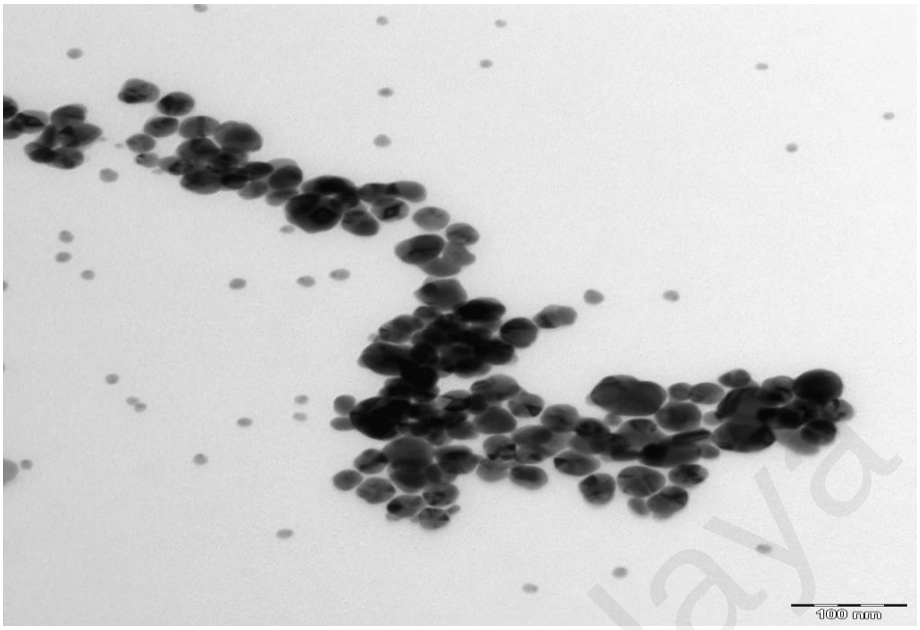

Figure 4.10: TEM images of AgNPs with 100nm range

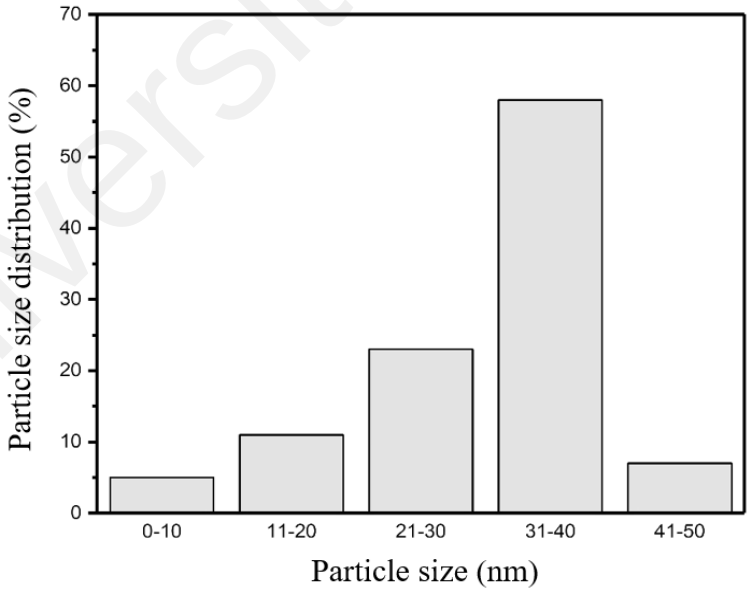

Figure 4.11: Histogram chart of particle size distribution of AgNPs.

Table 4.2: Distribution of AgNPs nanoparticles.

Particle size distribution (%)	Particle size (nm)	Total
5	0-10	4
11	11-20	9
23	21-30	18
58	31-40	46
8	41-50	6

The TEM images indicate that the AgNPs are present in the crystalline state, spherical, discrete and homogeneously dispersed with a mean diameter size of 30 nm. This shows that the aggregation process occurs at a slow rate with the release of free energy during the nucleation process via particle surface, which reduces the activation energy barrier during nucleation (Cai *et al.*, 1998; Pal *et al.*, 2006). The AgNPs are very stable which shows that the activation energy barrier for nucleation has been reduced by the releasing of free energy during the synthesis process. Because of this, the nanoparticle colloidal solution can be used directly for further characterizations and analysis without the separation from the solution (Kim *et al.*, 2001; Zang *et al.*, 2007).

4.3.2 Morphology of Ag-SiO_2NC at Various Filling Fractions

The morphological samples for pure SiO_2 and Ag-SiO_2 NC were examined using Transmission Electron Microscope (TEM). The solid Ag-SiO_2 NC contained a combination of amorphous and crystalline phases of SiO_2, embedded with AgNPs. Figure 4.12 shows the surface for pure SiO_2 system, which was formed after the hydrolysis process with ethanol. The surface appears amorphous and crystalline state with definite boundaries. This combined structures are illustrated in the following Figure 4.13.

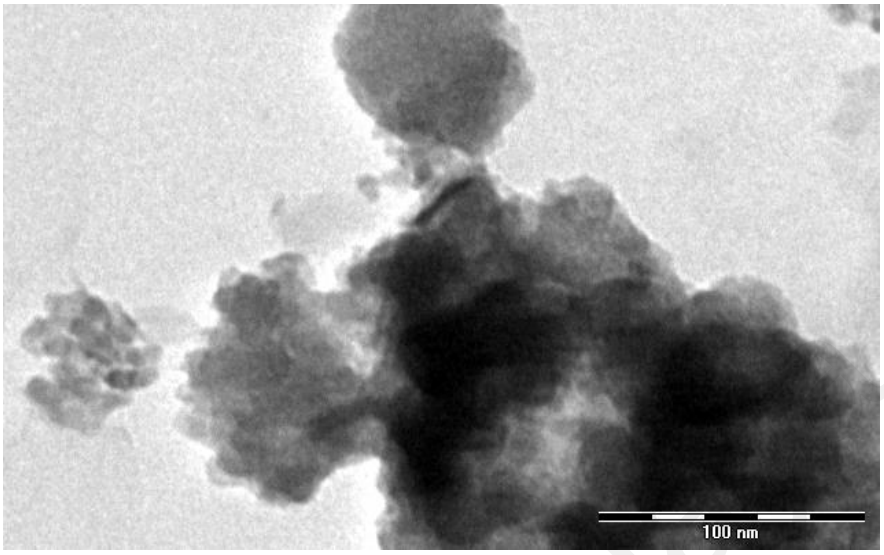

Figure 4.12. TEM image of pure SiO_2.

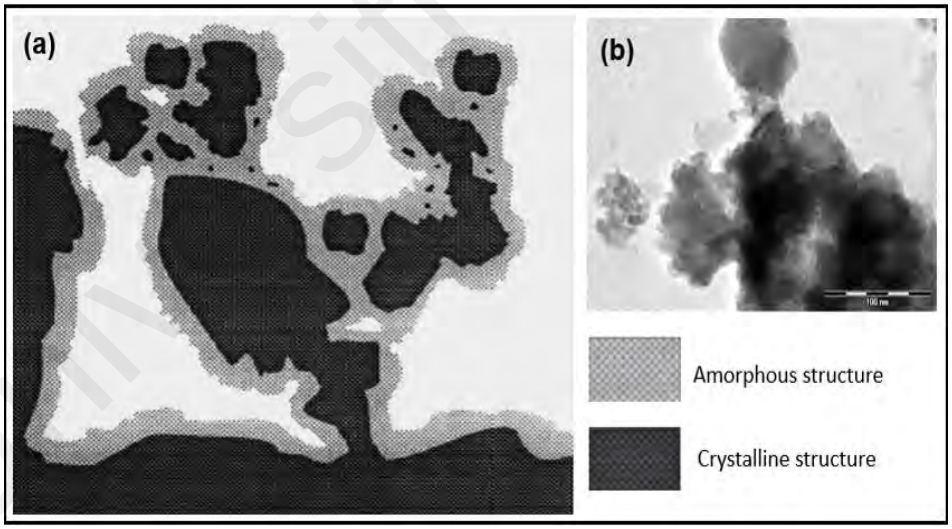

Figure 4.13: (a) Schematic of proposed structure of porous silicon. Porous silicon contains nanoscale wire and nanocrystallite regions, as well as amorphous silicon and oxide (Arun 1996) (b) is the TEM image of SiO_2.

The complex sponge of interconnecting layers of SiO_2 nanostructures in Figure 4.12 is the result from the hydrolysis process. The nanostructures range from atomic silicon up to pieces that can be considered as bulk silicon. The convolution network of the nanostructure as shown in Figure 4.13 gives the optical and electronic properties in different behaviors for the nanocomposite.

The TEM images in Figure 4.14 until Figure 4.18 reveals that the Ag-SiO_2 NC nanostructures shows an apparent transition from discrete AgNPs into a percolation network as the increase in the filling fraction. It can be seen that the AgNPs embedded on the surface of SiO_2 matrix are well separated, spherical and homogeneous. A gradual decrease in the interparticle spacing was observed with the increasing filling fraction.

This suggests the absence of additional aggregation or agglomeration and proves the decrease in the distance between the particles. The AgNPs are seen mono-dispersed and homogeneous. The average size distributions are measured from the enlarged images of TEM which is 4 nm to 5 nm. This average size agrees with a previous work which confirm the size and distributions of AgNPs in the SiO_2 nanostructures (Jasiorski, 2014). As the ratio of Ag/SiO_2 exceeds the optimum filling fraction (Ag60), the inter-particles distance becomes indefinite.

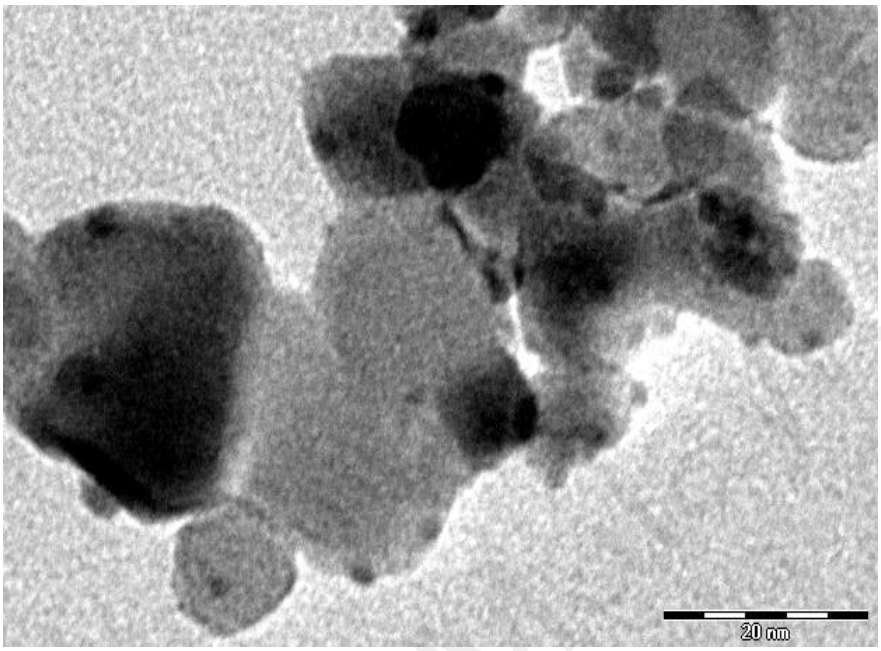

Figure 4.14: TEM images of Ag-SiO_2 NC at a lower filling fraction (0.2)

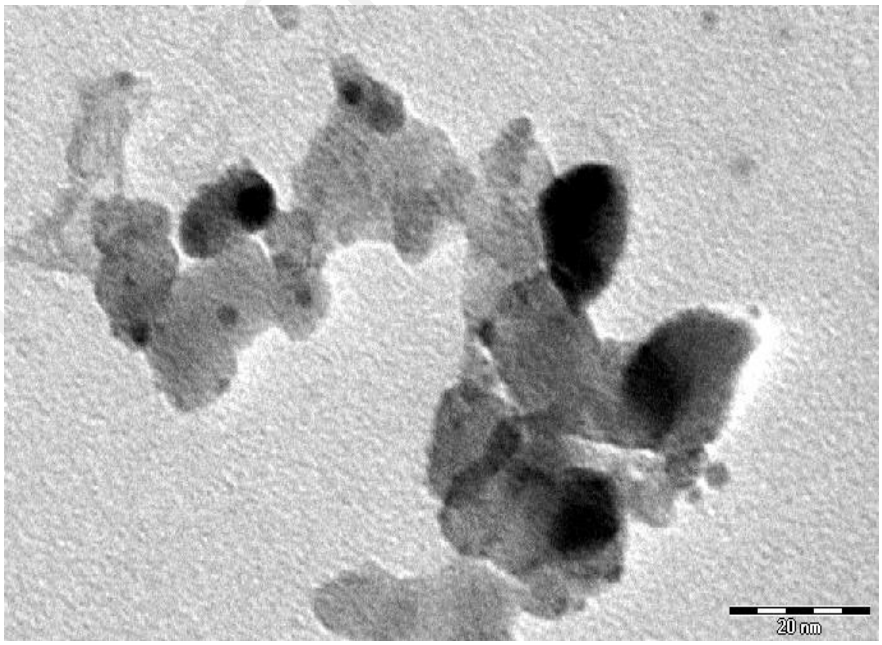

Figure 4.15: TEM images of Ag-SiO_2 NC at a low filling fraction (0.4)

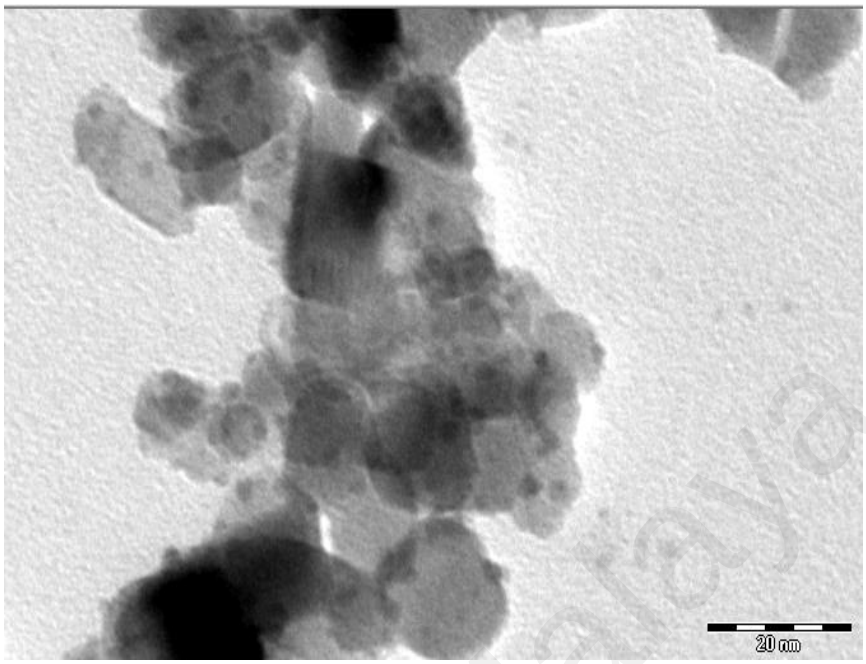

Figure 4.16: TEM images of Ag-SiO_2 NC at optimum filling fraction (0.6)

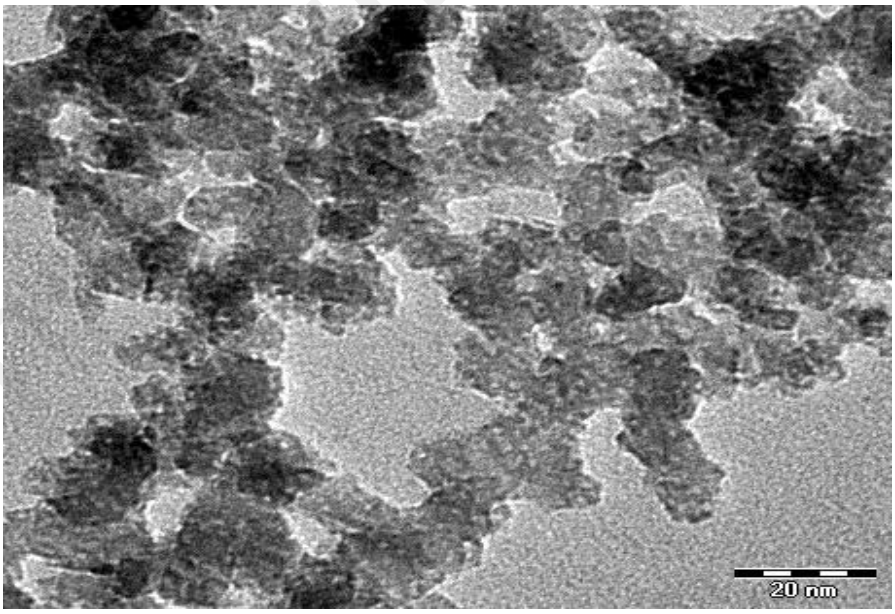

Figure 4.17: TEM images of Ag-SiO_2 NC at higher filling fraction (0.8)

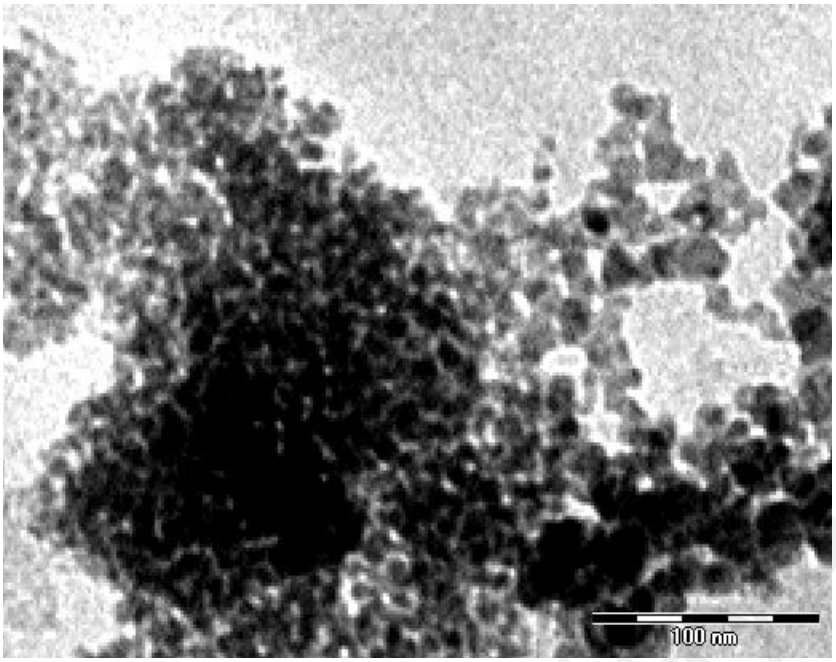

Figure 4.18: TEM images of Ag-SiO_2 NC at highest filling fraction (1.0)

Further analysis on the TEM images for the filling fraction of 4.0 is shown in Figure 4.19 which indicates that the mean size of particles is 5 nm and the mean inter-particle distance of AgNPs is 15 nm which indicates that the AgNPs are well dispersed and isolated. As the filling fraction is increased to 0.6 ratio, apparent reduction in the interparticle distance is observed as shown in Figure 4.20 with the mean size of particles and the average inter-particle distances are 6 nm and 10 nm, respectively. The TEM images in Figure 4.21 shows that the Ag-SiO_2 NC nanostructures of filling fraction 1.0 where the SiO_2 nanostructures are surrounded and packed by AgNPs with inter-particle indefinite spacing (Figure 4.20 (b)) with the mean size of the particles remains the same. The morphological studies supports the peak shift as revealed in the SPR absorption peaks.

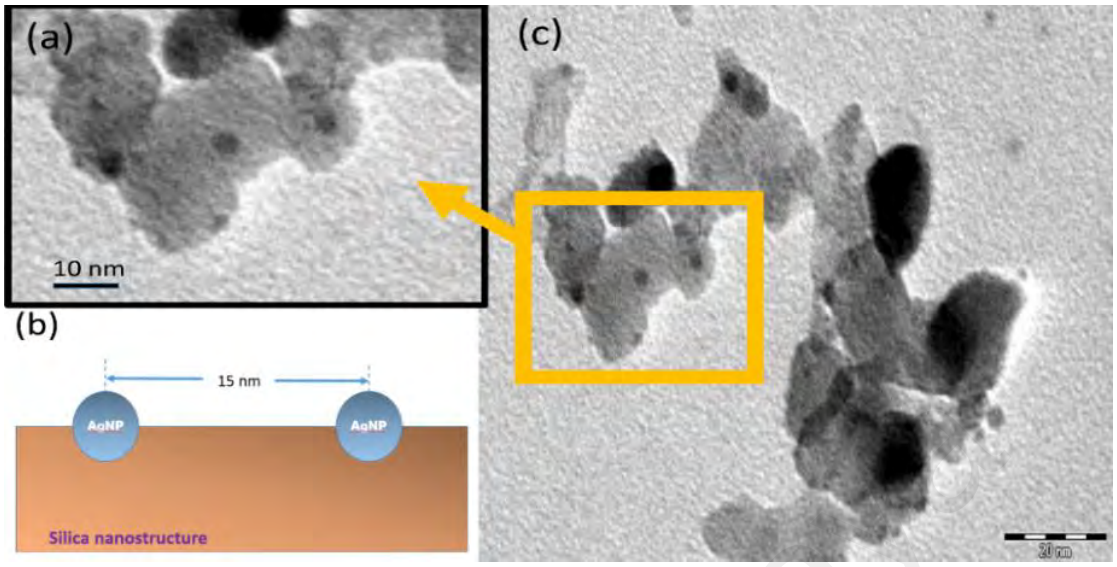

Figure 4.19: Morphological image shows the average inter-particle distance between AgNPs on the surface of SiO_2 nanostructure for filling fraction Ag40 is 15 nm in (b) ($\varepsilon_1 = 2.3$). (a) The small particles with the average size of 5 nm dominated by the surrounding SiO_2 nanostructures.

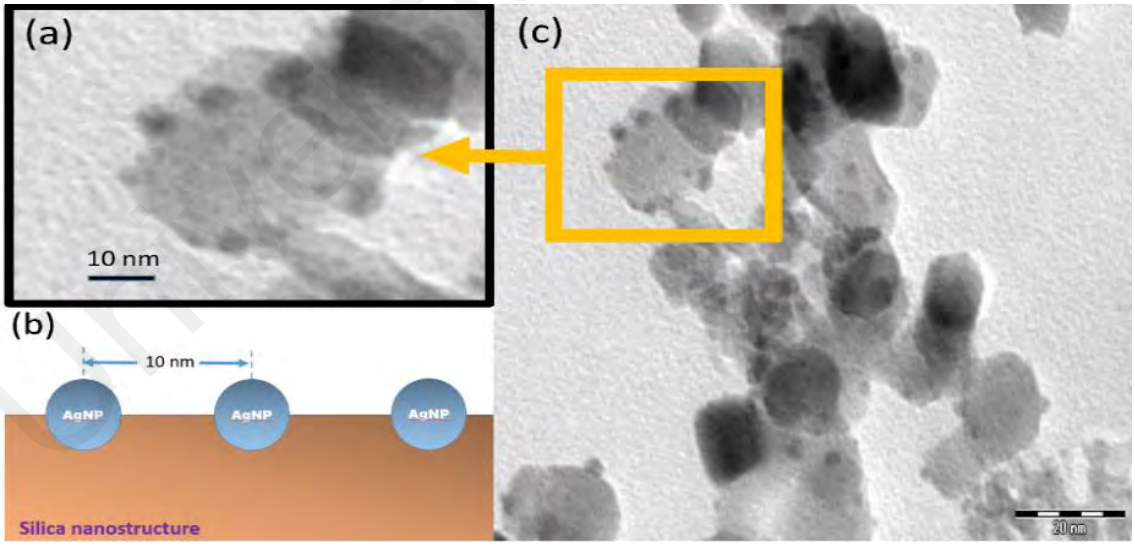

Figure 4.20: Morphological image shows the average inter-particle distance between AgNPs on the surface of SiO_2 nanostructure for filling fraction of Ag60 is 10 nm (b) ($\varepsilon_1 = -0.75$). (a) The small particles with the average size of 7 nm dominated by the surrounding SiO_2 nanostructures.

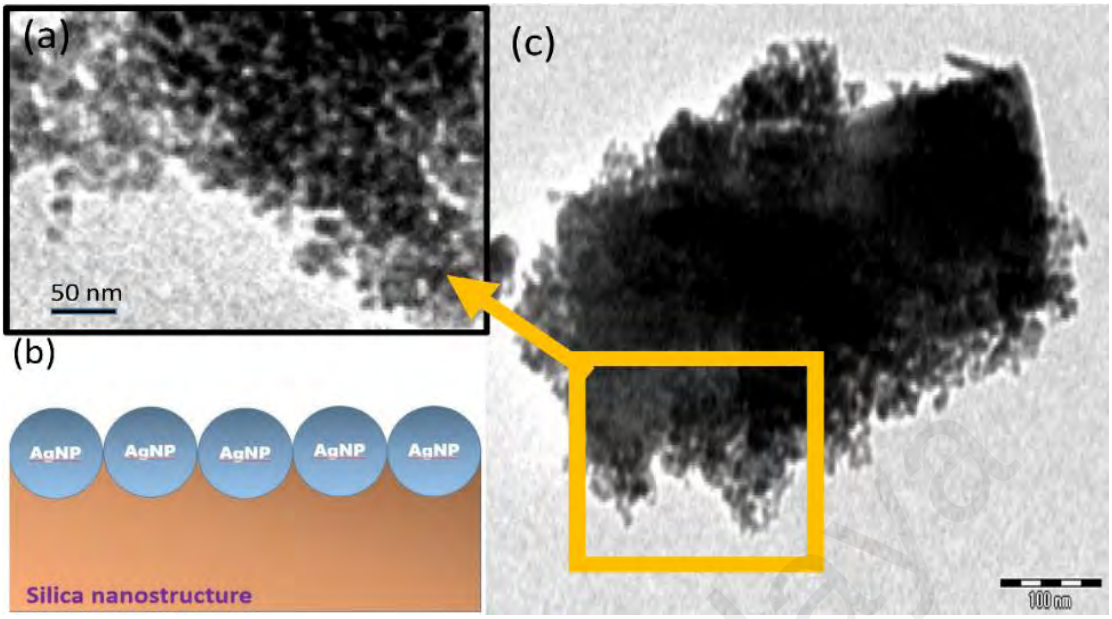

Figure 4.21: Morphological image shows the average inter-particle distance between AgNPs on the surface of SiO_2 nanostructure for filling fraction of Ag100 is less 2 nm (b) ($\varepsilon_1 = -1.1$). (a) The small particles with the average size of less than 2 nm dominated by the surrounding SiO_2 nanostructures.

4.4 Permittivity Studies

The permittivity of the dielectrics properties was obtained directly from Spectroscopic Ellipsometry (SE) (HORIBA, Model : MM16 System, France) measurement from two independent parameters ψ and Δ, known as the ellipsometric angles which represent the amplitude ratio and phase difference between the light waves, or also knows as the *p* and *s* polarized light waves. The dielectrics properties were analysed by Spectroscopic Ellipsometry (SE) which uses oscillator model to analyse the optical values from the measurements of the ellipsometric angles.

The spectra for real permittivity/dielectric constant ε_r at constant concentration and various filling fractions samples of Ag20, Ag40, Ag60, Ag80 and Ag100 are shown in Figure 4.22. The filling fraction determines the magnitude of the dispersion or the magnitudes of oscillating dipoles induced by light radiation onto the isolated AgNPs in the nanostructure. (Cha *et al.*, 2016). The spectrum of all filling fraction shows a decrease toward negative permittivity along the visible region compared to the host dielectric values. Samples with the filling fraction of Ag20 and Ag40 have a weaker dispersion while the other fractions of Ag80 and Ag100 show stronger dispersions. Whereas, for the filling fraction of Ag60, the dispersion pattern are almost stable as ageed in calculated data as Figure 4.23. The results indicate that the filling fraction determines the magnitude of the dispersion or the magnitudes of oscillating dipoles induced by light radiation onto the isolated AgNPs in the nanostructure. This could be the mechanism to determine the optimum filling fraction for the nanocomposite. Previous theoretical studies have shown that at a higher filling fraction of spherical metal nanoparticles to the substrate surface is the main reason for the strong dispersion in the polarizability of the ellipsometric angles where the inter-particle distance is smaller compared to the diameter size of the particles. This effect is due to the inter-particle plasmonic coupling phenomenon within sub-nanometer distances between the metal nanoparticles on the substrate surface (Xu *et al.*, 2006 ; Su *et al.*, 2003).

Figure 4.23 shows the effective permittivity pattern of nanostructures from all filling fractions which were calculated from Eq 2.6 (Maxwell Garnett equation) using the experimental properties of AgNPs and SiO_2. It can be observed that the curves are moving towards negative permittivity with the increase in the filling fraction of Ag/SiO_2.

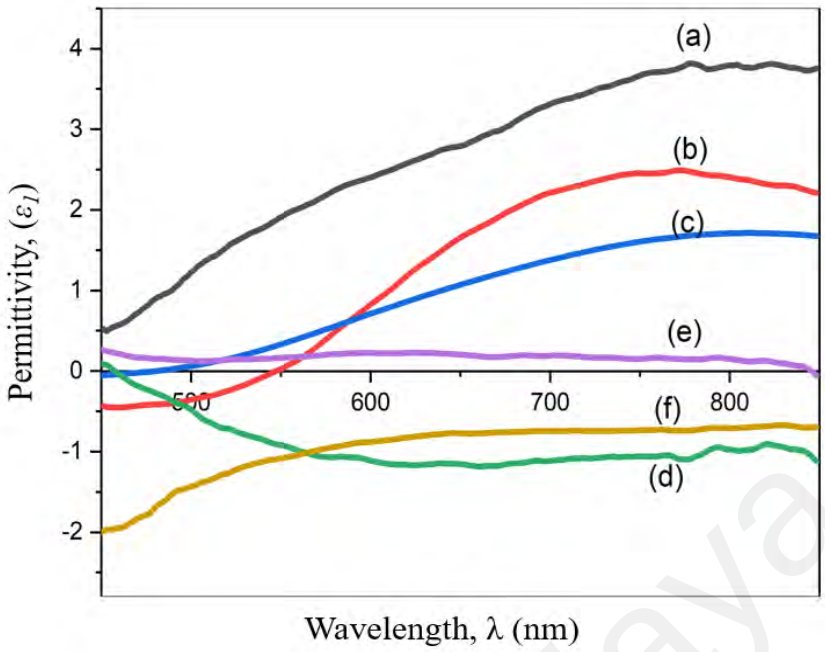

Figure 4.22: Spectra of the Ag-SiO_2 NC experimental effective permittivity for all samples, a) SiO_2 , b) Ag20 c) Ag40, (d) Ag60, (e) Ag80 and (f) Ag100. The dielectric constant decreases as the increase in the mass ratio. Strong dispersion occurs in Ag80 and Ag100 filling fraction.

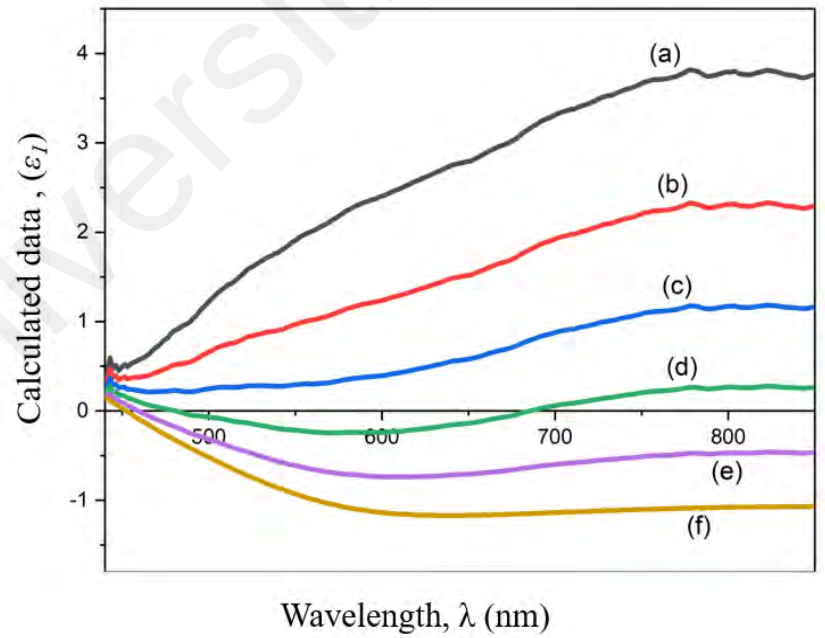

Figure 4.23: Spectra of the calculated values of effective permittivity from Maxwell Garnet equation using experimental data of AgNPs and SiO_2.

SE technique (HORIBA system) is also used to estimate the thickness of the thin film as shown in Table 4.3. The thickness of Ag-SiO_2 NC increases with the increase in the amount of AgNPs in the nanocomposite. The thickness of ITO is not affected throughout the EPD process. The thickness is calculated based on the formula; $\beta = 2\pi \left(\frac{d}{\lambda}\right) n_1 \cos(\phi_1)$ Where; β is the phase shift between two successive rays.

Table 4.3 : Sample thickness and optical properties at λ= 848 nm

Sample	Thickness (nm) Ag-SiO_2 NC	ITO	*n* (λ = 848 nm)
0.2	971.77 ± 2.33	215.30 ± 2.5	1.45
0.6	1026.87 ± 2.53	215.30 ± 2.5	1.28
1.0	1381.64 ± 2.31	215.30 ± 2.5	1.08
Pure SiO_2	731.42 ± 2.81	215.30 ± 2.5	1.84

Figure 4.24 summarizes the refractive index spectra of all filling fractions. The refractive index of the nanocomposite was obtained from the ellipsometric measurement. The Ag-SiO_2 NC nanostructure with a filling fraction of 0.6 possesses the lowest refractive index at 750 nm as shown in Figure 4.24. The refractive index spectra for all filling fractions show a decrease with the increase in the amount of AgNPs within the nanocomposite. The variation of filling fraction between AgNPs and silica nanostructures within the composite is the main factor which enables the tuning of the optical properties of the nanostructures. This is due to the role of AgNPs as the meta-atoms in the material polarizability magnitude (Cha et al., 2016). The refractive index of the thin film is from 0.27 to 1.84 in the spectral range of 50-850 nm. On the contrary, the spectral extinction coefficient (*k*) of the composite is relatively small. This is due to the absorption factor of

AgNPs which is greater than other metal nanoparticles. It describes the energy loss in the wave within the material which will determine the amount of attenuation as the electromagnetic wave propagates through the material. It also indicates how fast the incident light vanishes in a material due to absorption. The strong interaction of the AgNPs with light irradiation initiates the conduction of electrons on the metallic surface. The electrons on the nanoparticle surface undergo collective oscillations when excited by visible light (SPR effect) which results in an unusually strong scattering and absorption properties (Merlin *et al.*, 2009).

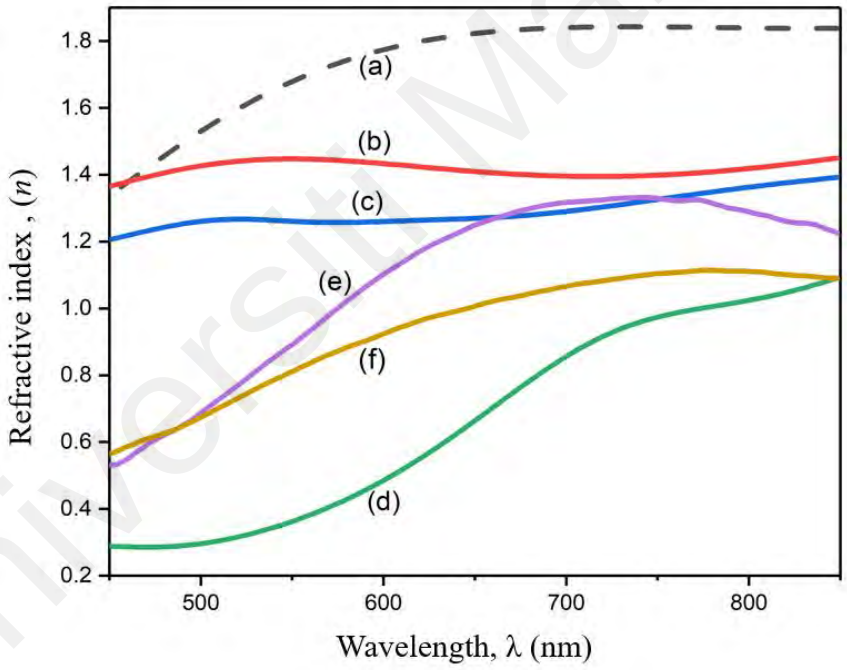

Figure 4.24: Spectra for refractive index for all filling fraction. All filling fractions shows a decrease in the refractive index with the increase in filling fraction. Where SiO_2, Ag20, Ag40, Ag60, Ag80 and Ag100 for (a), (b), (c), (d), (e), and (f) respectively.

Figure 4.25 shows that the real permittivity (ε_r) at 750 nm for the filling fraction of Ag20 is 2.28, with a refractive index of 1.39 as shown in Figure 4.26. At the same wavelength, the real permittivity (ε_r) is – 0.88 with a refractive index of 0.90 in Figure 4.27 and Figure 4.28 respectively, for a filling fraction of Ag60. The real permittivity (ε_r) of the filling fraction of Ag100 is –1.50 with a refractive index of 1.06 as in Figure 4.29 and Figure 4.30, respectively. This shows that the randomly distributed nanoparticle is tunable with consistent optical properties, effective near-field effect and polarizability in the nanostructures, with good results for a specific filling fraction, as summarized in table 3. This result agrees with a previous work which estimated that 2/3 of the filling fraction conforms to the MG model. The static polarizability oriented to the inter-particle axis customized the bonding and nonbonding interaction which causes the near field inter-particle coupling (Moiseev *et al.*, 2011; Jain *et al.*, 2007; Rechberger *et al.*, 2003).

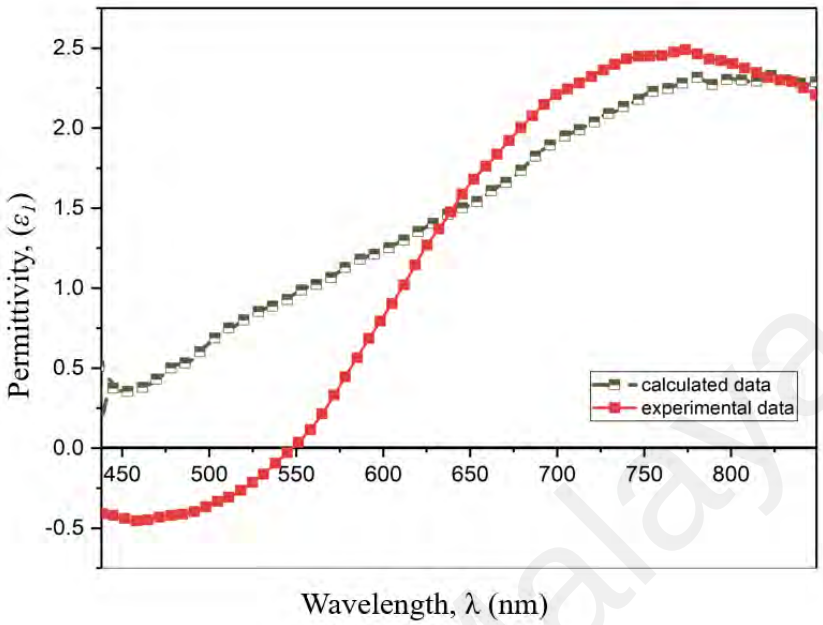

Figure 4.25: Real permittivity spectra for filling fraction Ag20.

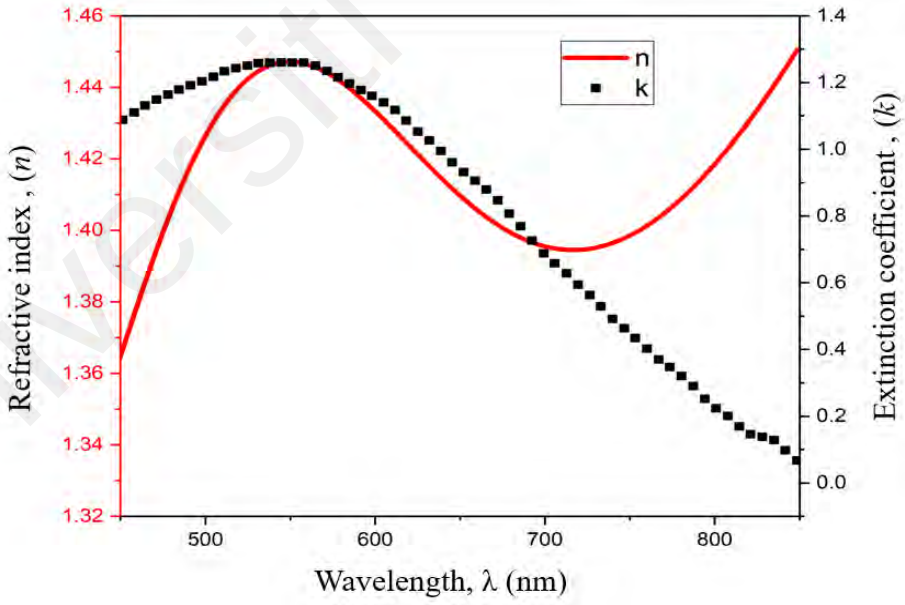

Figure 4.26: Refractive index and Extinction coefficient spectra for filling fraction Ag20.

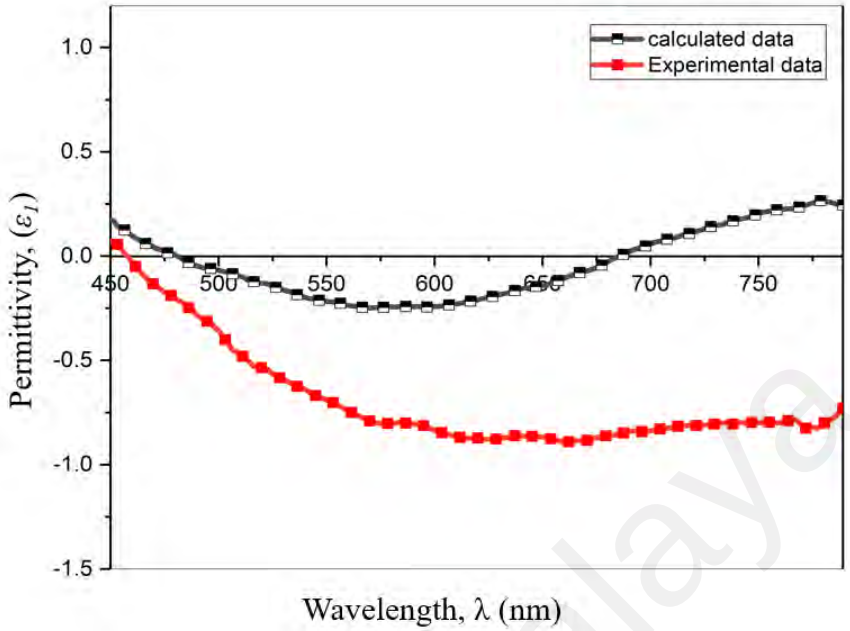

Figure 4.27: Real permittivity spectra for filling fraction Ag60.

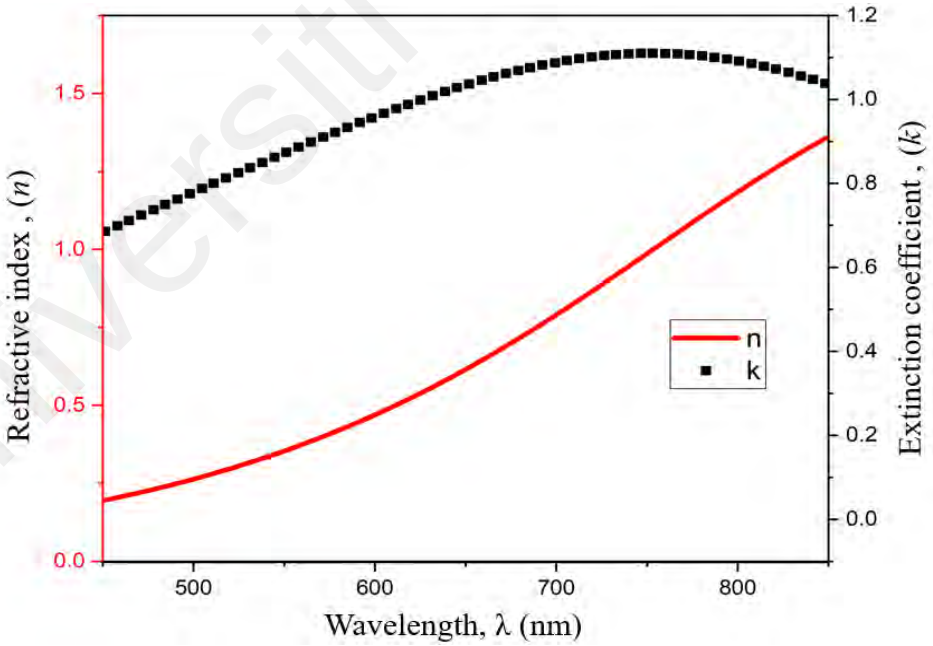

Figure 4.28: Refractive index and Extinction coefficient spectra for filling fraction Ag60.

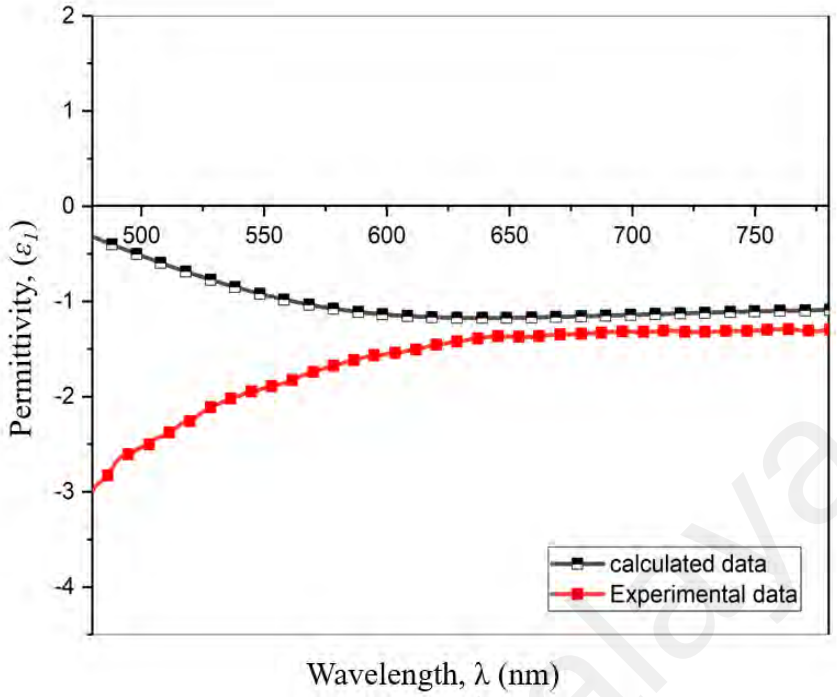

Figure 4.29: Real Permittivity spectra for filling fraction Ag100

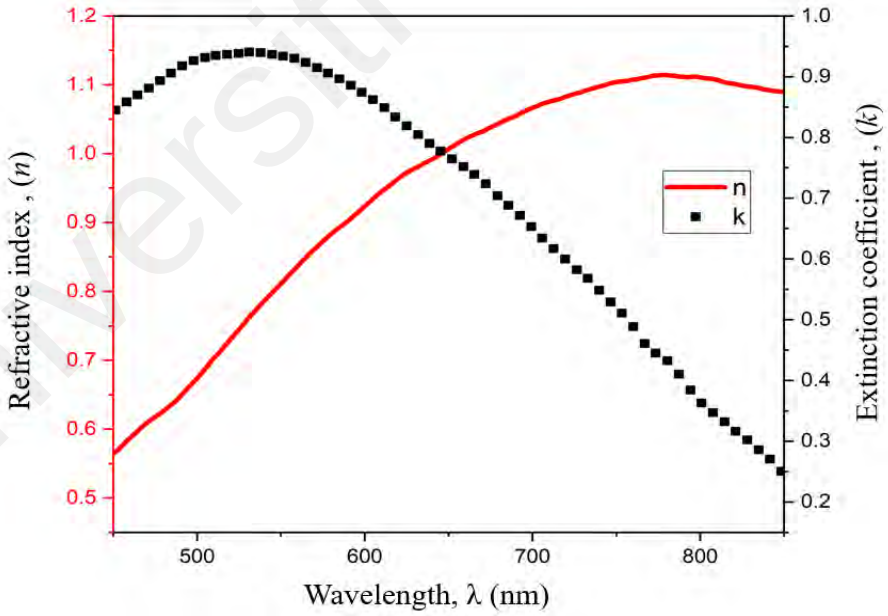

Figure 4.30: Refractive index and Extinction coefficient spectra for filling fraction Ag100

Table 4.4: Characteristics of Ag-SiO_2 NC at various filling fraction (λ= 750 nm)

Filling fraction	SPR λ_{max} (nm)	ε_r *(Experimental)*	ε_r *(calculated)*	n	Interparticle distance (nm)
0	-	3.74	3.08	1.81	-
0.2	456	2.28	2.24	1.39	15
0.4	455	1.40	1.13	1.32	-
0.6	453	-0.88	0.27	0.90	10
0.8	447	0.19	-0.47	1.33	-
1.0	435	-1.50	-1.13	1.06	< 5

The summary of the results are shown in Table 4.4. As the filling fraction of the AgNPs increases in the matrix, it leads to the dielectric and optical changes in the samples. This is due to the decrease in the average inter-particle distances. The decrease greatly enhances the dipole moment of the spherical AgNPs by excitation of the SPR that causes strong collective dipolar interactions between the AgNPs. The strong dipolar interactions in turn affects the linear and non-linear optical properties of the Ag-SiO_2 NC (Shalev, 2002 ; Bohrn et al, 1983; Marton et al, 1971;Xu et al, 2005). In this work, Maxwell-Garnett effective medium theory is used to describe the optical properties of the AgNPs in the nanocomposite and its dependence on the AgNPs filling factor. The theory might not correctly show the multipolar interactions between the nanoparticles (Markel *et al.*, 1991; Markel *et al.*, 1996) but it well describes the changes of dielectric properties and can be used to understand the effect of the metal filling fractions (Shalev, 2002).

CHAPTER FIVE:

STRUCTURAL, THERMAL AND ELECTROCHEMICAL STUDIES

5.1 Introduction

This chapter presents the results of thermal, structural and electrochemical properties of Ag-SiO_2 NC at various filling fraction. The aim of this chapter is to further characterize the optimum filling fraction of the Ag-SiO_2 NC. Thermal studies were performed by the Differential Scanning Calorimetry (DSC) and Thermogravimetric analysis (TGA), while electrochemical studies were performed by Electrochemical Impedance Spectroscopy (EIS).

5.2 Thermal Studies

5.2.1 Differential Scanning Calorimetry Analysis (DSC)

The thermal studies of pure SiO_2 and Ag-SiO_2 NC all samples were carried out using Differential Scanning Calorimetry (DSC). There is a single peak observed in all figures. Figure 5.1 shows the DSC curve for both pure SiO_2 and Ag20 for comparison. The graph depicts a strong endothermic peak which falls within 50 ºC to 140 ºC. The melting temperature, T_m obtained for SiO_2 at 108.7 °C agrees well as reported in pervious literature (Ding *et al.*, 2020). The nanostructured Ag-SiO_2 NCs for sample ID Ag20 showed a lower endothermal peak at 105.10 ºC, while the strongest peak belonged to pure SiO_2 as seen at 108.7 ºC.

The lower endothermal peak was caused by the enhancement of volume fraction of the amorphous phase, which favours the AgNPs transport and thus improve the conductivity of the nanostructure (Martinez *et al*.,2005). The results of the thermal analysis shows that the ΔH_m values for silica is -91.06 J/g and Ag20 is -90.20.4 J/g.

The values of relative crystallinity (χ_c) for all samples were calculated using the formula (Mohan *et al.*, 2007);

$$\chi_c = \frac{\Delta H_m^{sample} \times 100}{\Delta H_m^o} \quad (5.1)$$

Whereby the pure SiO_2 was taken as 100% in crystalline and ΔH_m^{sample} is the melting enthalpy value of the sample while ΔH_m^o is the value for melting enthalpy of pure SiO_2 (325 Jg^{-1}) (Jiang *et al.*, 2018).

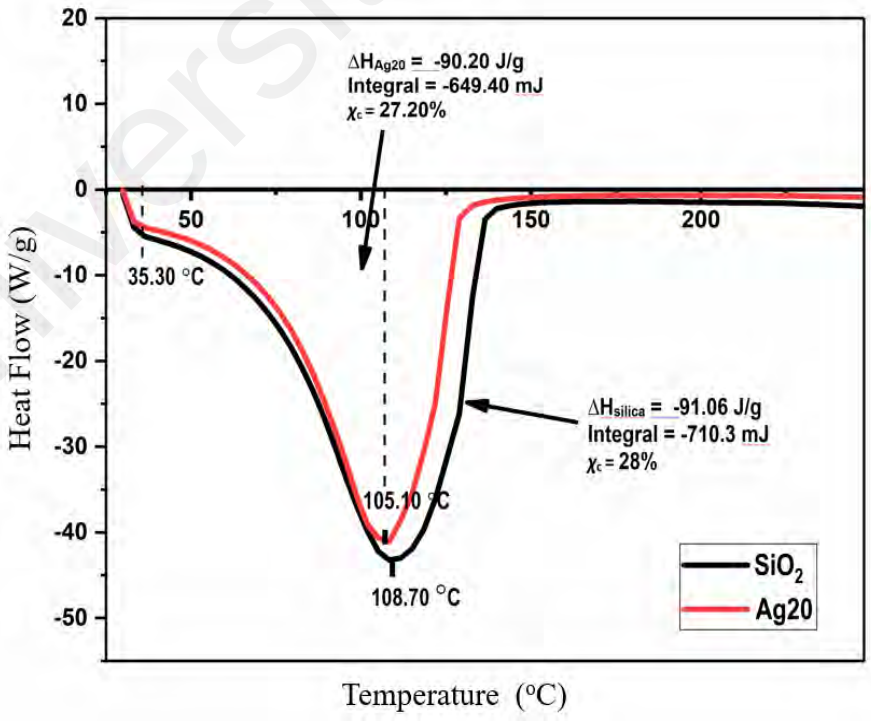

Figure 5.1: DSC thermogram for pure SiO_2 and Ag20.

In Figure 5.2, the sample ID Ag40 shows a decrease of the endothermic peak from 50 ºC to 104 ºC and the decrease in ΔH values from -90.20 J/g to -57.36 J/g. The transition of melting temperature in all samples is due to the increase of the amount of AgNPs in the nanostructure. The addition of nanoparticles to the host matrix nanostructure may contribute to the lowering of T_g and T_m by increasing the volume fraction of the amorphous phase caused by the modification of the host matrix.

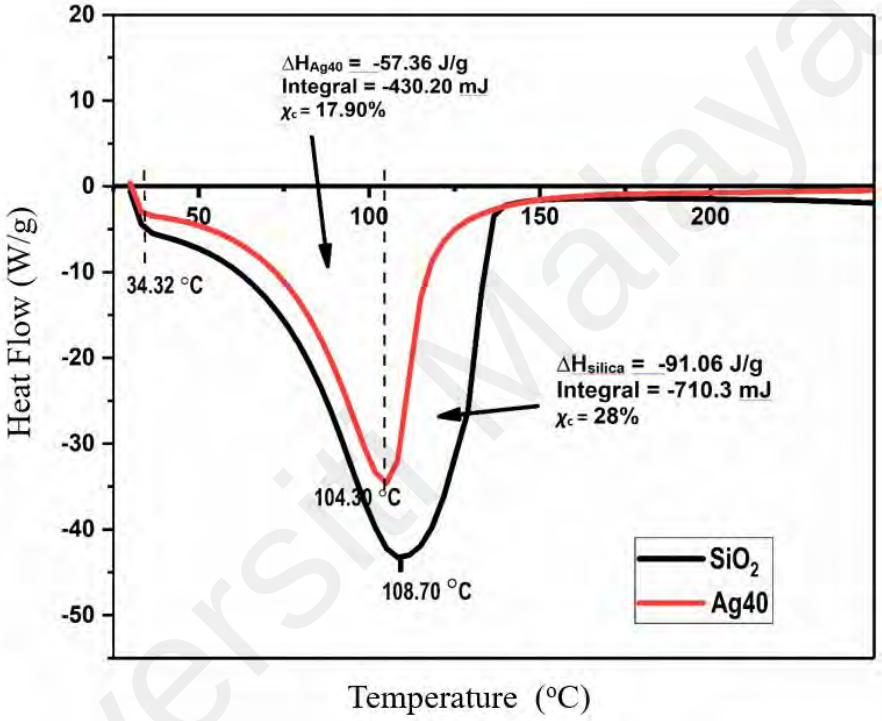

Figure 5.2: DSC thermogram for pure SiO_2 and Ag40.

Figures 5.3, 5.4 and 5.5 shows the same pattern of the decrease in T_m values of the other samples ID of Ag60, Ag80 and Ag100 at 102.17 ºC, 93.7 ºC and 91.6 ºC respectively. The decrease in ΔH values are shown as -55.32 J/g, -28.20 J/g and -27.9 J/g respectively for the rest of sample IDs.

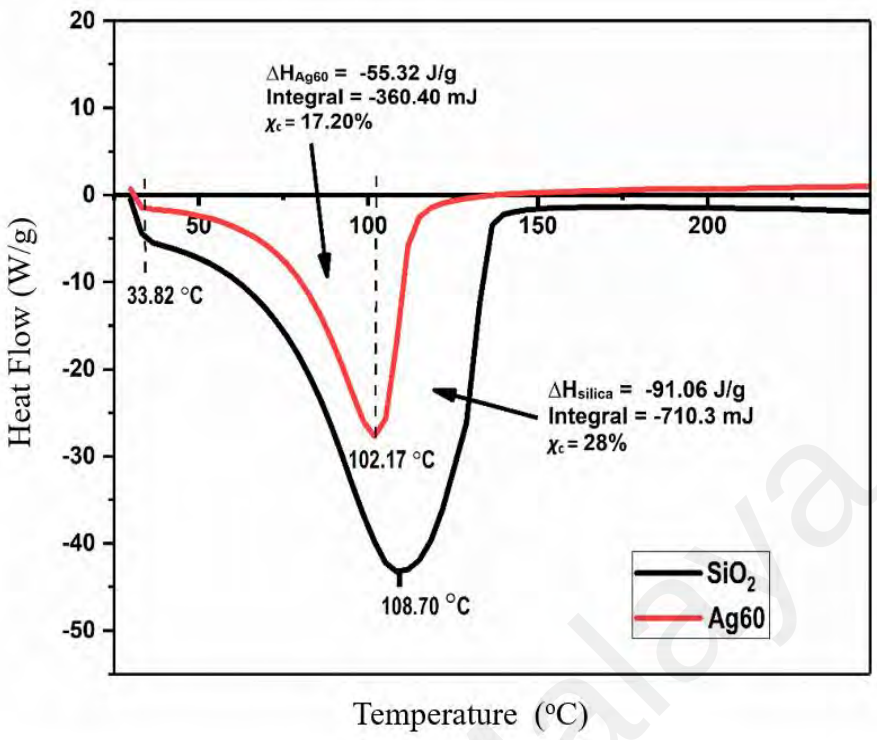

Figure 5.3: DSC thermogram for pure SiO_2 and Ag60.

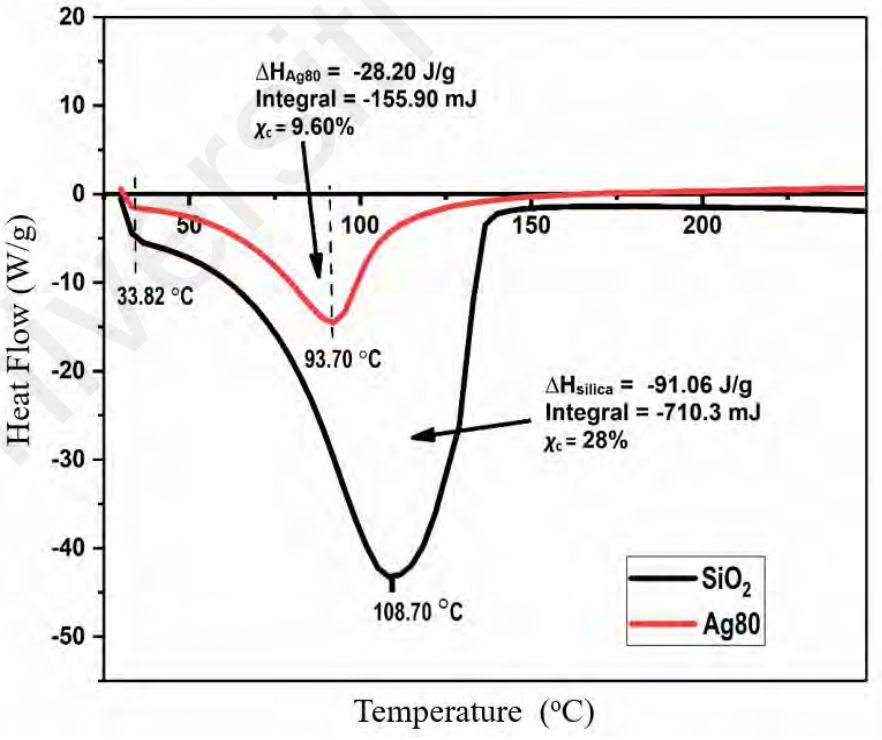

Figure 5.4: DSC thermogram for pure silica and Ag80.

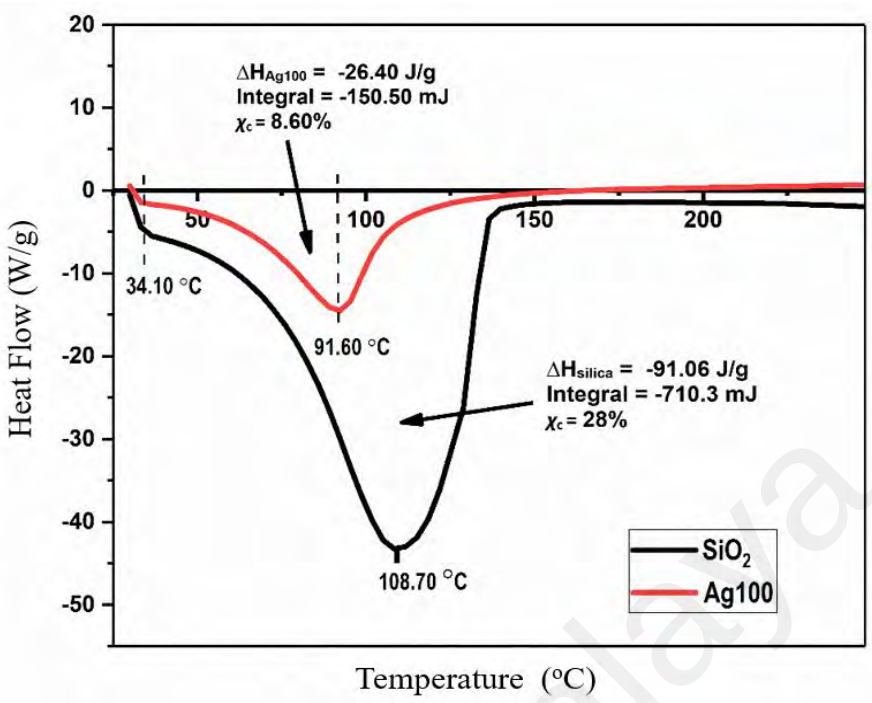

Figure 5.5: DSC thermogram for pure silica and Ag100.

Table 5.1: Thermal properties of pure SiO_2 and Ag-SiO_2 NCs.

Sample	**T_g (°C)**	**T_m (°C)**	**ΔH (J /g)**	**χ_c (%)**
Silica	35.20	108.7	-91.06	28.0
Ag20	35.20	105.10	-90.20	27.20
Ag40	34.20	104.30	-57.36	17.90
Ag60	33.82	102.17	-55.32	17.20
Ag80	33.82	93.70	-28.20	9.60
Ag100	34.10	91.60	-26.40	8.60

It is obvious from the Table 5.1 that the T_g, T_m, ΔH and χ_c shows a decrease due to the presence of AgNPs in the nanocomposite. The changes are due to the increase of volume fraction of the amorphous phase in the nanostructure. It is clear that the incorporation of AgNPs decreases the intensity of the endothermic peak of the nanostructure and changes in the melting endotherm was observed, indicating that the combination of AgNPs into the nanostructure has developed a new melting characteristic (Bandi *et al.*, 2006).

This is because as the amount of nanoparticles increase, the free volume becomes lower and creates numerous capillary effects on the evaporation temperature according to the amount of AgNPs present in the nanostructure. Table 5.1 reveals that AgNPs facilitates the crystallization of Ag-SiO_2 NC as a result of an increase in crystallinity. It should be pointed out that all samples IDs show the same trend. As for the significant change in ΔH of Ag20 to Ag40 and Ag60 to Ag80 compared to Ag40 to Ag60 and Ag80 to Ag100, this is due to the enhancement of conductivity. Therefore, AgNPs promote the crystallization process in the SiO_2 matrix. These observations clearly suggest that a major contribution to the conductivity enhancement comes from the structural modifications associated with the effects mentioned above (Hilonga *et al*., 2009).

5.2.2 Thermogravimetri Analysis Studies (TGA)

Figures 5.7 to 5.11 shows the typical weight loss (TGA) and derivatives of weight loss (DTG) curves of both samples while Figure 5.6 is the curves for the pure SiO_2. The degradation of all samples occurs in a single step starting at 90 °C and ending at 300 °C for the Ag-SiO_2 NC and for SiO_2. From the TGA curves, the values for the final

decomposition temperatures are determined. The decomposition temperature is determined from the DTG curves. As shown in Figure 5.6, the mass loss for pure SiO_2 begins at 97.30 °C and reaches maximum at 252.40 °C. The pure SiO_2 decomposes at 207.40 °C as reported in previous literature (Sen *et al.*, 2015).

Figures 5.7, 5.8, 5.9, 5.10 and 5.11 show the TGA-DTG results of samples ID Ag20, Ag40, Ag60, Ag80 and Ag100 respectively. All figures revealed single weight loss region. The single region originates from the decomposition of SiO_2 which agrees well with the previous work (Sen *et al.*, 2015). The temperature recorded for the other samples varies according to the amount of AgNPs incorporated into the nanostructure of the host matrix. The weight loss region could be ascribed to the loss percentage of adsorbed water and the residual of organic solvent (Yao *et al.*, 2007). The weight loss could also be related to the phase transition from a crystalline to an amorphous nanostructure. All samples with various filling fraction of Ag/SiO_2 begin to melt at 97 °C and the system is no longer stable.

The result of temperature values and percentage of weight loss are summarized in Table 5.2. It can be seen that the total weight loss are slightly decreased and the initial decomposition temperature also decreases with the increase in the amount of AgNPs. This indicates that the stability of the nanocomposite increases with the amount of AgNPs.

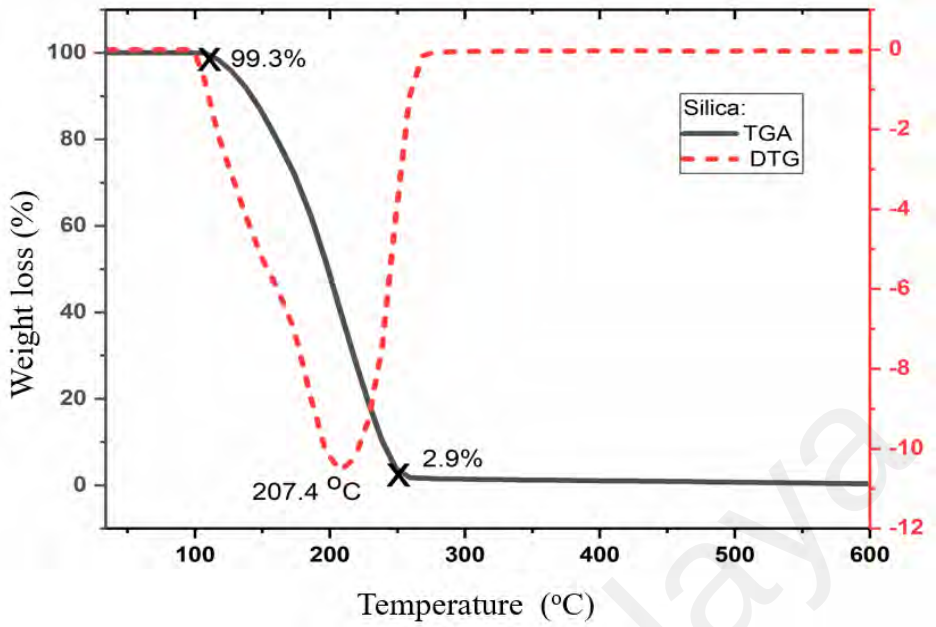

Figure 5.6: TGA-DTG curves for pure SiO_2

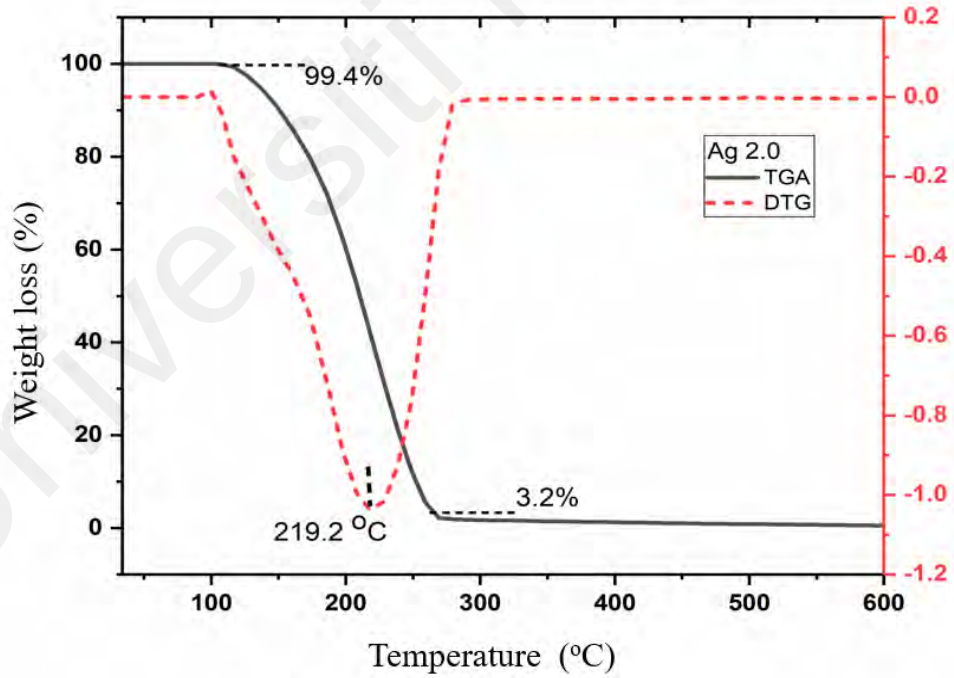

Figure 5.7: TGA-DTG curves for Ag20 sample

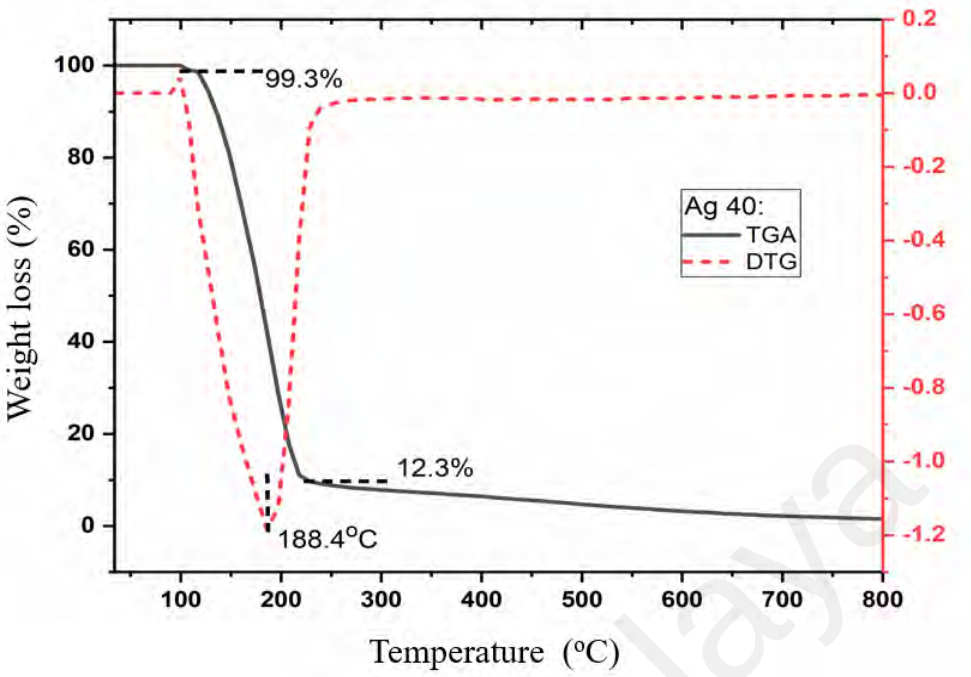

Figure 5.8: TGA-DTG curves for Ag40 sample

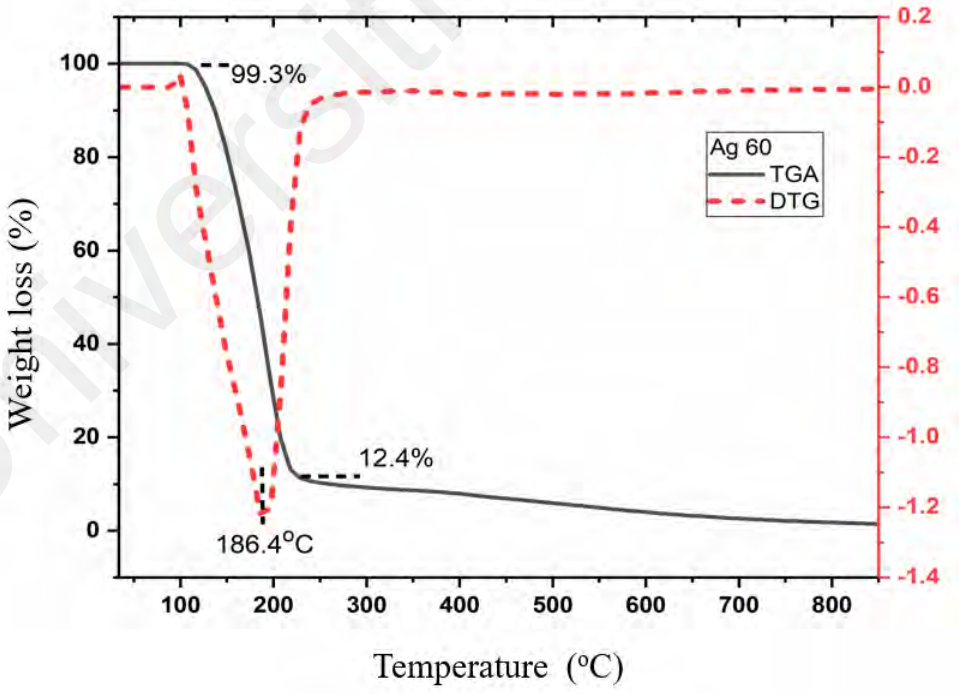

Figure 5.9: TGA-DTG curves for Ag60 sample

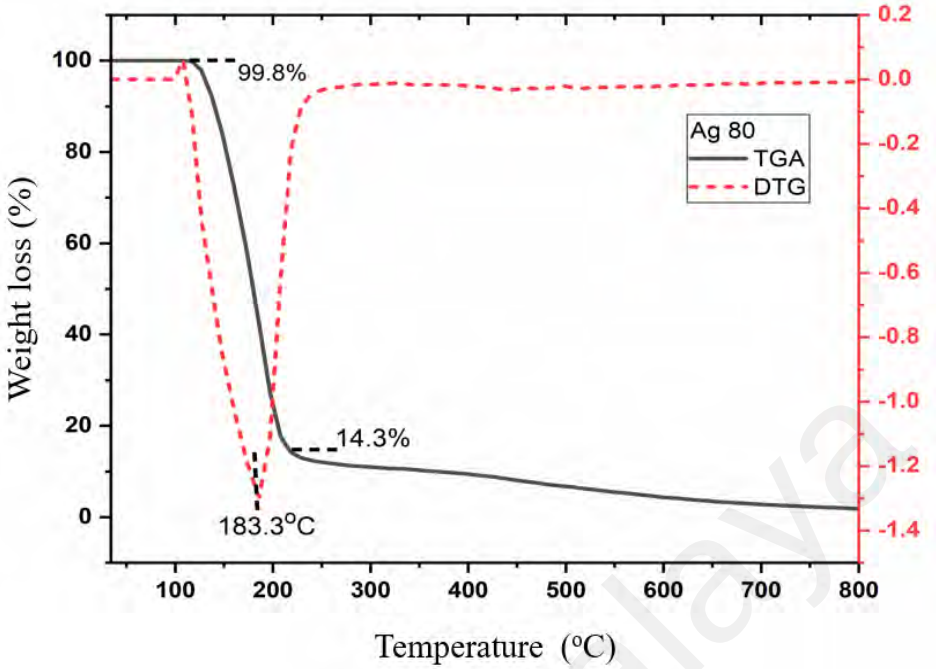

Figure 5.10: TGA-DTG curves for Ag80 sample

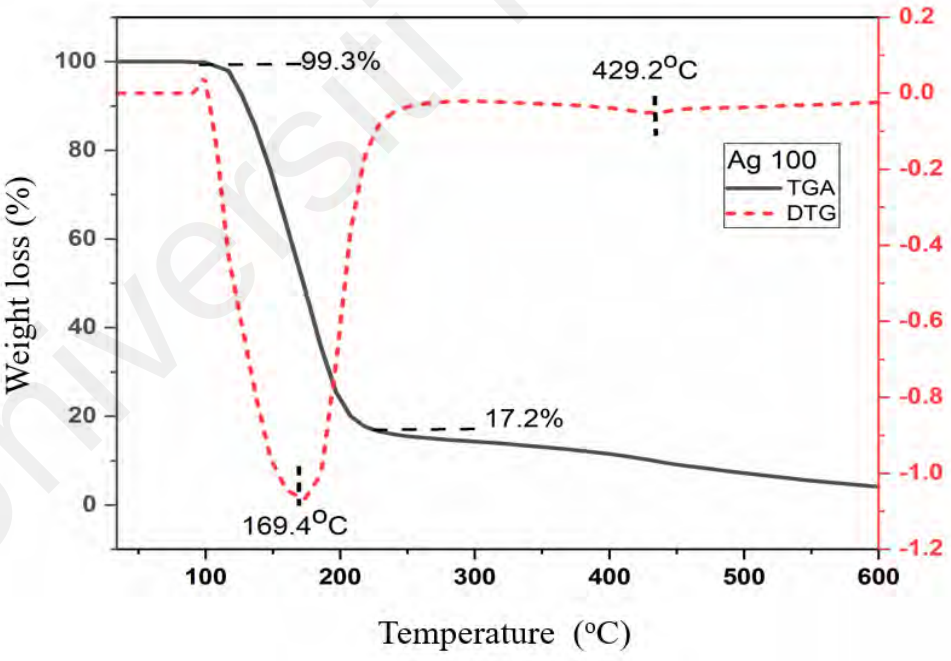

Figure 5.11: TGA-DTG curves for Ag100 sample

Table 5.2: Temperature values and percentage of weight loss and decomposition for Ag-SiO_2 NC samples at various volume ratio**.**

Sample	Initial weight loss temperature (<100 °C)	Final weight loss (%)	Decomposition temperature (>100 °C)	Total Weight loss (%)
Pure SiO_2	97.30	96.40	207.4	96.40
Ag20	99.50	96.20	219.2	96.2
Ag40	98.20	87.10	188.40	87.10
Ag60	97.10	86.90	186.40	86.90
Ag80	110.9	85.50	183.30	85.50
Ag100	108.23	82.10	169.40	82.10

5.3 Structural Studies

5.3.1 X-Ray Diffraction (XRD) Analysis

Figure 5.12 shows the XRD patterns of SiO_2 and Ag-SiO_2 NC. The bump with a broad diffraction pattern at $2\theta = 23^{o}$, similar for all samples is attributed to the amorphous structure of SiO_2 in the nanocomposite. The Ag-SiO_2 NC exhibit four well-resolved diffraction peak. The weak signal indicates the area dissipation of the AgNPs embedded into the surface of the silica nanostructure. The diffraction peak is only observed in the sample of optimum filling fraction. The four clear peaks at $2\theta = 38^{o}$, 44^{o}, 64^{o} and 77^{o} correspond to the AgNPs planes of 111, 200, 220 and 311(Liu *et al.*, 2014). The mean

size of the AgNPs (9.4 nm) embedded in the SiO_2 NPs was calculated using the Scherrer equation and is in good agreement with the size estimated from the TEM images. The Scherrer formula is as follows:

$$D = \frac{0.9\,\lambda}{\beta \cos\theta} \qquad (5.2)$$

Where D is the diameter of NPs related to the full-width at half maximum (FWHM), λ is the X-ray wavelength (0.1540 nm), β is the width at half-height of the diffraction peak of the nanoparticles/nanocomposite and θ is Bragg angle (degrees).

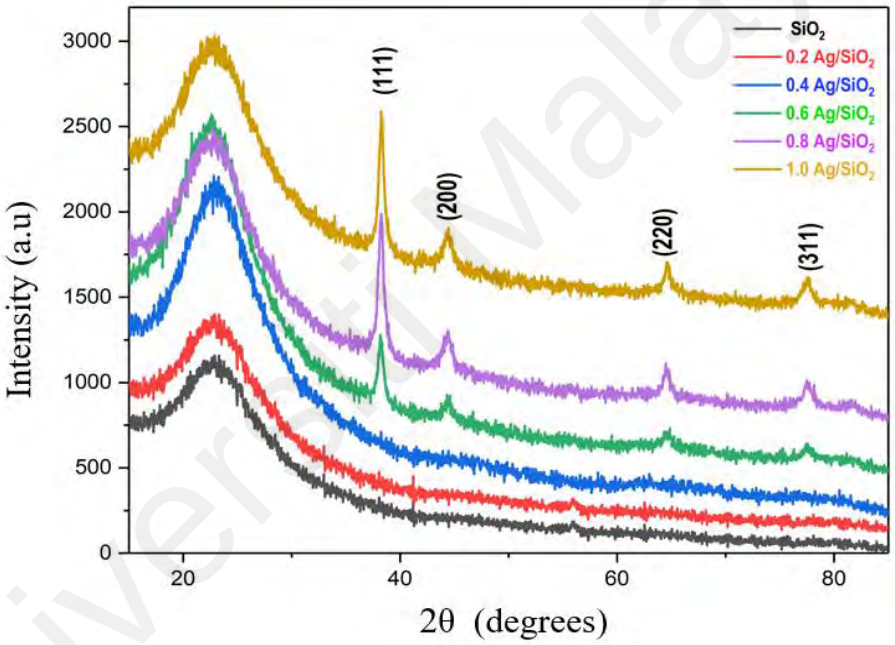

Figure 5.12: XRD patterns of SiO_2 and Ag/SiO_2 nanostructure for all filling fraction. Ag/SiO_2 exhibits the four well-resolved diffraction peak in the filling fraction of 0.6, 0.8 and 1.0 as shown in the top three pattern.

5.3.2 Fourier Transform Infrared (FTIR) Spectroscopy Analysis

Figure 5.13 presents the FT-IR spectra of the Ag-SiO_2 NC at various filling fractions. The observed peaks at 1053.34 cm^{-1}, 958.67 cm^{-1} and 788.46 cm^{-1} are the signature bands of the SiO_2 based on the symmetric and assymetric vibrations of the Si-O-Si bond. A

similar result was also reported (Racles *et al*., 2013) where the Si-O-Si vibrations occur between 1100 cm^{-1} and 470 cm^{-1}. SiO_2 nanoparticles also show peaks between 3327.21 cm^{-1} and 3404.21 cm^{-1} due to the stretching of –OH group in the nanostructures (Ibrahim *et al*., 2011). The presence of AgNPs in the SiO_2 network is assessed by the stretching of the Si-O-Ag at 1656 cm^{-1} and a similar spectra was also obtained in other work (Duhan *et al.*, 2010), where the vibration occured at 600 cm^{-1} and 1385 cm^{-1}. From the FTIR spectral analysis, the main advantage of SiO_2 nanostructures is its chemical inertness and the optical transparency towards the AgNPs which enables the spectroscopic monitoring of chemical reactions. Its particle surface can be also used to modulate the intensity of the AgNPs surface plasmon resonance bands, which influences the optical properties of the nanocomposite (Bahadur *et al*., 2011). Figure 5.14 shows the transmittance spectra of pure SiO_2 compared to the optimum filling fraction of Ag60 sample.

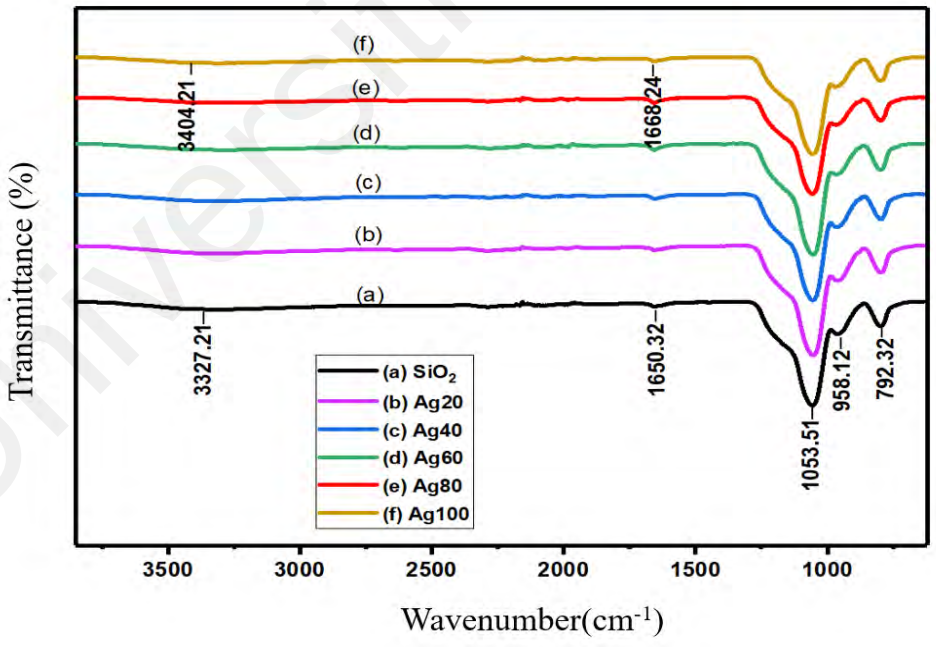

Figure 5.13: Transmittance spectra of pure SiO_2 (a) and all samples for Ag-SiO_2 NC with different Ag filling fractions (b-f)

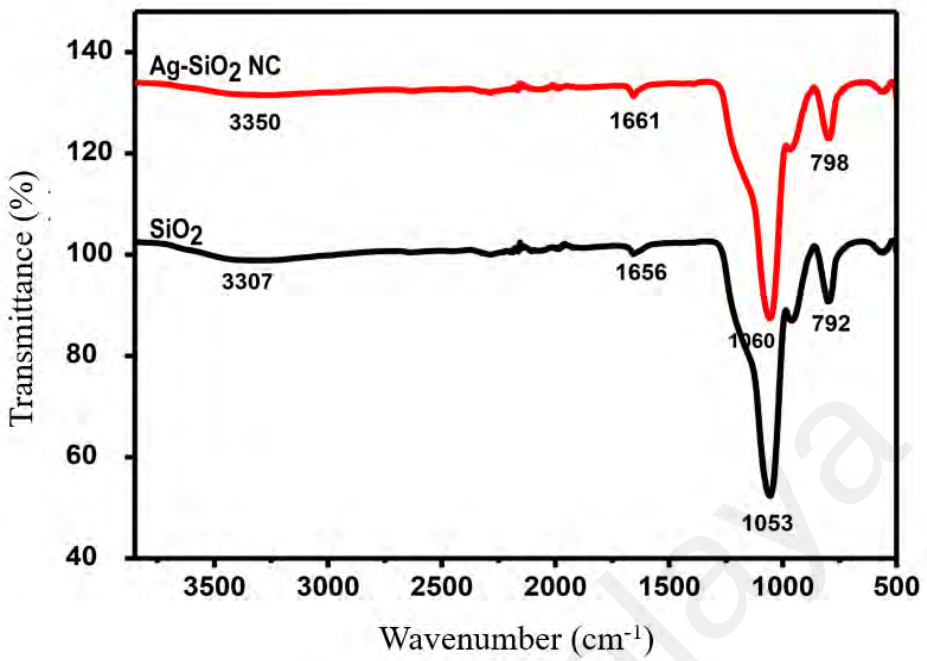

Figure 5.14: Transmittance spectra of pure SiO2 signature peak and the Ag60 of Ag-SiO_2 NC

5.3.3 Surface Enhanced Raman Spectroscopy (SERS) Analysis

Figure 5.15 (a) shows the normal Raman spectra of SiO_2 and Ag-SiO_2 NCs at the optimum filling fraction (Sample ID: Ag60). The five laser excitations at 295 cm^{-1}, 485 cm^{-1}, 561 cm^{-1}, 953 cm^{-1} and 987 cm^{-1} indicate the presence of the SiO_2 NPs. The bands at 485 cm^{-1} and 561 cm^{-1} are ascribed to the O-Si-O symmetric stretching vibrations. The bands at 953 cm^{-1} and 987 cm^{-1} are associated to the Si-O stretching region at higher frequencies, is blue shifted by 105 cm^{-1} and 74 cm^{-1}, respectively, due to scattering of the inhomogeneous SiO_2 nanostructures. There are no significant laser excitation seen for Ag60 in Raman spectra (Khan et al., 2016 ; Lee *et al.*, 2018).

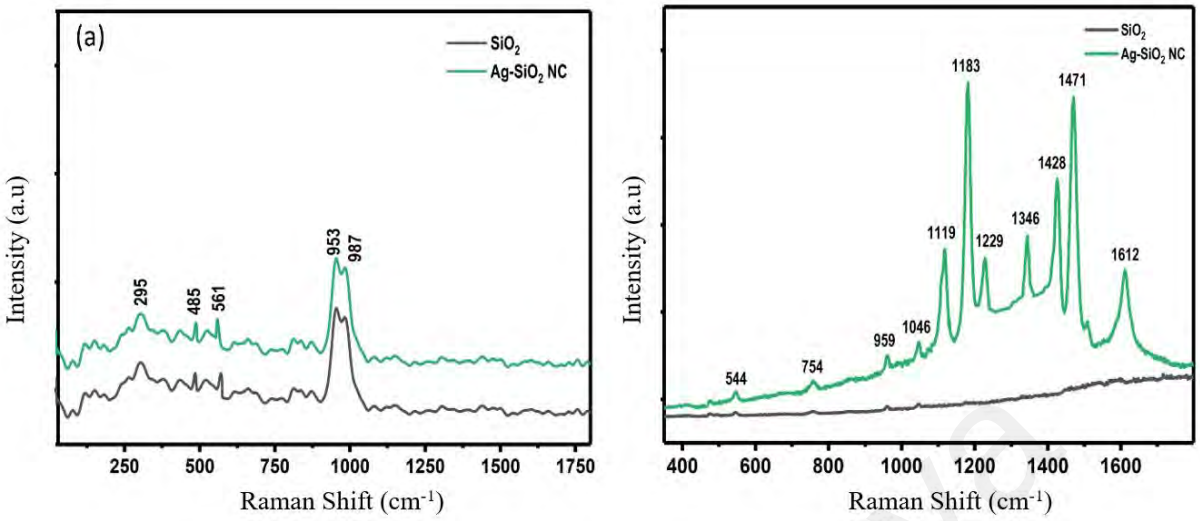

Figure 5.15: Spectra of (a) Normal Raman Scattering and (b) SERS spectrum for SiO_2 and Ag-SiO_2 NC.

Figure 5.15 (b) is the SERS spectrum of 4-ABT absorbed onto the AgNPs inter-particle junctions which are represented by several predominant peaks at 1183 cm^{-1}, 1428 cm^{-1} and 1471 cm^{-1}. These signals are attributed to the modes assigned to the b_2–type ring, which refers to the presence of a non-symmetric vibration related to the chemical enhancement mechanism. The low intensity bands at 1119 cm^{-1}, 1229 cm^{-1} and 1612 cm^{-1} is due to the a_1–type ring symmetric mode vibrations.

The excitation of the bands is due to the SPR of AgNPs and destructive interference which co-enhances the local electromagnetic mechanism (Kim *et al.*, 2011; Kim *et al.*, 2012). The 1183 cm^{-1} band is assigned to the C-S stretching mode b_2-type (7a) is red-shifted by 37 cm^{-1}. The 1428 cm^{-1} band assigned to the C-C stretch and C-H bending mode b_2–type (19b) is red-shifted by 26 cm^{-1}. The 1471 cm^{-1} band assigned to the C-C stretch and C-H bending mode b_2–type (19b) is red-shifted by 34 cm^{-1}. The 1119 cm^{-1} band assigned to the C-S stretching mode a_1-type (7a) is red-shifted by 39 cm^{-1}. The 1229 cm^{-1} band assigned to the C-H bending mode a_1–type (9a) is red-shifted by 28 cm^{-1}. The

1612 cm^{-1} band assigned to the C-C stretching mode a_1–type (8a) is red-shifted by 29 cm^{-1} (Suzuki *et al.*, 2016). Table 5.3 summarizes the stretching and bending modes of the spectra. The red-shift of all bands is due to the geometry of the substrate since the pH only affects the intensity of the bands (Xie *et al.*, 2014).

Table 5.3: Peak positions for 4-ABT on Ag-SiO_2 NC from Figure 5.15 (b) and their assignments.

SERS on 4-ABT	**Assignments**
1183 cm^{-1}	C-S stretching mode b_2-type (7a)
1428 cm^{-1}	C-C stretch and C-H bending mode b_2–type (19b)
1471 cm^{-1}	C-C stretch and C-H bending mode b_2–type (19b)
1119 cm^{-1}	C-S stretching mode a_1-type (7a)
1229 cm^{-1}	C-H bending mode a_1–type (9a)
1612 cm^{-10}	C-C stretching mode a_1–type (8a)

Figure 5.16 shows the SERS pattern of the sample with optimum filling fraction (sample ID: Ag60) with various intensity peaks at different pH values at room temperature. The predominant vibrational signals are observed at 1108 cm^{-1}, 1224 cm^{-1}, 1336 cm^{-1} and 1608 cm^{-1} due to the a_1–type vibration mode, while the bands at 1177 cm^{-1}, 1423 cm^{-1} and 1463 cm^{-1} are due to the b_2–type vibration mode. The broad spectral characteristics of acidic samples are likely caused by the spectral overlapping of inhomogeneously broadened vibrational signatures that originate from the aggregation of the nanoparticles (Herrera et al., 2013). The 4-ABT spectrum obtained with Ag-SiO_2 NC shows good enhancement in the basic environment. The intensity of the SERS signal varies as the pH increases. Herrera *et al*. found that the b_2-type bands of 4-ABT are very

weak or negligible in acidic medium, but are strong at basic pH from the interactions with the AgNPs (Uetsuki *et al.*, 2010). This is due to the instability of the resonating structures of the aniline group in the 4-ABT compound in the acidic medium. The combination of hydrogen ion with the amine group in 4-ABT at lower pH affects the a_2-type and b_2-type bands of 4-ABT. This weakens the electromagnetic enhancement (EM, a_1-type band) and chemical enhancement (CM, b_2-type band) at lower the pH. Figure 5.16 confirm that the SERS signal is tunable by alternating the pH values between 9.4 and 12.6.

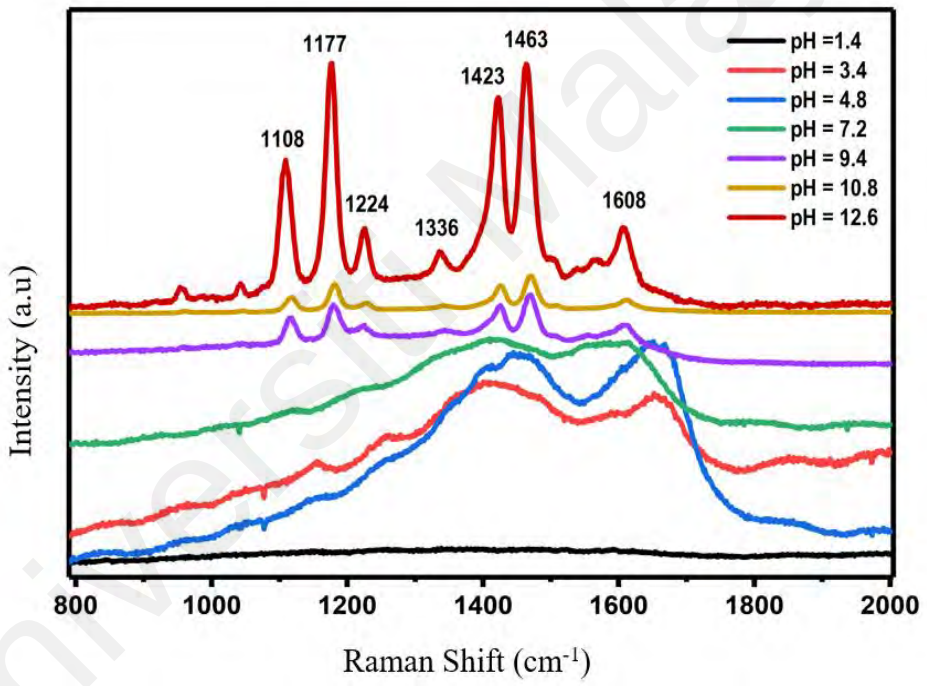

Figure 5.16: Spectra of SERS for Ag-SiO_2 NC optimum sample (Ag60) at different pH.

5.3.4 Zeta Potential (ZP) Analysis

The stability of AgNPs and Ag-SiO_2 NC particles suspension in their colloids solutions is important to ensure there are well disperse in their colloids solution. Zeta Potential measurements are significant to determine the stability. The ZP measurement is based on the potential at the surface of shear. It refers to the plane surface of the particles and the dispersion media. The potential exists due to the discrepancy in fermi energy of the particle and the electrolyte. Table 5.4 shows the values of zeta potential for AgNPs and Ag-SiO_2 NC at various filling fraction (Ag20, Ag40, Ag60, Ag80 and Ag100). It was observed that the AgNPs is stable having the ZP values in the range of -29.0 mV to -36.3 mV. Higher ZP values are more desirable for stable suspensions. It shows that Ag-SiO_2 NC is more stable as the amount of AgNP increased.

Table 5.4: Zeta Potential for AgNPs and Ag-SiO_2 NC

Particle	Zeta Potential (mV)	Mobility (μmcm/Vs)
AgNP	-29.0	-2.27
Silica	-34.1	-2.67
Ag20	-29.4	-2.31
Ag40	-33.9	-2.66
Ag60	-33.6	-2.63
Ag80	-37.3	-2.93
Ag100	-36.3	-2.85

5.4 Photoelectrochemical Studies

The synthesized Ag-SiO_2 deposited on the ITO by Electrophoresis Deposition (EPD) method was investigated for its photoelectrochemical water splitting characteristics using Linear Scan Voltammetry (LSV) method, in 0.5 M NaOH at a scan rate of 50 mV s^{-1} under dark and simulated solar irradiation of AM 1.5 G (100 mW cm^{-2}). The I-V plot for all samples is presented in Figure 5.17 which shows that photoactivity commences at slightly negative potential with respect to the Ag/AgCl reference electrode. As the potential increases to the positive region, a steady increase in the photocurrent is observed for all samples indicating the n-type nature of thin film and photoanodic behavior against counter electrode.

It can be seen in Figure 5.17 that the samples of Ag-SiO_2 NC thin film electrode generates a photocurrent density of 0.38 mA cm^{-2} under illumination conditions at a bias potential of +0.53 V for Ag100 and followed by the rest of the samples with a bias potential of +1.0V (Ag20), +0.9V (Ag40), +0.92V (Ag60), +0.82V (Ag80). The curve trend for Ag100 which is at Figure 5.17 (e) differ from the rest of the samples as it contained with the highest filling fractions of AgNPs. This catalytic performance is probably due to the SPR effect (Liz-Marzan *et al.*, 2006; Chen *et al.*,2010).

It is obvious that the various amount of AgNPs presents in the nanostructure controls the enhancement of the light trapping in the thin film which is characterized by the plasmonic properties of the metal nanoparticles (Kumar *et al.*, 2013; Yoon *et al.*, 2010). Thus, the presence of AgNPs on semiconducting SiO_2 nanostructure not only enhances the area of the surface but it also enhances the electro-chemical stability of the nanocomposites, improve the conductivity and the photocatalytic activity (Zheng *et al.*, 2008).

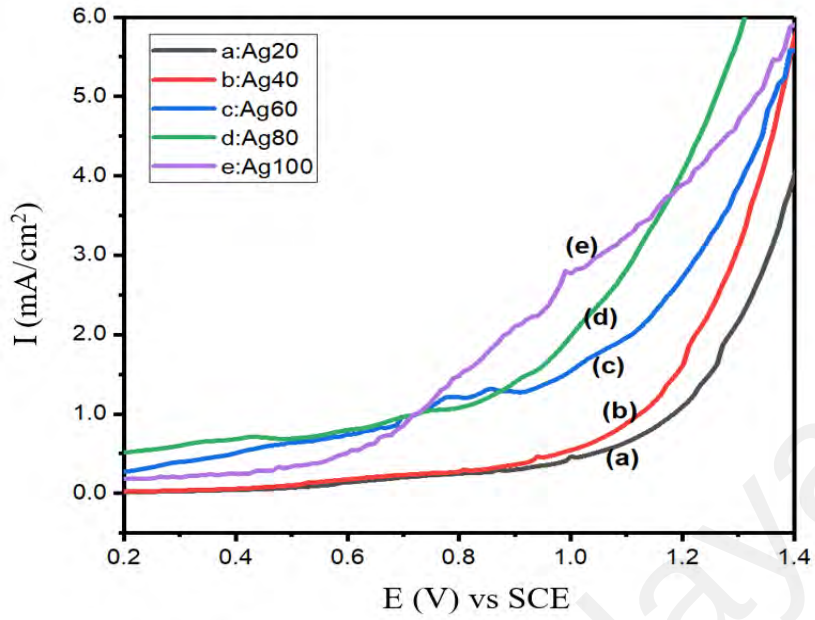

Figure 5.17: Current-Voltage (I-V) plot for all samples fabricated as thin film deposited on ITO and immersed in 0.5 NaOH simulated with AM 1.5G illumination of 100 mW cm^2 at a scan rate of 50 mV s^{-1}.

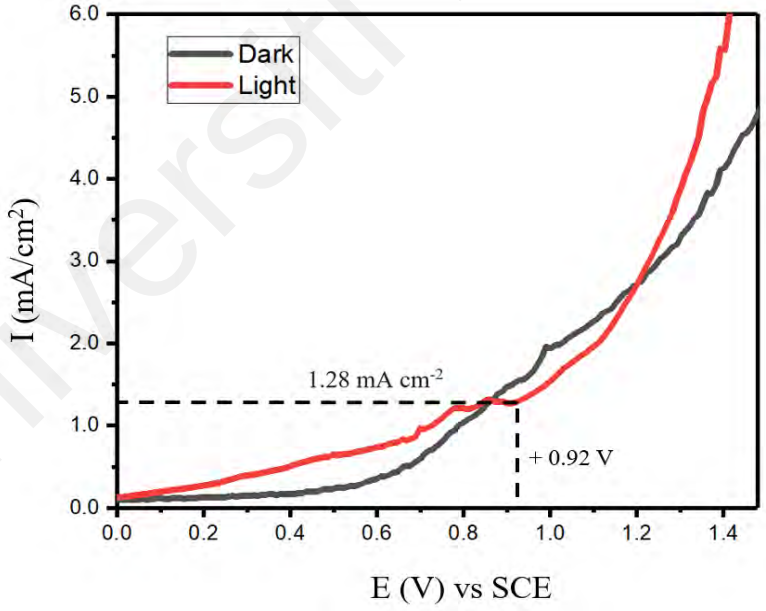

Figure 5.18: Current-Voltage (I-V) plot for sample ID Ag60 fabricated as thin film deposited on ITO and immersed in 0.5 NaOH simulated with AM 1.5G illumination of 100 mW cm^2 at a scan rate of 50mV s^{-1}.

Figure 5.18 shows the I-V plot for optimum filling fraction sample (sample ID Ag60) thin film electrode produce photocurrent density of 1.28 mA cm^{-2} under illumination conditions at a bias potential of +0.92 V as shown in the graph. The presence of photocurrent under the dark conditions is the results of crystal defects and lattice mismatch that facilitates temporary storage of electric current which creates pseudocapacitor and results in high dark current(Takenaka *et al.*, 2012).

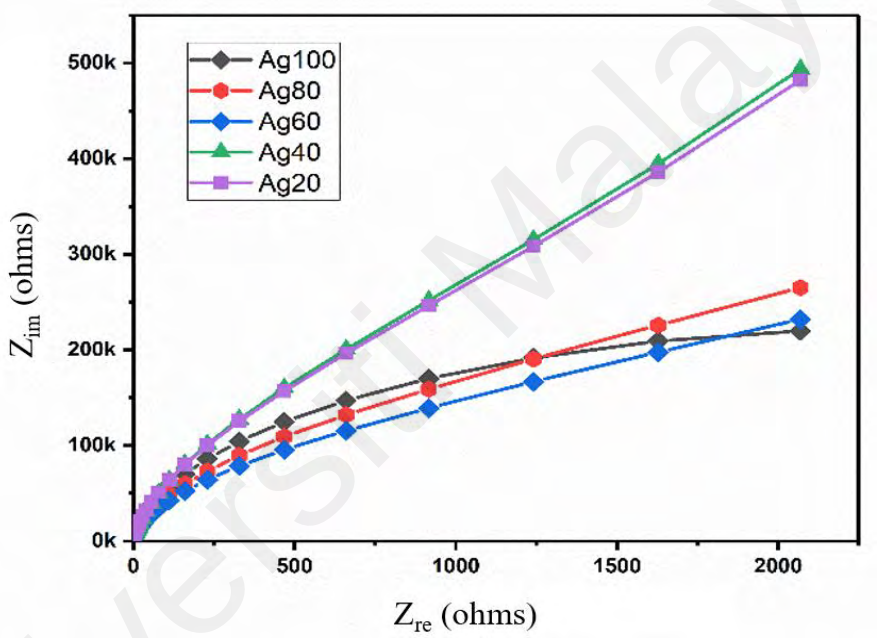

Figure 5.19 Nyquist plot obtained for the Ag-SiO_2 NC thin film in the presence of 0.5 M NaOH at frequencies ranges of under light illumination.

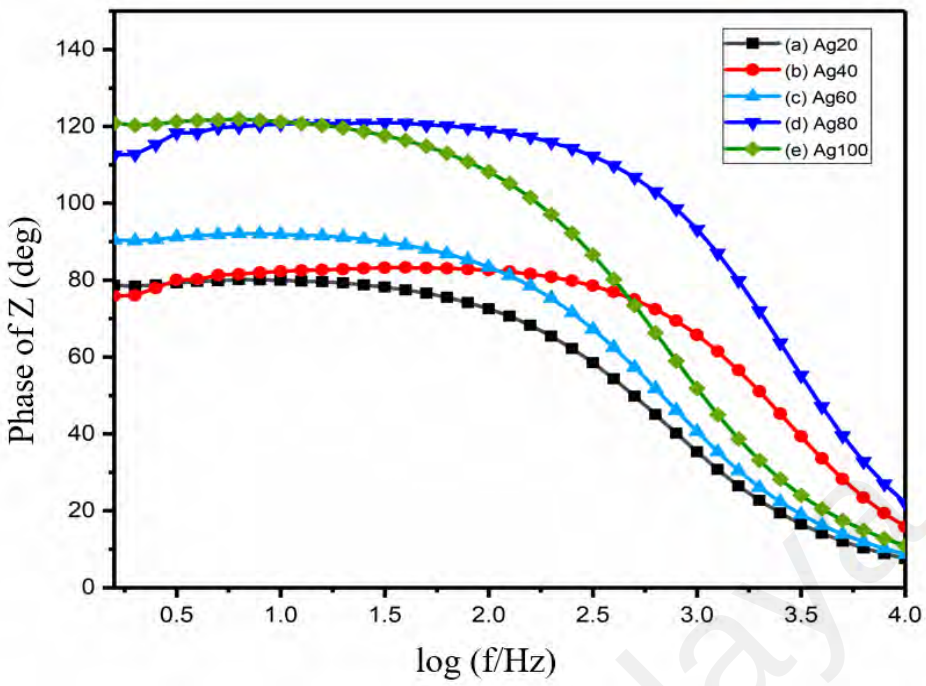

Figure 5.20 The Bode angle phase plot of all samples in the presence of 0.5 M NaOH at the frequencies ranges of 0.1 Hz to 10 kHz under light illumination.

The conductivity of the electrode and analysis of charge transfer kinetics in the semiconductor electrode/electrolyte interface were studied using Electrochemical Impedance Spectroscopy (EIS). The Nyquist and Bode plots were obtained from the EIS analysis under the dark and illumination conditions for Ag-SiO_2 NC deposited on ITO as thin film. Figure 5.19 shows the Nyquist plot of all samples. The semicircle diameters of all these plots extend to the lower frequencies which represents the charge transfer resistance determine the electronic properties of the electrode. Figure 5.19 also shows that the R_{ct} values of the Ag-SiO_2 NC thin film decrease upon illumination, which indicate the increase in the charge carrier due to low charge transfer resistance in the electrode interface and the decrease in the charge recombination. The decrease in the resistance in the thin film is due to the increase in the amount of AgNPs in the SiO_2 nanostructure (Li *et al.*, 2019).

The Bode plots of all samples are shown in Figure 5.20. From the plot, the maximum frequency of all samples shift towards lower frequency region under illuminated conditions. This is due to the rapid electron-transfer process in the Ag-SiO_2 NC thin film. The possible process is based on the separation of electron and hole pairs in the Ag-SiO_2 NC films induced by AgNPs, as it plays a role as the redox catalyst and contribute to the catalytic reaction (Hu *et al.*, 2018; Guo *et al.*, 2011).

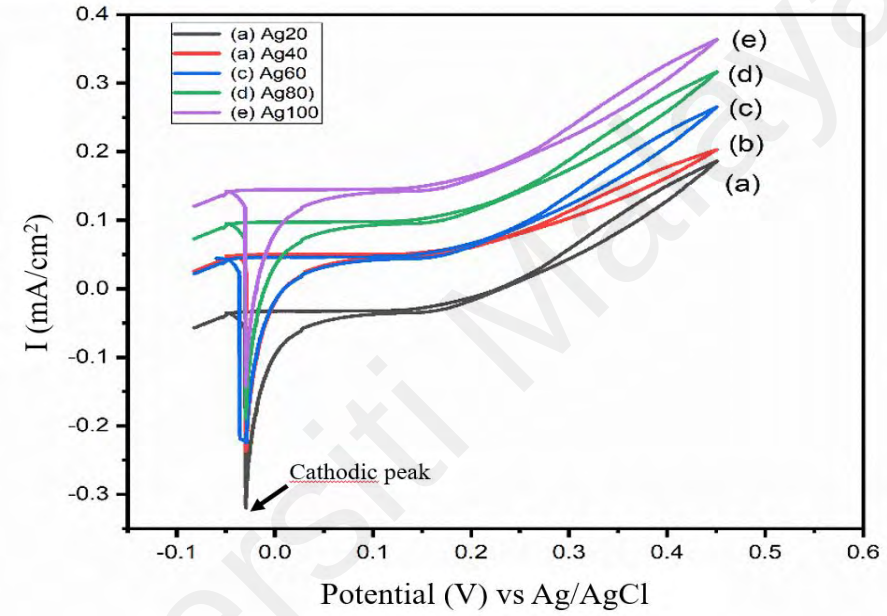

Figure 5.21. Cyclic voltammetry for all samples under illuminated conditions.

Figure 5.21 shows the cyclic voltammetry for all samples of Ag-SiO_2 NC under visible illuminated conditions. The deposited Ag-SiO_2 NC of all samples were used as the photoanode in the electrode of the photo-electrochemical cell. All samples show a cathodic (redox) peak at – 0.02 V (vs. Ag/AgCl reference electrode) which is attributed to hydrogen evolution (Guitoume *et al.*, 2018). However, there is no obvious oxidation peak observed in the anodic current which indicates that the photoanode is stable throughout the photo-electrochemical measurement. The obvious cathodic peak is driven from the photocurrent due to the reduction of the AgNPs and separation of the excited charges of electron-holes pairs at the SiO_2 / Ag/ electrolyte interface.

As shown in Figure 5.22, when the AgNPs is irradiated under the illuminated conditions, the photo-excitation of the electron-hole pairs is generated in the AgNPs due to the effect of LSPR (Tian *et al.*, 2005). These charges are then transferred to the SiO_2 so that most of the charges could be transported to the counter electrode via the ITO. At the counter electrode (Pt), the H^+ is reduced at the electrode/electrolyte interface and the photocurrent is generated (Kazuma *et al.*, 2012). The amount of photocurrent generated depends on the amount of AgNPs present in the sample. The weak photocurrent under visible light is due to the lattice mismatch of the SiO_2 (Paulose *et al.*, 2006).

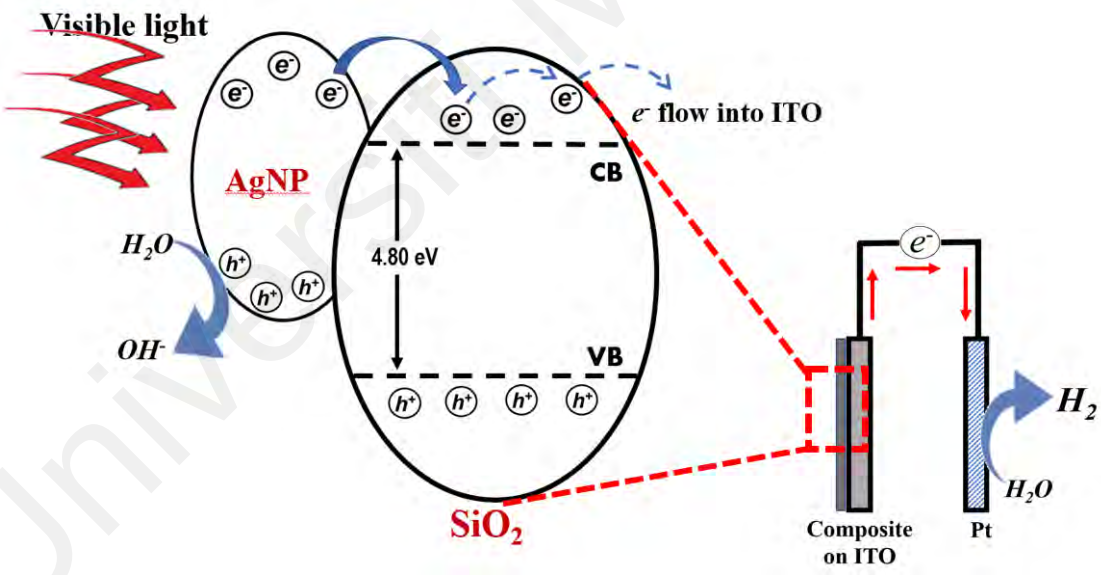

Figure 5.22: Mechanism of photocatalytic of Ag-SiO_2 NCs under illuminated conditions.

The photocurrents are generated under illuminated conditions following the major reactions:

Plasmon-excitation at the surface of AgNPs by visible light :

$$2Ag + h\nu \rightarrow 2Ag\ (e^- + h^+) \quad (5.3)$$

Excited photo-electrons transfer from AgNPs to the SiO_2 conduction band:

$$2Ag\ (e^- + h^+) + 2\ SiO_2 \rightarrow 2SiO_2\ (e^-) + 2Ag\ (h^+) \quad (5.4)$$

The generated photo-electrons transfer from the SiO_2 to the counter electrode (*Pt*) through the external circuit via the ITO:

$$2SiO_2\ (e^-) + 2Pt \rightarrow 2\ SiO_2 + 2Pt\ (e^-) \quad (5.5)$$

The evolution of hydrogen at Pt electrode:

$$2Pt\ (e^-) + 2H^+ \rightarrow H_2 + 2Pt \quad (5.6)$$

As from the sequential process shown in Figure 5.22, the photocatalytic process begins with the incident photon which excites the Local Surface Plasmon Resonance (LSPR) of the AgNPs, which eventually decays to produce the excited electron-hole pair distributed over a wide range of energies and an equilibrium state is created between the Conduction

Band (CB) and Valence Band (VB) position of the AgNPs and SiO_2. The resulting inner electric field effectively transfers the photo-generated electrons and holes to the CB of SiO_2 and VB of the AgNPs. The electrons with higher energy will have the potential to move from the excited AgNPs into the vacant states of the nearby molecules of SiO_2 (Hartland *et al.*, 2017). From Figure 4.4, the Uv-Vis spectroscopy shows the estimated band gap energy of Ag-SiO_2 NC of 2.03 eV at the optimum filling fraction (Ag60) and this justifies the possibility of the electron transfer from AgNPs to the host matrix of SiO_2 in the nanostructure. Whereas the thermodynamic reversible potential for the hydrogen production is V_{rev} = 1.229 V (Grimes *et al*., 2007). The band gap energy of SiO_2 is estimated as 4.80 eV, this justifies the effective high energy band gap in SiO_2 for the photocatalytic process, as it decreases the recombination rate of the photo-generated charges (Dutta et al., 2016).

CHAPTER SIX:

CONCLUSIONS AND RECOMMENDATIONS

6.1 Overview

In this research, AgNPs with desired optical properties and Ag-SiO_2 NC at various filling fraction were successfully synthesized via chemical reduction method and sol-gel technique, respectively, followed by Electrophoretic Deposition (EPD) to form Ag-SiO_2 NC film. All samples were characterized using several analytical techniques. The main objective of this research was to synthesize AgNPs and Ag-SiO_2 NC at the optimum composition of AgNP/SiO_2 based on the volume filling fraction.

As a consequence, the Maxwell Garnett model was used as the Effective Medium Theory (EMT) for the volume filling fraction method. Special focus was made to the Permittivity studies. The morphologies of the AgNPs and Ag-SiO_2 NC were studied using TEM while the changes in the optical properties from various volume filling fraction were extensively characterized by UV-Vis and PL spectroscopy while the structural changes were characterized by XRD, FTIR and Raman Spectroscopy. For further applications, the samples were characterized by Impedance Spectroscopy.

In summary, the Ag-SiO_2 NC with various filling fractions were successfully synthesized by the sol-gel method and deposited onto ITO substrate via the EPD process. The structural and optical studies of the Ag-SiO_2 NC at various filling fractions were investigated and the conclusions are summarized as follows:

(1) All samples of AgNPs and Ag-SiO_2 NC measured using TEM technique were within a diameter range of 5.00 – 50.00 nm. Most of the AgNPs were in the range of 10 to 40 nm. Using the UV-Vis technique, the absorption edge, direct band gap and indirect band gap values showed a decrease upon doping with AgNPs to the pure SiO_2, which was responsible for the changes in the dielectric and optical properties which produced the localized states in the optical band gap.

(2) The AgNPs embedded into the SiO_2 surface enables the excitation of the localized surface plasmon resonance (SPR). Furthermore, UV-Vis results reveal that the light absorption from the coupling of photonic and plasmonic modes can be modified using the specific filling fraction between the AgNPs and the dielectric medium.

(3) The XRD results show that the optimum filling fraction of the AgNPs/SiO_2 is 0.6. At the lower filling fraction, the presence of AgNPs is almost undetected as shown in the SPR absorption spectrum. Therefore, an optimum filling fraction of 0.6 possesses the desired optical property of the nanocomposite.

(4) Thermal analysis using DSC on the highest conducting samples revealed that the melting point of Ag-SiO_2 NC was around 50 °C – 140 °C. T_m and T_g decreased gradually due to the presence of the AgNPs embedded within the SiO_2

nanostructure. This phenomenon was due to the enhancement of volume fraction of the crystalline state of AgNPs and silica amorphous phase, thus enhanced the nanocomposite stability.

(5) The SiO_2 nanoparticles used in the synthesis showed excellent dispersion properties, due to the chemical inertness towards the AgNPs and is optically transparent as characterized by FTIR spectroscopy, thus can be used to modulate the intensity of the AgNPs surface plasmon absorption bands.

(6) The effective permittivity of the Ag-SiO_2 NC from the ES results is consistent with the Maxwell Garnett model at the optimum filling fraction. However, strong dispersions were observed at higher filling fractions. The effective permittivity and refractive index obtained from this filling fraction are -0.88 and 0.90, respectively shows metamaterial properties is obtained.

(7) From the results of PEC studies, Ag-SiO_2 NC has a good electronic properties, photochemically stable, responsive to solar-irradiation, having the oxidation and reduction potential, exhibit a great response for hydrogen generation. Among all samples, Ag60 has the advantage of a band-gap 2.03 eV and with the highest photocurrent density of 1.28 mA/cm^2 at bias potential of 0.92 eV for photoelectrochemical response and photoconversion efficiency.

6.2 Suggestions for Future Work

The results shown in this research have created a path towards a low temperature, cost-effective and non-toxic technique the synthesis of Ag-SiO_2 NC at an optimum filling fraction with a great potential in PEC water splitting. For future research,a few suggestions for further studies:

(1) It may be possible to synthesized the optimum composition of Ag-SiO_2 using other method at high temperature such as Polymer Pyrolisis Sol Gel for highly stable nanostructure.

(2) The success in the synthesis of optimum filling fraction at 0.6 (sample Ag60) can be extended by the incorporation of other metal-oxide such as Cuprous oxide (Cu_2O) for SERS applications and to improve the photocatalytic activities during illuminations under UV.

(3) Since the PEC studies on Ag-SiO_2 NC is only preliminary, further studies are required to improve the stability of the thin films. The evaluation of the stability of the films is suggested taking into account the reusability/recyclability of the of the thin films during PEC process.

REFERENCES

Alfaifi, B. Y., Ullah, H., Alfaifi, S., Tahir, A. A., Mallick, T. K. (2018) Photoelectrochemical solar water splitting: From basic principles to advanced devices. Veruscript Functional Nanomaterials. 2.

Amroziak, R., Holdynski, M., Plocinski, T., Pisarek, M., Kudelski, A. (2019). Cubic silver nanoparticles fixed on TiO2 nanotubes as simple and efficient substrates for surface enhanced Raman scattering. *Materials,* 12 (20) 337.

Acosta, S., Corriu, R., Leclercq, D., Mutin,P.H., Vioux, A. (1994). Novel Non-Hydrolytic Sol-Gel Route to Metal Oxides. *Journal of Sol-Gel Science and Technology*, *2*, 25-28.

Acosta-Silva, Y. J., Nava, R., Hern´andez-Morales, V., Mac´ıas-S´anchez, S. A., G´omez-Herrera, M. L., Pawelec, B.(2011). Methylene blue photodegradation over titania-decorated SBA-15. *Appl. Catal*., B, *110*, 108–117.

Alu, A., Salandrino, A., Engheta, N. (2006). Negative effective permeability and left-handed materials at optical frequencies. *Optical Society of America*.

Amendola, V., Meneghetti, M. (2009) Laser ablation synthesis in solution and size manipulation of noble metal nanoparticles. *Phys. Chem. Chem. Phys*. *11*, 3805–3821.

An, H. H., Kim, Y., Han, W. B., Kim, H-S., Lee, S., Yi, S. C., Kim, D-H., Yoon, C. S.(2013). Surface-enhanced Raman scattering substrate based on silvernanoparticle-deposited phospholipid multilayer. *Applied Surface Science 287*, 369– 374.

Awazu, K., Fujimaki, M., Rockstuhl, C., Tominaga, J., Murakami, H., Ohki, Y., Yoshida, N., Watanabe, T.(2008). A Plasmonic Photocatalyst Consisting of Silver Nanoparticles Embedded in Titanium Dioxide. *Journal of the American Chemical Society, 130*, 1676–1680. Solar Hydrogen Generation 273.

Awwad, A. M., Salem, N. M., Abdeen, A. O. (2012). Biosynthesis of Silver Nanoparticles using Olea europaea Leaves Extract and its Antibacterial Activity. *Nanoscience and Nanotechnology*, *2* (6) 164-170.

Azulai, D., Belenkova , T., Gilon , H., Barkay, Z., Markovich, G. (2009). Transparent Metal Nanowire Thin Films Prepared in Mesostructured Templates. *Nano Lett*. *9* (2009) 4246-4249.

Babapour, A., Akhavan, O., Azimirad, R., & Z Moshfegh, A. (2006). Physical characteristics of heat-treated nano-silvers dispersed in sol-gel silica matrix. *Nanotechnology*, *17*, 763-771.

Bahadur, N.M., Watanabe, S., Furusawa. T., Sato, M., Kurayama, F., Siddiquey, I.Y., Kobayashi, Y., Suzuki, N., Rapidone. (2011). Characterization and Functionalization of Silica coated Gold Nanoparticles, *Colloids Surf. A, 392,* 137-144.

Bandi, S., Schiraldi, D.A.(2006). Glass Transition Behavior of Clay Aerogel/Poly(vinyl alcohol) Composite. *Macromolecules, 39* (19) 6537–6545.

Barnes, W. L. (2006). Surface plasmon–polariton length scales: a route to sub-wavelength optics. *J. Opt. A: Pure Appl. Opt.***,** *8,* S87–S93.

Barnes, W. L., Dereux, A. & Ebbesen, T. W. (2003). Surface plasmon subwavelength optics. *Nature.* 424, 824–830.

Barnickel, P., Wokaun, A. (1990). Synthesis of metal colloids in inverse microemulsions.

Baset, S., Akbari, H., Zeynali, H., and Shafie, M. (2011). Size measurement of metal and semiconductor nanoparticles via UV–Vis absorption spectra. *Dig. J. Nanomater. Bios. 6*, 709–716.

Belyaev, B.A., Tyurnev, V.V. (2018). Electrodynamic Calculation of Effective Electromagnetic Parameters of a Dielectric Medium with Metallic Nanoparticles of a Given Size. *J. Exp. Theory Phys. 127***,** 608–619.

Behara, D. K., Sharma, G. P., Upadhyay, A. P., Gyanprakash, M., S Pala, R. G., Sivakumar, S. (2016). Synchronization of charge carrier separation by tailoring the interface of Si–Au–TiO 2 heterostructures via click chemistry for PEC water splitting. *Chemical Engineering Science. 154* (150-169).

Bigot, J.-Y., Halte´, V., Merle, J.-C., Daunois, A.(2000). Electron dynamics in metallic nanoparticles. *Chemical Physics*, 251, 181–203.

Blanchard, J., In, M., Schaudel, B., Sanchez. C. (1998). Hydrolisis and Condensation Reactions of Transition Metal Alkoxides. *Eur. J. Inorg. Chem.* 111521127.

Bohren, C.F., Huffman, D.R. (1983) *Absorption and Scattering by Small Particles*. Wiley, New York.

Bresme, F., Quirke, N. (1998).Computer Simulation Study of the Wetting Behavior and Line Tensions of Nanometer Size Particulates at a Liquid-Vapor. *Interface. Interface. Phys. Rev. Lett*. *80*, 3791-3794.

Brinker, C. J., & Schere, G. W., (1990). Sol-Gel Science:The Physics and Chemistry of Sol-Gel Processing, *Academic Press*, New York.

Budhiraja, N., Sharma, A., Dahiya, S., Parmar, R., Vidyadharan, V.(2013). Synthesis and optical characteristics of silver nanoparticles on different substrates. *International Letters of Chemistry, Physics and Astronomy, 19, 80-88.*

Racles, C., Nistor, A.,Cazacu. M.(2013). A silica-silver nanocomposite obtained by sol-gel method in the presence of silver nanoparticles, *Cent. Eur. J. Chem., 11,* 1689-1698.

Capolino, F. (2010). Theory and Phenomena of Metamaterials. *CRC Press*: Boca Raton, FL, USA.

Cassagneau, T., Caruso, F. (2002). Contiguous silver nanoparticle coatings on dielectric spheres, *Adv. Mater. 14*, 732–736.

Catauro, M., Tranquillo, E., Poggetto, G.D., Pasquali, M., 'Era, A. D., S. Ciprioti, V. (2018). Influence of the Heat Treatment on the particle size and on the crystalline Phase of TiO_2 Synthesized by the Sol-Gel Method. *Materials, 11*, 2364.

Ceccato, R., Dire, S., Lutterotti, L. (2003). Pyrolysis pathway of sol–gel derived organic/inorganic hybrid nanocomposites. *Journal of Non-Crystalline Solids,* 322 (1-3)22–28.

Cai, W., Zhang, Y., Jia, J., Zhang, L. (1998). Semiconducting optical properties of silver/silica mesoporous composite. *Appl. Phys. Lett*. *73***,** 2709–2715.

Cha, H., Lee, D., Yoon, J. H., Yoon, S. (2016). Plasmon coupling between silver nanoparticles: Transition from the classical to the quantum regime. *Journal of Colloid and Interface Scien*ce. *464,* 18-24.

Chaumet, P., Dufour, J. (1998). Electric potential and field between two different spheres. J. Electrostat. *43*, 145-159.

Che Lah, N.A., Johan, M. R. (2011). Facile shape control synthesis and optical properties of silver nanoparticles stabilized by Daxad 19 surfactant. *App. Surface Sci.* 257, 7494 – 7500.

Cheng, C., Jiang, Y., Sun, X., Shen, J., Wang, T., Fan, G., Fan, R. (2020). Tunable negative permittivity behavior and electromagnetic shielding performance of silver/silicon nitride metacomposites, *Composites Part A 130,* 105753.

Chen, H., You, T., Jiang, L., Gaoa, Y., Yin. P. (2017). Creating dynamic SERS hotspots on the surface of pH-responsive microgels for direct detection of crystal violet in solution. RSC Adv. *7*, 32743.

Chen, W-F., Mofarah, S. S., Hanaor, D. A. H., Koshy, P., Chen, H-K., Jiang, Y., Sorrell, C. C. (2018). Enhancement of Ce/Cr Codopant Solubility and Chemical Homogeneity in TiO_2 Nanoparticles through Sol–Gel versus Pechini Syntheses. *Inorg. Chem. 57* (12) 7279–7289.

Chen, X., Zheng, Z., Ke, X., Jaatinen, E., Xie, T., Wang, D., Guo, C., Zhao, J., Zhu, H. (2010). Supported silver nanoparticles as photocatalysts under ultraviolet and visible light irradiation. *Green Chem. 12,* 414–419.

Choma, J., Jamiola, D., Ludwinowicz, J., Jaroniec, M. (2012). Deposition of silver nanoparticles on silica spheres and rods. *Colloids Surf.A 411*, 74–79.

Chou, K-S., Ren, C-Y.(2000). Synthesis of nanosized silver particles by chemical reduction method. *Materials Chemistry and Physics, 64*, 241-6.

Crooker, S.A., Barrick, T., Hollingsworth, J.A. (2003) Multiple temperature regimes of radiative decay in CdSe nanocrystal quantum dots: intrinsic limits to the darkexciton lifetime, *Appl. Phys. Lett*. *82*, 2793–2796.

Cuenya, B.R. (2010). Synthesis and catalytic properties of metal nanoparticles: Size, shape, support, composition, and oxidation state effects. *Thin Solid Films*, *518*, 3127–3150.

Das, S. K., Khan, M. M. R., Parandhaman, T., Laffir, F., Guha, A. K., Sekaran, G., Mandal, A. B. (2013). Nano-silica fabricated with silver nanoparticles: antifouling adsorbent for efficient dye removal, effective water disinfection and biofouling control. *Nanoscale*, *5*, 5549-5560.

De, S., Higgins, T.M., Lyons P.E., Doherty E.M., Nirmalraj P.N., Blau W.J., Boland J.J., Coleman J.N. (2009). Silver Nanowire Networks as Flexible, Transparent, Conducting Films; Extremely High DC to Optical Conductivity Ratios. *Acs Nano. 3* (7) 1767-1774.

Del P. Rodríguez-Torres, M.; Díaz-Torres, L.A.; Romero-Servin, S. (2014). Heparin Assisted Photochemical Synthesis of Gold Nanoparticles and Their Performance as SERS Substrates. *Int. J. Mol. Sci*., *15*, 19239-19252

Dimitriev, Y., Ivanova, Y., Iordanova, R. (2008) History of sol-gel science and technology (review), *Journal of the University of Chemical Technology and Metallurgy, 43*, 2, 181-192.

Ding, J., Qin, Z. Luo, H. Yang, W. Wang, Y. Huang, Z. (2020) Nano-silica modified phenolic resin film: manufacturing and properties, *Nanotechnol Rev.* 9 (1)209–218.

Ditlbacher, H., Hohenau, A., Wagner, D., Kreibig, U., Rogers, M., Hofer, F., Aussenegg, F.R., Krenn, J.R. (2005). *Phys. Rev. Lett. 95*, 257403.

Duhan, S., Devi, S., Srivastava, M. (2010). Characterization of nanocrystalline Ag/SiO_2 nanocomposites and synthesis by wet chemical method, *Indian J. Pure Appl.Phys., 48,* 271–275.

Dutta, S., Ghosh, A., Kabir, H., Saha, R. (2016). Facile one pot synthesis of zinc oxide nanorods and statistical evaluation for photocatalytic degradation of a diazo dye. *Water Science & Technology, 74* (3) 698-713.

Ebert, K., Fritsch, D., Koll, J., Tjahjawiguna, C. (2004). Influence of inorganic fillers on the compaction behaviour of porous polymer based membranes. *J. Membr. Sci*. *233*, 71–78.

Eklund SE, Cliffel DE. (2004). Synthesis and catalytic properties of soluble platinum nanoparticles protected by a thiol monolayer. *Langmuir, 20*, 6012–6018.

Engheta, N., Zuilkowski, R.W. (2006). Metamaterials : Physics and Engineering Explorations. *John Wiley & Sons*.

Eremenko, A.M., Smirnova, N. P., Mukha, I.P., Yashan, H.R. (2010). Silver and Gold Nanoparticles in Silica Matrices: Synthesis, Properties and Application. *Theoritical and Experimental Chemistry, 46* (2) 65-88.

Etrich, C., Fahr, S., Hedayati, M. K., Faupel, F., Elbahri, M., Rockstuhl, C. (2014). Effective Optical Properties of Plasmonic Nanocomposites. *Materials, 7*, 727-741.

Evanoff, D.D., Chumanov, G. (2005). Synthesis and Optical Properties of SilverNanoparticles and Arrays. *ChemPhysChem*. *6*, 1221 – 1231.

Faraudo, J., Bresme, F. J. *Chem. Phys. 118* (2003), 6518.

Flores, J.C., Torres, V., Popa, M., Crespo, D., Calderon-Moreno, J.M.(2008). Preparation of core-shell nanospheres of silica-silver: SiO_2@Ag. *J. Non-Cryst. Solids*. *354* (52-54) 5435–5439.

Gao X, Nie S. (2004). Quantum dot-encoded mesoporous beads with high brightness and uniformity rapid readout using flow cytometry. *Anal Chem. 76*, 2406–2410.

Graf, C., von Blaaderen, A., (2002). Metallodielectric colloidal core-shell particles for photonic applications. *Langmuir, 18*, 524–534.

Grimes, C. A., Varghese, O. K., & Ranjan, S. (2007). *Light, water, hydrogen: the solar generation of hydrogen by water photoelectrolysis*: Springer Science & Business Media.

Gric, T. (2016). Surface-Plasmon-Polaritons at the Interface of Nanostructured Metamaterials. *Progress In Electromagnetics Research M, Vol. 46, 165–172.*

Guitoume, D., Achour, S.,Sobti, N., Boudissa, M., Souami, N., Messaoudi, Y. (2018). Structural, optical and photoelectrochemical properties of TiO_2 films decorated with plasmonic silver nanoparticles. *Optik, 154,* 182-191.

Guo, J.-F., Ma, B., Yin, A., Fan, K., Dai, W.-L. (2011). Photodegradation of rhodamine B and 4-chlorophenol using plasmonic photocatalyst of Ag-Agl/Fe_3O_4@SiO_2 magnetic nanoparticle under visible light irradiation. Appl. Catal. B. *101*, 580-586.

Guo, Q., Zhao, Y., Wang, Z., Skrabalak, S.E., Lin, Z., Xia, Y. (2008). Size Dependence of Cubic to Trigonal Structural Distortion in Silver Micro-and Nanocrystals under High Pressure. *J. Phys. Chem C*. *112* (51) 20135-20137.

Gurav, A. S., Kodas,T. T., Wang, L. M., Kauppinen, E. I., Joutsensaari, J. (1994). Generation of nanometer-size fullerene particles via vapor condensation. *Chem. Phys. Lett*. *218*, 304-308.

Hartland, G.V., Besteiro,L., Johns, P., Govorov, A.O. (2017). What's so hot about electrons in metal nanoparticles. *ACS Energy Lett. 2 (7)* , 1641–1653.

Herrera, G.M., Padilla, A.C., Hernandez-Rivera, S.P. (2013) Surface Enhanced Raman Scattering (SERS) studies of gold and silver nanoparticles prepared by laser ablation, *Nanomaterials, 3*,158–172.

Henglein, A. (1993). Physicochemical Properties of Small Metal Particles in Solution: "Microelectrode" Reactions, Chemisorption, Composite Metal Particles, and the Atom-to-Metal Transition. *Journal of Physical Chemistry. 97*, 5457-5471.

Hilonga, A., Kim, J.K., Sarawade, P.B., Kim, H.T. (2009). Reinforced silver-embedded silica matrix from the cheap silica source for the controlled release of silver ions. *Applied Surface Science*. 255, 8239–8245.

Hirai, T., Sato, H., Komasawa, I. (1999). Preparation of semiconductor nanoparticlepolyurea composites using reverse micellar systems via an in situ diisocyanate polymerization. *J Phys. Chem. B. 103*, 10120–10126.

Hong-Mei, G., Li, Z., Xiong-Rui, S., Si, X., Shao-Ding, L., Qu-Quan, W. (2009). Illuminating Dark Plasmons of Silver Nanoantenna Rings to Enhance Exciton-Plasmon Interactions. *Advance Functional Materials, 19*. (2) 298-303.

Hong, Y., Huh, Y-M., Yoon, D.S., Yang, J. (2012). Nanobiosensors Based on Localized Surface Plasmon Resonance for Biomarker Detection. *Journal of Nanomaterials, 13*, 759830.

Hornyak, G. L., Dutta, J., Tibbals, H. F., Rao., A. K. (2008). Introduction to Nanoscience. *CRC Press, Taylor and Francis Group*, Boca Raton, US.

Huang, H., Yang, Y. (2008). Preparation of silver nanoparticles in inorganic clay suspensions. *Compos. Sci. Technol*. *68*, 2948-2953.

Hu, M., Yan, X., Hu, X., Feng, R., Zhou, M. (2018). Synthesis of silver decorated silica nanoparticles with rough surfaces as adsorbent and catalyst for methylene blue removal. *J Solgel Sci. Technol*. *89*, 754-763.

Iacona, F., Franzo`, G., Spinella, C. (2000). Correlation between luminescence and structural properties of Si nanocrystals. *J. Appl. Phys. 87,* 1295.

Ibrahim, W.A.W., Ismail, W.N.W., Keyon, A.S.A., Sanagi, M.M. (2011). Preparation and characterization of a new sol-gel hybrid based tetraethoxysilane-polydimethylsiloxane as a stir bar extraction sorbent materials, *J Sol-Gel Sci Technol. 58* , 602-611.

Ingram D., Linic, S. (2011). Water Splitting on Composite Plasmonic-Metal/Semiconductor Photoelectrodes: Evidence for Selective Plasmon-Induced Formation of Charge Carriers near the Semiconductor Surface. *Journal of the American Chemical Society, 133*, 5202–5205.

Ishimaru, A., Jaruwatanadilok, S., & Kuga, Y. (2005). Generalized Surface Plasmon Resonance Sensors Using Metamaterials and Negative Index Materials. *Progress in Electromagnetics Research, PIER. 51*, 139-152.

Izaak, T. I., Martynova, D. O., Stonkus, O. A., Slavinskaya, E. M., Boronin, A. I. (2013). Deposition of silver nanoparticles into porous system of sol–gel silica monoliths and properties of silver/porous silica composites. *J Sol-Gel Sci Technol*. *68* (3) 471–478.

Jain, P. K., Huang, W., El-Sayed, M. A. (2007). On the Universal Scaling Behaviour of the Distance Decay of Plasmon Coupling in Metal Nanoparticle Pairs : A Plasmon Ruler Equation. *Nano Lett.7*, 2080–2088.

Jasiorski, M., Łuszczyk, K., Baszczuk, A. (2014). Morphology and absorption properties control of silver nanoparticles deposited on two types of sol–gel spherical silica substrates. *Journal of Alloys and Compounds,* 588, 70–74.

Jasiorski, M., Skoczylas, A., Hermanowicz, K., Haimann, K., Strezk, W., Maruszewski, K. (2004). Surface-enhanced Raman spectra of substances adsorbed on Ag0 clusters deposited on SiO_2 submicron spheres prepared by the sol–gel method. *Optical Materials. 26*, 145–149.

Jepsen, P.U., Fischer, B.M., Thoman, A., Helm, H., Suh, J.Y., Lopez, R., Haglund, R.F. (2006). Metal-insulator phase transition in a VO_2 thin film observed with tetrahertz spectroscopy. *Phys. Rev. B. 74* (20) 205103-205112.

Jiang, J., Cao, J.,Wang, W. Mei, C. (2018). Analysis on the Influence of Component Ratio on Properties of Silica/Montmorillonite Nanocomposites. *Materials* , *11* (11) 2074-2086.

Jiun-Jen, C., Jeffrey, C.S.W. , Pin Chieh, W., Din Ping, T. (2011). Plasmonic Photocatalyst for H_2 Evolution in Photocatalytic Water Splitting. *J. Phys. Chem. C. 115* (1) 210–216.

Jiwei, Z., B. S. X. Y. L. Z. (2002). Preparation and spectral properties of Nd_2O_3-doped silica-based glasses prepared by the sol-gel process. *Ceramics International, 28* (7), 737-740.

Jiwei, Z., Xi, Y., Xiaogang, C., Liangying, Z., Chen, H. (2002). Direct-current field dependance of dielectric properties in B_2O_3- SiO_2 glass doped $Ba_{0.6}$ $Sr_{0.4}$ TiO_3 ceramics. *J. Mater. Sci*. *37*, 3739–3745.

Johnson, R. L. (2005). Characterization of Piezoelectric ZnO Thin Films and the Fabrication of Piezoelectric Micro-Cantilevers. *Masters Thesis*, Iowa State University, Ames Iowa.

Juarez, H., Pacio, M., Diaz, T., Rosendo, E., Garcia, G., Garcia, A., Mora, F., Escalante, G.(2009). Low temperature deposition: properties of SiO_2 films from TEOS and ozone by APCVD system. Journal of Physics : Conference Series 167, 012020.

S. J. Kelly, X. Wen, D. P. Arnold, J.S. Andrew, "Electrophoretic deposition of nickel zinc ferrite nanoparticles into microstructured patterns," *AIP ADVANCES. 6* (2016) 056105.

Kabashin, A. V., Evans, P., Pastkovsky, S., Hendren, W., Wurtz, G.A., Atkinson, R., Pollard, R., Podolskiy, V.A., Zayats, A.V. (2009). Plasmonic nanorod metamaterials for biosensing. *Nature Materials, 8*, 867–871.

Kalele, S.A., Ashataputre, S.S., Hebalkar, N.Y., Gosavi, S.W., Deobagkar, D.N., Deobagkar, D.D., Kulkarni, S.K. (2005). Optical detection of antibody using silica-silver core-shell particles. *Chem.Phys.Lett. 404*, 136-141.

Kamegawa, T., Yamahana D., Yamashita, H. (2010). Graphene Coating of TiO_2 Nanoparticles Loaded on Mesoporous Silica for Enhancement of Photocatalytic Activity. *J. Phys. Chem. C. 114* (35)15049–15053.

Kang, D. K. L., Y. S. (2004). Synthesis of Silver Nanocrystallites by a New Thermal Decomposition Method and Their Characterization. *ETRI Journal, 26* (3), 252-256.

Kawashita, M., Toda, H.M., Kim, T., Kokubo, N., Masuda, J. (2003). Preparation of antibacterial silver-doped silica glass microspheres. *Biomed. Mater. Res. A. 66,* 266–274.

Kazuma, E., Tatsuma, T. (2012). Photoinduced reversible changes in morphology of plasmonic Ag nanorods on TiO_2 and application to versatile photochromism. *Chem. Commun. 48,* 1733–1735.

Kelly, S.J., Wen, X. Arnold, D.P., Andrew, J.S. (2016). Electrophoretic deposition of nickel zinc ferrite nanoparticles into microstructured patterns. AIP Advances, *6*, 056105.

Khan, A.S., Khalid, H., Sarfraz, Z., Khan, M., Iqbal, J., Muhammad, N., Fareed, M.A., Rehman, I. U. (2016). Vibrational spectroscopy of selective dental restorative materials. *Appl. Spectrosc. Rev. 52,* 507–540.

Kim, K.S., Kim, J.K., Kim, W.S. (2002). "Influence of Reaction Conditions on Sol-Precipitation Process Producing Silicon Oxide Particles. *Ceramics International*, *28*, 187-194.

Kielbasa, J. E., Liu, J., Ucer, K. B., Carroll, D. L., Williams R. T. (2007). Sol-gel nanocomposites as metamaterials: preparation and optical measurements. *J Mater Sci: Mater Electron. 18,* S435–S438.

Kim, F., Kwan, S., Akana, J., Yang P. (2001). Langmuir-Blodgett Nanorod Assembly. *J. Am. Chem. Soc. 123* (18) 4360-4361.

Kim, K., Yoon, J.K., Lee, H.B., Shin, D., Shin, K.S. (2011). Surface Enhanced Raman scattering of 4-Aminobenzenethiol in Ag sol: relative intensity of a1 and b2 – type bands invariant against aggregation of Ag nanoparticles. *Langmuir 27*, 4526–4531.

Kim, K., Shin, D., Choi, J-Y., Kim, K.L., Shin, K.S. (2011). Surface Enhanced Raman scattering characteristics of 4-Aminobenzenethiol derivatives adsorbed on silver. *J. Phys. Chem. C. 115*, 24960–24966.

Kim, K., Kim, K.L., Shin, D., Choi, J-Y., Shin, K.S. (2012). Surface Enhanced Raman Scattering of 4-Aminobenzenethiol on Ag and Au: pH dependence of b2-type bands. *J. Phys. Chem. C 116*, 4774–4779.

Kim, T. G., Kim, J.M., Jang, K-S., Lee, S.J. (2021). Dispersibility tailored conductive epoxy nanocomposites with silica nanoparticle-embedded silver nanowire. *Polymer Testing* 96, 107111.

Kobayashi, Y., Salgueirino-Maceira, V., Liz-Marzan, L.M. (2001). Deposition of silver nanoparticles on silica spheres by pretreatment steps in electroless plating, *Chem. Mater.* 13, 1630–1633.

Kruis, F., Fissan, H., Rellinghaus, B. (2000). Sintering and evaporation characteristics of gas-phase synthesis of sizeselected PbS nanoparticles. *Mater. Sci. Eng. B*. 69-70, 329-334.

Kumar, V., Wang, H. (2013).Plasmonic Au nanoparticles for enhanced broadband light absorption in inverted organic photovoltaic devices by plasma assisted physical vapour deposition. *Org. Electron. 14* (2) 560–568.

Kumar, K.V.A., John, J., Sooraj, T.R., Raj, S.A., Unnikrishnan, N.V., Selvaraj, N. B. (2019). Surface plasmon response of silver nanoparticles doped silica synthesised via sol-gel route. *Applied Surface Science 472*, 40–45.

Landau, L., Lifschitz, E. M. (1984). Electrodynamics of continuous media. Elsevier.

Lee, C.H., Yu, J., Wang, Y., Tang, A.Y.L., Kan, C.W., Xin, J.H. (2018). Effect of graphene oxide inclusion on the optical reflection of a silica photonic crystal film. *RSC Adv. 8,* 16593–16602.

Lee, J. Y., Connor, S. T., Cui, Y., Peumans, P. (2010). Semitransparent Organic Photovoltaic Cells with Laminated Top Electrode. *Nano Lett. 10* (4) 1276-1279.

Le Gue´vel, X., Ho¨tzer, B., Jung, G., Hollemeyer, K., Trouillet, V., Schneider, M. (2011). Formation of fluorescent metal (Au, Ag) nanoclusters capped in bovine serum albumin followed by fluorescence and spectroscopy. *J Phys Chem C. 115*, 10955–10963.

Li, C.-H., Jamison, A.C., Rittikulsittichai, S., Lee, T.-C., Lee, T. R. (2014). In Situ Growth of Hollow Gold−Silver Nanoshells within Porous Silica Offers Tunable Plasmonic Extinctions and Enhanced Colloidal Stability. *ACS Appl. Mater. Interfaces*, 6, 19943−19950.

Li, H., Li, Y., Li M., Xu, L., Li, J. (2019). Facile and ultrasensitive electrochemical impedance sensing for formaldehyde based on silver ions doped in controllable and homogeneous silica microspheres. *Sensors & Actuators :B. Chemical, 284*, 657-662.

Lin, C. H., Chang, C. H., Jao, W. C., Yang, M. C. (2009). Organic–inorganic hybrid membranes prepared from the sol–gel process of poly(butyleneadipate-co-terephthalate) and TiO_2. *Polym. Adv. Technol*. 20, 672–679.

Liu, H., Bai, J., Wang, S., Li, C., Guo, L., Liang, H., Xu, T., Sun, W., Li, H. (2014). The preparation of silver nanoparticles/carbon nanofibers as catalyst in the styrene epoxidation. *Colloids and Surfaces A: Physicochem. Eng. Aspects*. *448*, 154–159. doi.10.1016/j.colsurfa.2014.02.024.

Liu, T., Li, D., Yang, D., Jiang, M. (2011). An improved seed-mediated growth method to coat complete silver shells onto silica spheres for surface- enhanced Raman scattering, *Colloids Surf. A 387*, 17–22.

Liu, Y., Bartal, G., Zhang, X. (2008). All-angle negative refraction and imaging in a bulk medium made of metallic nanowires in the visible region. *Optics Express*, *16,* 15439-15448.

Livage, J., Henry, M., Sanchez, C. (1988). Sol-gel chemistry of transition metal oxides. *Prog. Solid State Chem. 18* (4) 259-341.

Liz-Marzan, L.M. (2006). Tailoring surface plasmons through the morphology and assembly of metal nanoparticles. *Langmuir, 22*, 32–41.

Liz-Marzan, L.M., Giersig, M., Mulvaney, P.(1996). Synthesis of nanosized gold–silica core–shell particles. *Langmuir*, 12, 4329–4335.

Lu , Y. C., Chou, K. S. (2010). Tailoring of silver wires and their performance as transparent conducive coatings. *Nanotechnology 21* (21) 215707.

Lu, Y., Yin, Y., Li, Z., Xia, Y. (2002). Synthesis and self-assembly of Au–SiO2 core–shell colloids. *Nano Lett. 2*, 785–788.

Luo, C., Zhang, Y., Zeng, X., Zeng, Wang, Y.Y. (2005). The role of poly(ethylene glycol) in the formation of silver nanoparticles, *J. Colloid Interface Sci, 288*, 444-456.

M. Kuttge, M., Vesseur, E., Koenderink, A., Lezec, H., Atwater, H., Garcia De Abajo, F., Polman. (2009). Local Density of states, spectrum, and far-field interference of surface plasmon polaritons probed by cathodoluminescence. *Physic Review B*, *79*,113405.

Magnusson, M. H., Deppert, K., Malm, J. O., Bovin,J. O., Samuelson, L. (1999). Gold nanoparticles: Production, reshaping, and thermal charging. *J. Nanoparticle Res*. *1*, 243-251.

Mahmudin, L., Suharyadi, E., Utomo,A. B. S., Abraha, K. (2015). Optical Properties of Silver Nanoparticles for Surface Plasmon Resonance (SPR)-Based Biosensor Applications. *Journal of Modern Physics*, *6* (8) 1071-1076.

Maier, S. A. (2007). *Plasmonics: Fundamentals and Applications*: Springer

Markel, V.A., Muratov, L.S., Stockman, M.I., George, T.F. (1991). Theory and numerical simulation of optical properties of fractal clusters. *Phys. Rev. B*, *43*, 8183–8195.

Markel, V.A., Shalaev, V., Stechel, E.B., Kim, W., Armstrong, R.L. (1996). Small-particle composites. I. Linear optical properties. *Phys. Rev. B*, *53*, 2425–2436.

Martinez-Castanon, Gabriel-Alejandro., Martinez, J.R., Ortega-Zarzosa, G., Ruiz, Facundo., Sanchez-Loredo, M.(2005). Optical Absorption of Ag Particles Dispersed in a SiO_2 Amorphous Matrix. Journal of Sol-Gel Science and Technology, 36, 137-145.

Marton, J.P., Lemon, J.R. (1971). Optical Properties of Aggregated Metal Systems. *Phys. Rev*. B 4, 271–280.

Matter, F., Luna, A. L., Niederberger, M. (2020). From colloidal dispersions to aerogels: How to master nanoparticle gelation. *Nano Today*, *30*,100827.

Mauro R. Sardela Jr. (2014). *X-Ray Diffraction and Reflectivity.* Springer Link. 1-41.

McFarland AD, Duyne RPV. (2003). Single silver nanoparticles as real-time optical sensors with zeptomole sensitivity. *Nano Lett*. 3,1057–1062.

Merlin, R. (2009) Metamaterials and the Landau-Lifshitz permeability argument: large permittivity begets high-frequency magnetism. *Proc. National. Acad. Sci*. *106*, 1693–1698.

Mishra, Y. K., Mohapatra, S., Chakravadhanula, V. S. K., Lalla, N. P., Zaporojtchenko, V., Avasthi, D. K., Faupel., F. (2010). Synthesis and Characterization of Ag-Polymer Nanocomposites. *Nanoscience and Nanotechnology*, 10, 2833–2837.

Mock, J.J., Barbic, M., Smith, D.R. (2002). Silver nanodisks: synthesis, characterization, and self-assembly. *J. Chem. Phys. 116*, 6755–6758.

Mohan, V.M., Raja, V., Bhargav, P.B., Sharma, A.K., & NarasimhaRao, V.V.R. (2007). Structural, electrical and optical properties of pure and $NaLaF_4$ doped PEO polymer electrolyte films. *Journal of Polymer Resource*, *14,* 283-290

Moiseev, S.G. (2010). Active Maxwell-Garnett composite with the unit refractive index. *Physica B 405*, 3042.

Moiseev, S. G.(2011). Composite medium with silver nanoparticles as an anti-reflection optical coating. *Appl Phys A 103***,** 619–622.

Mokari, T., Sztrum, C.G., Salant, A., Rabani, E., Banin, U. (2005). Formation of asymmetric one-sided metal-tipped semiconductor nanocrystal dots and rods. *Nature Materials, 4*, 855–863.

Mokkapati, S., Beck, F.J., Polman, A., Catchpole, K.R. (2009). Designing periodic arrays of metal nanoparticles for light-trapping applications in solar cells, *Appl. Phys. Lett. 95*, 053115–053119.

Moskovits M. (2005). Surface-enhanced Raman spectroscopy: a brief retrospective. *J Raman Spectrosc. 36* (6–7), 485–496.

Muniz-Miranda, M.(2003). Silver-doped silica colloidal nanoparticles.:Characterization and optical measurements. *Colloids and Surfaces A: Physicochem. Eng. Aspects*, *217*,185-189.

Natsuki, J., Natsuki, T., Hashimoto, Y.(2015). A Review of Silver Nanoparticles: Synthesis Methods, Properties and Applications. *International Journal of Materials Science and Applications, 4* (5) 325-332.

Nguyen, T. K. L., Nguyen, T. A. T., Dang,V. P., Nguyen, N. D., Le, A. Q., Nguyen, Q. H. (2013). Synthesis of silver nanoparticles deposited on silica by γ-irradiation and preparation of PE/Ag nano compound masterbatches. *Adv. Nat. Sci. Nanosci. Nanotechnol. 4* (4) 045004.

Niitsoo, O., Couzis, A. (2011). Facile synthesis of silver core-silica shell composite nanoparticles. *J. Colloid Interface Sci. 354*, 887-890.

Nishio, K., Tsuchiya, T. (2004). Chapter 3 Sol–Gel Processing of Thin Films with Metal Salts. In Sakka, JSumio (ed.). Handbook of Sol-Gel Science and Technology, Processing Characterisation and Applications. Kluwer Academic, 59–66.

Orgaz-Orgaz, F. (1988). Gel to glass conversion: Densification kinetics and controlling mechanisms. *J. Non-Cryst. Solids, 100* (1-3)115–141.

Orgaz, F. R. H., (1986). Coloured coatings prepared by the sol-gel process. *Journal of Non-Crystalline Solids,* 82(1-3),378-390.

Owen, T. (1996). Fundamentals of UV-visible Spectroscopy. Germany: Hewlett-Packard

Pal, A.K., Hussain, S., Roy, R.K. (2006). Incorporation of silver nanoparticles in DLC matrix and surface plasmon resonance effect. *Chem.Phys. 99*, 375-379.

Paramasivam, I., Macak, J.M., Schmuki, P. (2008). Photocatalytic Activity of TiO_2 Nanotube Layers Loaded with Ag and Au Nanoparticles. *Electrochemistry Communications, 10*, 71–75.

Paulose, M., Mor, G.K., Varghese, O.K., Shankar, K., Grimes, C.A. (2006). Visible light photoelectrochemical and water-photoelectrolysis properties of titania nanotube arrays. *J. Photochem. Photobiol. A,* 178 (2006) 8–15.

Pei , L., Xiang , W., Zhao , X., Liang , X., Yang , X., Liu , H., Chen , Z., Xie , C., Ma, X., Zhang , C., Ma, L., Zhao. J. (2014) Sol–gel synthesis of silver nanocrystals embedded in sodium borosilicate monolithic transparent glass with giant third-order optical nonlinearities. *Materials Research Bulletin*, *59*,154–161.

Pei, Y., Yao, F., Ni P., Sun, X. (2010). Refractive index of silver nanoparticles dispersed in polyvinyl pyrrolidone nanocomposite. *Journal of Modern Optics, 57*(10) 872–875.

Pesika, N.S., Stebe, K.J., Searson, P.C. (2003). Synthesis and characterization of nitrogen rich calcium sialon ceramics. *Adv. Matter.* 15, 1289–1294.

Phadtare, S., Kumar, A., Vinod, V.P., Dash, C., Palaskar, D.V., Rao, M., Shukla, P.G., Sivaram, S., Sastry, M. (2003). Direct assembly of gold nanoparticle shells on poly urethane microsphere cores and their application as enzyme immobilization templates, *Chem. Mater. 15*, 1944–1949.

Piotrowska, G., Golimowski, J., Urban, P. (2009) Nanoparticles: Their potential toxicity and environmental management. *Waste Management.* 29, 2587-2595.

Podolskiy,V. A., Sarychev, A. K., Shalaev, V. M. (2002). Plasmon modes in metal nanowires and left-handed materials. *J. Nonlinear Opt. Phys. Mater*. *11*, 65-74.

Povinelli, M. L., Johnson, S. G., Joannopoulos, J. D., Pendry, J. B. (2003). Towards photonic crystal matematerials, Creating magnetic emitters in photonic crystals. *Appl. Phys. Lett. 82*, 1069-1071.

Prasad, P. N. (2004). Nanophotonics, John Wiley.

Quang, D. V., Sarawade, P. B., Hilonga, A., Kim, J-K., Chai, Y. G., Kim, S. H., Ryu, J-Y., Kim, H. T. (2011). Preparation of silver nanoparticle containing silica micro beads and investigation of their antibacterial activity. *Applied Surface Science, 257* (15) 6963–6970

Radeshkumar, C., Munstedt, H., (2006) Antimicrobial polymers frompolypropylene/silver composites—Agrelease measured by anode stripping voltammetry. *React. Funct. Polym. 66* (7) 780–788.

Rahman, M. M., Younes, H., Lu, J. Y., Ni, G., Yuan, S., Fang, N. X., Zhang, T.J. Al Ghaferi, A. (2016). Broadband Light Absorption by Silver Nanoparticles Decorated Silica Nanospheres. *RSC Adv.*, 6, 107951-107959.

Raj, R., An, L. N., Shah, S., Riedel, R., Fasel, C., Kleebe, H. J. (2001). Oxidation Kinetics of an Amorphous Silicon Carbonitrided Ceramic. *J. Am. Ceram. Soc. 84* (8) 1803-1810.

Rameshkumar, P., Manivannan, S., Ramaraj, R. (2013). Silver nanoparticles deposited on amine-functionalized silica spheres and their amalgamation-based spectral and colorimetric detection of Hg(II)ions. *J Nanopart Res. 15*, 1639.

Rameshkumar, P., Viswanathan, P., Ramaraj., R. (2014). Silicate sol–gel stabilized silver nanoparticles for sensor applications toward mercuric ions,hydrogen peroxide and nitrobenzene. *Sensors and Actuators B, 202,* 1070–1077.

Rechberger, W., Hohenau, A., Leitner, A., Krenn, J. R., Lamprecht, B., Aussenegg, F.R.(2003). Optical properties of two interacting gold nanoparticles. *Opt. Commun. 220*,137–141.

Ren, C., Sun, J., Li, J., Chen, X., Hu, Z., Xue, D. (2009). Bi-functional silica nanoparticles doped with iron oxide and CdTe prepared by a facile method. *Nanoscale Res.Lett. 4*, 640–645.

Riedel, R. (1996). Advanced Ceramics from Inorganic Polymers. Brook, R.J. *Materials Science and Technology, A Comprehensive Treatment, Vol.17B: Processing of Ceramics. Part II,* 1-50.

Ritchie, R. H. (1957). Plasma Losses by Fast Electrons in Thin Films. *Physical Review,* 106, 874–881.

Robert, C. T., Teresa, M. B., Jeremy, D. B., Andrew, J. F., Bobby, T., Lynn, M. G., Michael, J. H., Jeffrey, L. B. (2009). Ultrasmooth, Large-Area, High-Uniformity, Conducive Transparent Single-Walled-Carbon Nanotube Films for Photovoltaics Produced by Ultrasonic Spraying. *Adv. Mater*. *21* (31) 3210-3216.

Rosenthal, S.J., Mcbride, J., Pennycook, S.J., Feldman, L.C. (2007). *Surf. Sci. Rep*. 62, 111.

Rothrock AR, Donkers RL, Schoenfisch MH. (2005). Synthesis of nitric oxide-releasing gold nanoparticles. *J Am Chem Soc. 127*, 9362–9363.

Sakoda, K. (2001). Optical Properties of Photonic Crystals, Springer Series in Optical Sciences. *Springer-Verlag*, Vol. 80.

Sanada, Atsushi. (2011) Negative permeability and permittivity of meta material and surface wave waveguide. *National University Corporation*, Yamaguchi University, US Patent.

Sanvicens, N., Marco, M. P. (2008). Multifunctional nanoparticles—properties and prospects for their use in human medicine. *Trends Biotechnol. 26* (8) 425–433.

Sau, T.K., Rogach, A.L. (2010). Nonspherical noble metal nanoparticles: Colloid-chemical synthesis and morphology control. *Adv. Mater*. *22*, 1781–1804.

Scaffardi, L.B., Pellegri, N., De, S.O., Tocho, J.O. (2005). Sizing gold nanoparticles by optical extinction spectroscopy. *Nanotechnology,* 16, 158-163.

Scraphin, A. A. (1996). Photoluminescence Properties of Silicon Nanocrystallites. Thesis, *Doctor of Philosophy in Electronic Materials*. Massachusetts Institute of Technology. Department of Materials Science and Engineering.

Sekhar, E.C., Krishna Rao, K.S.V., Sudana Rao, K.M., Alisha, S.B.(2018). A Simple biosynthesis of silver nanoparticles from syzygium cumini stem bark aqueous extract and their spectrochemical and antimicrobial studies. *J. Appl. Pharmaceut. Sci. 8*, 073-079.

Sen, D., Lakhotiya, H., Das,A., Bahadur, J., Mazumder, S., Basak, C. B., (2015). Organic–inorganic composite micro-granules by evaporation induced assembly: role of trapped water in structural evolution. *RSC Adv.* 5 (29) 22884–22891.

Sengupta B, Ritchie CM, Buckman JG, Johnsen KR, Goodwin PM, Petty JT. (2008). Base-directed formation of fluorescent silver clusters. *J Phys Chem C. 112*, 18776–18782.

Shalaev, V.M. (2002). Optical Properties of Nanostructured Random Media, *Topics in Applied Physics*, *vol. 82*. Springer, Berlin.

Shelby, R. A., Smith, D. R., Schultz, S. (2001). Experimental verification of a negative index of refraction. *Science, 292*, 77-79.

Shi, Z-C., Fan, R-H., Zhang, Z-D., Yan, K-L., Zhang, X-H., Sun, K., Liu, X.-F., Wang, C-G. (2013). Experimental realization of simultaneous negative permittivity and permeability in Ag/Y3Fe5O12 random composites. *J. Mater. Chem. C. 1*, 1633-1637.

Shi, X., Ueno, K., Oshikiri, T., Misawa, H. (2013). Improvement of Plasmon-Enhanced Photocurrent Generation by Interference of TiO_2 Thin Film. *J. Phys. Chem. 117*, 24733-24739.

Shibata, S., Aoki, K., Yano, T., Yamanie, M. (1998). Preparation of Silica Microspheres Containing Ag Nanoparticles. *Journal of Sol-Gel Science and Technology, 11* (3) 279–287.

Shvets, G., & Urzhumov, Y. A., (2004). Engineering electromagnetic properties of periodic nanostructures using electrostatic resonance. *Phys. Rev. Lett. 93*, 243902.

Su, K.-H., Wei, Q.-H., Zhang, X. (2003). Interparticle Coupling Effects on Plasmon Resonances of Nanogold Particles, *Nano Letters 3* (8)1087-1090.

Suber, L., Sondi, I., Matijevic E, E. (2005). *J. Colloid Inter Sci.* 288, 489.

Subramanian, V., Wolf, E.E., Kamat, P.V. (2004). Catalysis with TiO_2/Gold Nanocomposites. Effect of Metal Particle Size on the Fermi Level Equilibration, *Journal of the American Chemical Society, 126,* 4943–4950.

Sun , Y. (2010). Silver nanowires – unique templates for functional nanostructures. *Nanoscale* 2, 1626-1642.

Sun, Y., X., Y. (2002). Shape-Controlled Synthesis of Gold and Silver Nanoparticles. *Science Magazine AAAS*, *298* (5601) 2176-2179.

Suzuki, S., Kaneko, S., Fujii, S., Marqu´es-Gonz´ alez, S., Nishino, T., Kiguchi, M. (2016). Effect of the molecule–metal interface on the Surface-Enhanced Raman scattering of 1,4- Benzenedithiol, *J. Phys. Chem. C. 120,* 1038–1042.

Taft, E., Philipp, H. (1961). Optical Constants of Silver. *Phys. Rev.* 121, 1100

Taguchi, A., Fujii, S., Ichimura, T., Verma, P., Inouye, Y., Kawata, S. (2008). Oxygen-assisted shape control in polyol synthesis of silver nanocrystals. *Chemical Physics Letters, 462*, 92-95.

Tan, H., Santbergen, R., Smets, A.H.M., Zeman, M. (2012). Plasmonic light trapping in thin-film silicon solar cells with improved self-assembled silver nanoparticles. *Nano Lett., 12* 4070–4076.

Tang, S., Tang, Y., Zhu, S., Lu, L., Meng, X. (2007). Synthesis and characterization of silica–silver core-shell composite particles with uniform thin silver layers. *J. Solid State Chem. 180*, 2871–2876.

Takenaka, M., Morii, K., Sugiyama, M., Nakano, Y., Takagi, S. (2012). Dark Current reduction of Ge photodetector by GeO_2 surface passivation and gas-phase doping. *Opt. Express. 20,* 8718-8725.

Thimsen, E., Le Formal, F., Grätzel, M., Warren, S. (2011). Influence of Plasmonic Au Nanoparticles on the Photoactivity of Fe_2O_3 Electrodes for Water Splitting. *Nano Lett. 11*,35–43.

Tian, Y., Tatsuma, T.(2005). Mechanisms and Applications of Plasmon-Induced Charge Separation at TiO_2 Films Loaded with Gold Nanoparticles. *J. Am. Chem. Soc. 127* (20)7632–7637.

Trefry, J. C., Monahan, J. L., Weaver, K. M., Meyerhoefer, A. J., Markopolous, M. M., Arnold, Z. S., Wooley, D. P., and Pavel, I. E. (2010). Size selection and concentration of silver nanoparticles by tangential flow ultrafiltration for SERS-based biosensors. *J. Am. Chem. Soc. 132*, 10970–10972.

Tripathy, A., Raichur, Chandrasekaran, A.M.N., Prathna, T.C., Mukherjee, A. (2010). Process variables in biomimetic synthesis of silver nanoparticles by aqueous extract of *Azadirachta indica* (Neem) leaves. *J. Nanopar Res* 12 237.

Uetsuki, K., Verma, P., Yano, T., Saito, Y., Ichimura, T., Kawata, S. (2010). Experimental identification of chemical effects in surface enhanced Raman scattering of 4 aminothiophenol. *J. Phys. Chem. C. 114*, 7515–7520.

Umadevi, A. J. C. M. (2012). Synthesis and characterization of monodispersed silver nanoparticles. Advances in Natural Sciences: *Nanoscience and Nanotechnology*, 3, 035013.

Van Der Vis, M.G.M., Cordfunke, E., Konings, R. (1993). The Thermodynamic Properties Of Tetraethoxysilane (Teos) and an Infrared Study of its Thermal Decomposition. *Journal De Physique IV* Colloque C3, Supplement Au Journal De Physique, 11(3) 75-82.

Van der Horst, C., Silwana, B., Iwuoha, E., Somerset, V. (2015). Synthesis and characterization of Bismuth-Silver nanoparticles for electrochemical sensor applications. *Anal. Lett. 48,* 1311–1332.

Vernon KC, Funston AM, Novo C, Go´mez DE, Mulvaney P, Davis TJ. (2010). Influence of particle–substrate interaction on localized plasmon resonances. *Nano Lett.* 10 (6), 2080–2086.

Vodnik, V.V., Bozanic, D.K., Dzunuzovic, E., Vukovic, J., Nedeljkovic, J.M. (2010). Thermal and optical properties of silver-poly(methylmethacrylate) nanocomposites prepared by in-situ radical polymerization. *Eur. Polym. J*. 46, 137–142.

Wang, H., You, T., Shi, W., Li, J., Guo, L. (2012). $Au/TiO_2/Au$ as a Plasmonic Coupling Photocatalyst. The Journal of Physical Chemistry C, 116 (10)6490–6494.

Wang, P., Huang, B., Dai, Y., Whangbo, M.-H. (2012). Plasmonic photocatalysts : harvesting visible light with noble metal nanoparticles. *Phys. Chem. Chem. Phys. 14*, 9813–9825.

Wang, X., Fan, H., Ren, P., Yu, H., Li, J. (2012). A simple route to disperse silver nanoparticles on the surfaces of silica nanofibers with excellent photo-catalytic properties. *Mater. Res. Bull. 47*, 1734–1739.

Weast, R.C. (1968). Handbook of Chemistry and Physics. *The Chemical Rubber Publishing Co. 48*, F149.

Wilcoxon, J.P., Martin, J.J.E., Parsapour, F. (1998). *J. Chem. Phys.* 108, 9137.

Wu, Z. G., Jia, Y. R., Wang, J., Guo, Y., Gao, J. F. (2016). Core-shell SiO_2/Ag composite spheres: synthesis, characterization and photocatalytic properties. Materials Science-Poland, 34 (4) 806-810.

Xie, Y., Chen, T., Cheng, Y., Wang, H., Qian, H., Yao, W. (2014). SiO_2@Au nanoshells-based SERS method for detection of sunset yellow and chrysoidine. *Spectrochim. Acta, 132*, 355–360.

Xu, G., Tazawa, M., Jin, P., Nakao, S. (2005). Surface plasmon resonance of sputtered Ag films: substrate and mass thickness dependence. *Appl. Phys. A,* 80, 1535–1540.

Xu, J., Han, X., Lin, H., Hu, Y. (2006) Synthesis and optical properties of silver nanoparticles stabilized by gemini surfactant. *Colloids Surf. A*. *179* 179–184.

Yang, H. U., D'Archangel, J., Sundheimer, M. L., Tucker, E., Boreman, G. D., Raschke, M. B. (2015) Optical dielectric function of silver. *Physical Review B*, 91, 235137.

Yang, H., Wang, Y., Chen, X., Zhao, X., Gu, L., Huang, H., Yan, J., Xu, C., Li, G., Wu, J., Edwards, A. J., Dittrich, B., Tang, Z., Wang, D., Lehtovaara, L., Ha¨kkinen, H., Zheng, N. (2015). Plasmonic twinned silver nanoparticles with molecular precision. *Nature Comm*. *7*,12809.

Yao, T., Lin, Q., Zhang, K., Zhao, D., Lv, H., Zhang, J., Yang, B. (2007). Preparation of SiO_2 @ polystyrene@polypyrrole sandwich composite and hollow polypyrrole capsule with movable SiO_2 spheres inside. *J. Colloid Interface Sci. 2.* 315- 434.

Yoon, W.-J., Jung, K.-Y., Liu, J., Duraisamy, T., Revur, R., Teixeira, F.L., Sengupta, S., Berger, P.R. (2010). Plasmon-enhanced optical absorption and photocurrent in organic bulk heterojunction photovoltaic devices using self-assembled layer of silver nanoparticles. *Sol. Energy Mater. Sol. Cells. 94* (2) 128–132.

Yu, H., Peng, Y., Yang, Y., Li, Z-Y. (2019) Plasmon-enhanced light-matter interactions and applications. *npj Comput. Mater* 5, 45.

Yu, Y., Cardona, M. (1995). Fundamentals of Semiconductors, pp.348, *Springer*, Berlin.

Zhang, F., Li, Y., Gu, Y.-e., Wang, Z., Wang, C. (2011). One-pot solvothermal synthesis of a Cu_2O/Graphene nanocomposite and its application in an electrochemical sensor for dopamine. Microchim. Acta. 173, 103–109.

Zhang, J.Z. (2008). Optical properties and spectroscopy of nanomaterials, *World Scientific Publishing,* London.

Zhang, Q., Xie, J., Yu. Y., Lee, J.Y. (2010). Monodispersity control in the synthesis of monometallic and bimetallic quasi-spherical gold and silver nanoparticles. *Nanoscale. 2*, 1962–1975.

Zhang, W., Qiao, X., Chen, J. (2007). Synthesis of nanosilver colloidal particles in water/oil microemulsion. *J. Colloids Surf. A: Physic Eng Asp. 299*, 22.

Zheng,Y., Chen, C., Zhan, Y., Lin, X., Zheng, Q., Wei, K., Zhu, J. (2008). Photocatalytic activity of Ag/ZnO heterostructure nanocatalyst: correlation between structure and property. *J. Phys. Chem. C 112* , 10773–10777,

Zhou, Q., Kaappa, S., Malola, S., Lu, H., Guan, D., Li, Y., Wang, H., Xie, Z., Ma, Z., Häkkinen, H., Zheng, N., Yang, X., Zheng, L. (2018). Real-space imaging with pattern recognition of a ligand-protected Ag374 nanocluster at sub-molecular resolution, *Nature Communication*. 9, 2948.

Ziolkowski, R. W., Heyman, E. (2001). Wave propagation in media having negative permittivity and permeability. *Phys. Rev. E. 64*, 056625.

Zrenner, A., *Nature*. 418 (2002), 612

Internet Reference

Goldman L, Coussesns C. (2005). Implications of Nanotechnology for Environmental health Research. Roundtable on Environmenatal health Sciences, Research Medicine. Retrived from : http://www.nap.edu/catalog/11248.html [cited 2020 July].

Scheerschmidt, K. (2007). Optical properties of Ag in glasses. *Max-Planck Institut.* Retrieved from https://www-old.mpi-halle.mpg.de/department2/research-areas/nanowires-nanoobjects/md-simulations-of-silica-glasses-and-small-particles/abstract/optical-properties-of-ag-in-glasses/

Mons, S. (2007). Schematic silica gel surface, Retrieved from:https://www.differencebetween.com/difference-between-colloidal-silica-and-reactive-silica

Cheng Zeng, Xiao. (2015). Researchers model new atomic structures of gold nanoparticle. Retrieved from: https://www.nanowerk.com/nanotechnology-news/newsid=39884.php. [cited 2020 May]

Oldenburg, S.J.(2015). Silver Nanoparticles : Properties and Applications. Retrieved from: https://www.sigmaaldrich.com/technical-documents/articles/materials-science/nanomaterials/silver-nanoparticles.html. [cited 2015 August]